creative commons
COMMONS DEED

저작자표시-비영리-변경금지 2.0 대한민국

이용자는 아래의 조건을 따르는 경우에 한하여 자유롭게

- 이 저작물을 복제, 배포, 전송, 전시, 공연 및 방송할 수 있습니다.

다음과 같은 조건을 따라야 합니다:

저작자표시. 귀하는 원저작자를 표시하여야 합니다.

비영리. 귀하는 이 저작물을 영리 목적으로 이용할 수 없습니다.

변경금지. 귀하는 이 저작물을 개작, 변형 또는 가공할 수 없습니다.

- 귀하는, 이 저작물의 재이용이나 배포의 경우, 이 저작물에 적용된 이용허락조건을 명확하게 나타내어야 합니다.
- 저작권자로부터 별도의 허가를 받으면 이러한 조건들은 적용되지 않습니다.

저작권법에 따른 이용자의 권리는 위의 내용에 의하여 영향을 받지 않습니다.

이것은 이용허락규약(Legal Code)을 이해하기 쉽게 요약한 것입니다.

Disclaimer

dCollection

ULSAN NATIONAL INSTITUTE OF
SCIENCE AND TECHNOLOGY

High-Performance Field-Effect Transistor-Type Sensors Based on Nanoscopically Engineered Organic Semiconductors

Moonjeong Jang

Department of Energy Engineering
(Energy and Chemical Engineering)

Graduate School of UNIST

ULSAN NATIONAL INSTITUTE OF SCIENCE AND TECHNOLOGY

High-Performance Field-Effect Transistor-Type Sensors Based on Nanoscopically Engineered Organic Semiconductors

A thesis submitted to the Graduate School of UNIST in partial fulfillment of the requirements for the degree of Doctor of Philosophy in the Energy Engineering (Energy and Chemical Engineering)

Moonjeong Jang

1. 11. 2017

Approved by

Advisor

Changduk Yang

Approved by

Advisor

Joon Hak Oh

ULSAN NATIONAL INSTITUTE OF SCIENCE AND TECHNOLOGY

High-Performance Field-Effect Transistor-Type Sensors Based on Nanoscopically Engineered Organic Semiconductors

Moonjeong Jang

This certifies that the thesis of Moonjeong Jang is approved.

1. 11. 2017

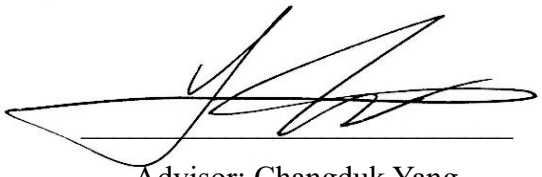

Advisor: Changduk Yang

Joon Hak Oh: Thesis Committee Member #1

Hyunhyub Ko: Thesis Committee Member #2

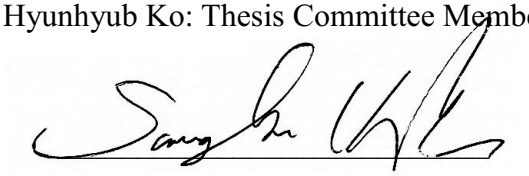

Sang Kyu Kwak: Thesis Committee Member #3

Byeong-Su Kim: Thesis Committee Member #4

ULSAN NATIONAL INSTITUTE OF SCIENCE AND TECHNOLOGY

Abstract

Sensors based on organic field-effect transistor (OFET) platforms show great promise for use in chemical and biological sensors due to their prominent advantages, including high sensitivity, light-weight, low-cost, simple platforms, and flexible applications. Functional properties of active organic semiconductor layers can be tailored by material design or/and surface functionalization to enhance selectivity. To date, a large number of sensors for chemical and biogenic substances have used high-cost immobilization methods and high-end technologies. OFET-based sensors are particularly attractive for applications in simple, cost-effective, high-performance electronics. Furthermore, the sensitivity, selectivity, response time, stability, reproducibility, and limit of detection of sensors can be optimized by choosing or engineering more suitable fabrication techniques and materials for the active layers. Such on-demand, structure-engineered, and surface-engineered organic semiconducting layers are highly desirable for the practical uses of OFETs. In my thesis, commendable molecular engineering, process engineering and interface engineering are highlighted to demonstrate the feasibility of high-performance nanoscopically engineered organic-transistor-based sensors.

Here, I begin with an introduction to OFET and organic sensors, with an emphasis on the organic semiconductor engineering strategies in chapter 1. In detail, in chapter 1, typical properties of organic semiconductors, a discussion of OFET operation, and a working principles of this OFET-type sensors are introduced. Chapter 2 presents molecular engineering strategies to enable the fabrication of *n*-channel-dominant ambipolar OFETs. The electrical charge transport through fluorine-substituted semiconducting materials is investigated. These investigations are easily applied to demonstrate complementary inverters with a reasonable performance.

In chapter 3, I focus on the device design and fabrication of high mobility OFETs made by using organic–organic heterointerface. Pentacene is used as an active layer above, and *m*-bis(triphenylsilyl)benzene is used as the bottom layer. Sequential evaporation process without breaking vacuum of these materials results in high-quality organic semiconductor thin films with far fewer grain boundaries. In addition, the pentacene film exhibits myriad nanometre-sized pores in the organic layers. This surprising structure, the pore-rich structure improves the sensitivity of organic-transistor-based chemical sensors. This approach demonstrates a conceptually novel methodology for the fabrication of “structurally engineered” organic semiconducting thin films and our work has a significant impact in the fields of materials science as well as organic electronics.

Furthermore, organic semiconductor engineering strategies to improve sensitivity and selectivity for biogenic substances by direct semiconductor surface functionalization and to enhance sensitivity and selectivity towards psychostimulants by modification with specific selective sensing layer are given in chapter 4 and 5, respectively.

ULSAN NATIONAL INSTITUTE OF SCIENCE AND TECHNOLOGY

In chapter 4, highly sensitive organic-transistor-based sensors that can selectively detect a neurotransmitter acetylcholine without enzyme immobilization are fabricated using organic thin films functionalized with a synthetic receptor, a cucurbit[6]uril (CB[6]) derivative. The liquid-phase sensing experiments are successfully performed by using organic semiconductor layer with high operational stability in water. The findings provide a low-cost, simple, and feasible method for the fabrication of high-performance water-stable sensors for biogenic substances. In addition, the results obtained herein describe the first demonstration of acetylcholine sensing without any enzymatic reactions using the synthetic receptor-functionalized OFET-platform. In chapter 5, the direct detection of amphetamine-type-stimulants (ATS) is suggested for the illicit and designer drugs sensing OFET platforms. Their novel sensing system and sensing mechanism are studied using other CB homologues, a cucurbit[7]uril (CB[7]) derivative decorated OFET-based sensors. By synergistic combination of a highly selective synthetic host molecule and a highly sensitive OFET device, the first ATS sensors with specific synthetic receptor-engineered OFET-platform are demonstrated flexible polymer substrates. These sensors in physiological buffer system and even in urine samples show highly sensitive sensing behaviors.

ULSAN NATIONAL INSTITUTE OF
SCIENCE AND TECHNOLOGY

ULSAN NATIONAL INSTITUTE OF SCIENCE AND TECHNOLOGY

Contents

Contents 3
List of Figures and Schemes 5
List of Tables 11
Chapter 1. Introduction to Organic Field-Effect Transistors 12
1.1. Organic Field-Effect Transistor (OFET) Overview 12
1.2. Fabrication of High-Performance Organic Semiconductors 14
1.3. Sensor Applications of Nanoscopically Engineered Organic Semiconductors 15
1.4. References 17
Chapter 2. Investigation of Charge-Transport Properties in Fluorinated DPP-Benzothiadiazole (BT) Polymer Semiconductors 21
2.1. Introduction 22
2.2. Experimental Section 23
2.3. Results and Discussion 25
2.4. Conclusion 30
2.5. References 31
Chapter 3. Fabrication of Nanostructured Organic Semiconductor Thin Films and Their Chemical Sensor Applications 42
3.1. Introduction 43
3.2. Experimental Section 43
3.3. Results and Discussion 45
3.4. Conclusion 49
3.5. References 51
Chapter 4. Highly Sensitive and Selective Biosensors Based on Functionalized Organic Semiconductors 65
4.1. Introduction 66
4.2. Experimental Section 67
4.3. Results and Discussion 69
4.4. Conclusion 73
4.5. References 74
Chapter 5. Highly Sensitive Amphetamine-Type Stimulants Sensors Based on Surface-Engineered Organic Semiconductors 84
5.1. Introduction 85
5.2. Experimental Section 86

ULSAN NATIONAL INSTITUTE OF SCIENCE AND TECHNOLOGY

5.3. Results and Discussion 87
5.4. Conclusion 92
5.5. References 93
Chapter 6. Summary and Perspectives 102
Acknowledgements 105

ULSAN NATIONAL INSTITUTE OF SCIENCE AND TECHNOLOGY

List of Figures and Schemes

Figure 1.1. Schematic diagrams of two bottom-gate OFET configurations: a) top-contact and b) bottom contact. OSC, organic semiconductor; S, source; D, drain.

Figure 1.2. Simplified illustration of the operation principle of an OFET with *p*-channel semiconductor. OSC, organic semiconductor; S, source; D, drain.

Figure 1.3. a) Schematic diagram of organic-transistor-based sensors. b) Typical device response upon exposure to analyte. The semiconductor used is *p*-channel material. Color code: OSC, green.

Scheme 2.1. Synthetic route to PDPP-FBT and PDPP-2FBT. [a]Suzuki polycondensation conditions (i): $Pd_2(dba)_3$, P(*o*-tolyl)$_3$, K_3PO_4, toluene/H_2O, 95 °C; Stille polycondensation conditions (ii): $Pd_2(dba)_3$, P(*o*-tolyl)$_3$, toluene, 120 °C, microwave.

Figure 2.1. UV–vis–NIR absorption spectra of PDPP-FBT and PDPP-2FBT in dilute chloroform (a) solution and (b) thin film on glass plate. (c) Cyclic voltammograms of PDPP-FBT and PDPP-2FBT. (d) UPS spectra of PDPP-FBT and PDPP-2FBT.

Figure 2.2. UV-vis-NIR absorption spectra of PDPP-BT in dilute chloroform (a) solution and (b) thin film on glass plate. Cyclic voltammograms of (c) PDPP-BT and UPS spectrum of (d) PDPP-BT.

Figure 2.3. TGA traces of (a) PDPP-FBT and (b) PDPP-2FBT, the heating rate is 10 $^oC\ min^{-1}$. DSC curve of (c) PDPP-FBT and (d) PDPP-FBT at a heating rate of 10 $^oC\ min^{-1}$.

Figure 2.4. Calculated side view of model trimers for (a) DPP-FBT and (b) DPP-2FBT; DFT-optimized geometries and charge-density isosurfaces for (c) DPP-FBT and (d) DPP-2FBT HOMO and LUMO levels.

Figure 2.5. Calculated side view of model trimer (a) DPP-BT. DFT-optimized geometries and charge-density isosurfaces for (b) DPP-BT HOMO and LUMO energy levels.

Figure 2.6. Net dipole moments of DPP-BT, DPP-FBT, and DPP-2FBT units in the ground and excited state, respectively (blue line: dipole moment vector).

Figure 2.7. AFM height images (5 μm × 5 μm) of drop-cast (a, b) PDPP-FBT and (c, d) PDPP-2FBT films (a, c) before and (b, d) after the thermal annealing at 250 °C, on OTS-modified SiO_2/Si substrates. RMS roughness: (a) = 7.67 nm, (b) = 6.90 nm, (c) = 11.80 nm, (d) = 8.57 nm.

Figure 2.8. 2D-GIXD images of drop-cast films of fluorinated DPP-BT copolymers annealed at 250 °C: (a) PDPP-FBT and (b) PDPP-2FBT. The corresponding GIXD diffractogram profiles: (c) in-plane and (d) out-of-plane GIXD patterns.

Figure 2.9. 2D-GIXD images of as-cast films of fluorinated DPP-BT copolymers: (a) PDPP-FBT and (b) PDPP-2FBT. The corresponding GIXD diffractogram profiles: (c) in-plane and (d) out-of-plane GIXD patterns.

ULSAN NATIONAL INSTITUTE OF SCIENCE AND TECHNOLOGY

Figure 2.10. Current-voltage (*IV*) characteristics of OFETs based on ambipolar (a–d) PDPP-FBT and (e–h) PDPP-2FBT films of annealed at 250 °C. Transfer characteristics for polymer films in (a, e) *p*-channel operation (V_{DS} = -100 V) and (c, g) *n*-channel operation (V_{DS} = +100 V) mode. (b, d, f, and h) Output characteristics for PDPP-FBT and PDPP-2FBT films.

Figure 2.11. Current-voltage (*IV*) characteristics of OFETs based on as-cast film of ambipolar {(a)-(d)} PDPP-FBT and {(e)-(h)} PDPP-2FBT. Transfer characteristics for polymer films in (a), (e) *p*-channel operation (V_{DS} = -100 V) and (c), (g) *n*-channel operation (V_{DS} = +100 V) mode. {(b), (d), (f) and (h)} Output characteristics for PDPP-FBT and PDPP-2FBT films.

Figure 2.12. Inverter characteristic based on (a) ambipolar PDPP-FBT and (b) PDPP-2FBT OFETs (V_{DD} = 100V).

Figure 3.1. Device structure and Morphology of organic layers: a) Device schematic and the molecular structure of TSB3. b) AFM height images of (*left*) pentacene / TSB3 and (*right*) pentacene on OTS-treated SiO_2. A large number of pores are present in the pentacene-TSB3 film. The scale bars are 1 μm. c) Cross-sectional HRTEM image of pentacene (45 nm) / TSB3 (15 nm) on OTS-treated SiO_2. The depth of the pore, also clearly observed in the AFM image of Figure 3.1b, is the same as the thickness of the pentacene/TSB3 layers. The scale bars are 50 nm.

Figure 3.2. Analysis on TSB3 molecules: a) Ultraviolet–visible spectrum of TSB3 thin film. The band gap of a TSB3 thin film (15 nm) was measured to be 3.6 eV. b) (Upper) Optimized geometry of a TSB3 molecule in vacuum and (lower) its charge-density isosurfaces calculated by density functional theory (DFT) calculations. c) Cyclic voltammetry results of pentacene and TSB3 molecules. [HOMO_Pentacene: −5.04 eV and HOMO_TSB3: −6.58 eV] d) Differential scanning calorimetry data of TSB3 molecules. The glass transition temperature (T_g) and melting temperature (T_m) of TSB3 were estimated to be 33 °C and 238 °C, respectively.

Figure 3.3. Cross-sectional SEM (first row) and HRTEM (second and third rows) images of pentacene (45 nm) / TSB3 (15 nm) and pentacene (45 nm) on OTS-treated SiO_2. The pentacene/TSB3 film exhibits much smoother surface than the pentacene film without TSB3, which corroborates more 2D growth of pentacene on TSB3.

Figure 3.4. Electrical measurement data for the pentacene OFETs and morphological analysis: a) Current-voltage curves for pentacene OFETs with and without TSB3, measured inside a nitrogen-filled glovebox. Pentacene/TSB3 OFETs: [μ_{FET} = 5.5 (±0.7) $cm^2 V^{-1} s^{-1}$, V_{TH} = -37.5 (±0.8) V, I_{ON}/I_{OFF} = 3.7 (±0.5) $\times 10^6$]; Pentacene OFETs: [μ_{FET} = 1.5 (±0.2) $cm^2 V^{-1} s^{-1}$, V_{TH} = -33.5 (±1.1) V, I_{ON}/I_{OFF} = 6.9 (±3.2) $\times 10^6$] b) AFM height image and cross-sectional profile of a 15-nm-thick TSB3 film on OTS-treated SiO_2. When the TSB3 thin film is deposited without a rigid layer on top, the substrate surface is severely dewetted, and the TSB3 film becomes agglomerated. The scale bar is 500 nm. c–f) SEM images of pentacene (film thicknesses c) 5, d) 10, e) 20, f) 45 nm) / TSB3 (15 nm) on OTS-treated SiO_2. Similar to Figure 3.4b, clusters are also found in pentacene (5 and 10 nm) / TSB3 layers. However, such clusters

ULSAN NATIONAL INSTITUTE OF SCIENCE AND TECHNOLOGY

are not observed when a thick layer of pentacene (20 and 45 nm) was deposited onto the TSB3 film. The scale bars are 500 nm. g) 2D GIXD image of pentacene (5 nm) / TSB3 (15 nm) on OTS-treated SiO_2. Predominantly the thin-film-phase peaks are present. h) Magnified AFM images of pentacene (45 nm) / TSB3 (15 nm) and pentacene (45 nm) on OTS-treated SiO_2, and a schematic diagram of the charge transport inside pentacene layers with and without TSB3. The scale bars are 200 nm.

Figure 3.5. Current-voltage curves of pentacene OFETs measured inside a nitrogen-filled glovebox: a) Drain current vs. gate-source voltage curves with and without TSB3 in logarithmic scale. b) Drain current vs. drain-source voltage curves of pentacene OFET with TSB3.

Figure 3.6. OFET-based chemical sensor utilizing the vertical macropores: a) Schematic diagram of an OFET-based sensor with macroporous layers made of pentacene and TSB3. b) Variation of the output current in the sensor as a function of time. The bias stress effect was compensated by dividing the measured current data by the current without the flow of analyte, and the data was normalized to the initial current at t=0. The blue regions indicate the flow of methanol gas (analyte). As clearly shown in the plot, the sensor with TSB3, having vertical macropores, exhibits higher sensitivity than the sensor without TSB3. Both V_{GS} and V_{DS} were fixed at -100 V.

Figure 3.7. GIXD images of pentacene thin film with and without TSB3: a) Pentacene (45 nm) / TSB3 (15 nm) on OTS-treated SiO_2. The pentacene layer with TSB3 shows dominant thin-film-phase peaks. b) Pentacene (45 nm) on OTS-treated SiO_2. The pentacene layer without TSB3 shows dominant bulk-phase peaks.

Figure 3.8. Two-dimensional grazing incidence X-ray diffraction pattern of 15-nm-thick TSB3 on OTS-treated SiO_2. The circular pattern indicates that the TSB3 film is not preferentially oriented on the substrate.

Figure 3.9. Proposed mechanism for the growth of pentacene on TSB3. In this growth model, the pores in pentacene are expected to form on the exposed OTS surface.

Figure 3.10. Snapshots of molecular dynamics systems of TSB3 on OTS and their van der Waals (vdw) interaction energies at 60 °C. Each system contains 144 OTS molecules in the bottom layer with a, 25, b, 50 and c, 75 TSB3 molecules on top. Vacuum is introduced above TSB3 and below OTS. The term "BE" stands for binding energy.

Figure 3.11. Snapshots of molecular dynamics systems of (a, b, c) pentacene on TSB3 and (d, e, f) pentacene on OTS, and their van der Waals (vdw) interaction energies at 60 °C. The TSB3 and OTS layers contain 66 and 81 molecules, respectively. One layer of pentacene is composed of 60 molecules. (a, d) Monolayers, (b, e) bilayers and (c, f) trilayers of pentacene were simulated. Vacuum is introduced above pentacene and below the bottom layer (TSB3 or OTS). The term "BE" stands for binding energy.

Figure 3.12. Molecular dynamics simulation of pentacene diffusion: a) Top-view and b) cross-sectional snapshots of the molecular dynamics system of pentacene on the interfacial region between TSB3 and OTS. The upper images show the beginning of the simulation. After 50 ps, the pentacene molecules

ULSAN NATIONAL INSTITUTE OF SCIENCE AND TECHNOLOGY

gradually diffuse towards TSB3, which confirms that pentacene has higher attractive interaction with TSB3 than OTS. Yellow dashed lines indicate the boundary between OTS and TSB3.

Figure 3.13. Snapshots of molecular dynamics systems of monolayer pentacene on a) TSB3, b) polystyrene (PS) and c) poly(methyl methacrylate) (PMMA), and their van der Waals interaction energies at 60 °C. a) The TSB3 and pentacene layers contain 66 and 60 molecules, respectively. b) and c) Each system contains 84 pentacene molecules on 50 decamers of PS or PMMA. Vacuum is introduced above pentacene and below the bottom layer (TSB3, PS or PMMA). The interaction energy in the y-axis represents binding energy.

Figure 4.1. a) Schematic illustration of the top-contact OFET-based sensors with a synthetic receptor, AOCB[6], and b) the molecular structure of AOCB[6]. In the device structure, only monolayer of AOCB[6] is shown for clarity.

Figure 4.2. Current-voltage (I–V) characteristics of DDFTTF OFETs with and without AOCB[6]. a) Transfer characteristics for DDFTTF OFETs in *p*-channel operation mode and a source-drain electrode geometry of W/L = 180. b) Output characteristics for DDFTTF OFETs with AOCB[6].

Figure 4.3. AFM images of OTS-modified SiO_2/Si substrates with a scan size of 2 μm × 2 μm; a), c) Height and b), d) phase images of DDFTTF film before and after thermal annealing at 150 °C for 30 min in nitrogen conditions. e) Height, f) phase images of AOCB[6]/DDFTTF film after annealing at 150 °C for 30 min under nitrogen conditions.

Figure 4.4. a) Real-time responses of DDFTTF OFET-based sensors with AOCB[6] toward various concentrations (1 pM – 100 mM) of ACh^+ and Ch^+, and pure DI water under typical operation conditions (V_{DS} = –2 V and V_{GS} = –60 V). b) Statistical comparisons of the sensing results for ACh^+ and Ch^+ (S indicates $I_D/I_{D\text{-}BASE}$).

Figure 4.5. Comparison of responses of the DDFTTF OFET-based sensors with and without AOCB[6] toward 1 pM of ACh^+ at V_{DS} = –2 V and V_{GS} = –60 V.

Figure 4.6. a) Real-time responses of DDFTTF OFET-based sensors with AOCB[6] toward various Na^+ concentrations (1 μM – 100 mM) at V_{DS} = –2 V and V_{GS} = –60 V. b) Statistical results for sensing Na^+ (S indicates $I_D/I_{D\text{-}BASE}$).

Figure 4.7. Real-time responses of the sensors with AOCB[6] toward pristine PBS and various concentrations (1 pM – 1 μM) of ACh^+ in a PBS solution at V_{DS} = –2 V and V_{GS} = –60 V. Acetylcholine chloride solutions were prepared in a PBS solution (pH 7.4, 0.01 M) containing sodium chloride (137 mM) and potassium chloride (2.7 mM).

Figure 4.8. DFT optimized structures of the complexations of CB[6] and analytes: a) CB[6]-ACh^+ and b) CB[6]-Ch^+. Hydrogens of CB[6] are omitted for clarity. Color code: C, gray; O, red; N, blue; H, white.

Figure 4.9. DFT optimized structures of the complexation of CB[6]-Na^+. Hydrogens of CB[6] are

ULSAN NATIONAL INSTITUTE OF SCIENCE AND TECHNOLOGY

omitted for clarity. Color code: C, gray; O, red; N, blue; H, white; Na, purple.

Figure 4.10. Charge changes on CB[6] after complexation with three guest molecules (ACh^+, Ch^+, and Na^+). For structures obtained from molecular dynamics simulations, charges of CB[6] are obtained from the natural population analysis at the M06-2X/6-31G(d) level.

Figure 4.11. Signal changes of the sensors with AOCB[6] for the mixing systems of analytes containing both ACh^+ and Ch^+ at V_{DS} = –2 V and V_{GS} = –60 V. The red line indicates the rate of the signal change.

Figure 4.12. a) Schematic illustration of flexible DDFTTF OFET-based sensors with AOCB[6]. b) Photograph of a flexible sensor prepared with an Al_2O_3 gate dielectric on an ITO-coated PEN substrate. c) Real-time responses of the sensors with AOCB[6] toward 1 pM ACh^+ under a low-voltage operation condition.

Figure 4.13. a) Transfer and b) output characteristics for flexible DDFTTF OFET-based sensors with AOCB[6] in *p*-channel operation mode.

Figure 5.1. Chemical structures of the ATS tested and receptor CB[7].

Figure 5.2. a) ^{1}H-NMR spectra of complexation of **1** and CB[7] in D_2O. (b) X-ray structure of **1**@CB[7].

Figure 5.3. a) ^{1}H-NMR spectra of complexation of **2** and CB[7] in D_2O. (b) X-ray structure of **2**@CB[7].

Figure 5.4. a) Schematic illustration of the top-contact OFET-based sensors with AOCB[7]. b) Transfer characteristics of DDFTTF OFETs with and without AOCB[7] in *p*-channel operation mode. c) Transfer characteristics for DDFTTF OFETs with AOCB[7] under low-voltage operation.

Figure 5.5. AFM images of the active layers of DDFTTF OFET-based sensors; a) Height and b) phase images of DDFTTF film after thermal annealing at 150 °C for 30 min in nitrogen conditions. c,e) Height and d,f) phase images of the surface of the sensors with AOCB[7] film before and after sensing tests for amphetamine, respectively.

Figure 5.6. a) Comparison of sensing responses of the DDFTTF OFET-based sensors with AOCB[7] and with AOCB[6] toward 100 mM of PEA at V_{DS} = -2 V and V_{GS} = -60 V. b) Sensing results of the sensors with AOCB[7] toward various PEA concentrations (from 1 nM to 100 mM) at V_{DS} = -2 V and V_{GS} = -60 V.

Figure 5.7. a) Real-time responses of DDFTTF OFET-based sensors with AOCB[7] toward various concentrations (from 1 pM to 1 μM) of amphetamine under typical operation conditions (V_{DS} = -2 V and V_{GS} = -60 V). b) Plots showing the sensitivity for amphetamine. The error bar represents the standard deviation.

Figure 5.8. a) Comparison of sensing responses of the DDFTTF OFET-based sensors with and without AOCB[7] toward 1 pM of amphetamine at V_{DS} = -2 V and V_{GS} = -60 V.

Figure 5.9. a) Real-time responses of DDFTTF OFET-based sensors with AOCB[7] toward various concentrations (from 1 pM to 1 μM) of methamphetamine under typical operation conditions (V_{DS} = -2 V and V_{GS} = -60 V). b) Plots showing the sensitivity for methamphetamine. The error bar represents the standard deviation.

ULSAN NATIONAL INSTITUTE OF SCIENCE AND TECHNOLOGY

Figure 5.10. a) Comparison of the electrical characteristics of the DDFTTF OFETs with AOCB[7] before and after sensing tests for amphetamine, and re-thermal annealing. b) AFM height image of AOCB[7]/DDFTTF film on OTS-treated SiO2 after re-annealing at 150 °C for 30 min in nitrogen conditions.

Figure 5.11. a) Real-time responses of the sensors with AOCB[7] toward pristine PBS and various concentrations (from 1 pM to 1 μM) of amphetamine in a PBS solution at V_{DS} = -2 V and V_{GS} = -60 V. Amphetamine solutions were prepared in a PBS solution (pH 7.4, 0.01 M) containing sodium chloride (137 mM) and potassium chloride (2.7 mM).

Figure 5.12. a) Sensing responses of the DDFTTF OFET-based sensors with AOCB[7] toward pristine artificial urine at V_{DS} = -2 V and V_{GS} = -60 V. b) Sensing results of the sensors with AOCB[7] toward various amphetamine concentrations (from 0.2 pM to 0.2 μM) in a urine solution at V_{DS} = -2 V and V_{GS} = -60 V.

Figure 5.13. a) Schematic illustration of a flexible DDFTTF OFET-based sensor with AOCB[7] sensor prepared with an Al_2O_3 gate dielectric on an ITO-coated PEN substrate. b) Real-time responses of the sensors with AOCB[7] toward 1 pM amphetamine under a low-voltage operation condition. The inset shows a photograph of the flexible sensor with AOCB[7].

Figure 5.14. a) Transfer and b) output characteristics for flexible DDFTTF OFET-based sensors with AOCB[7] in *p*-channel operation mode.

ULSAN NATIONAL INSTITUTE OF
SCIENCE AND TECHNOLOGY

List of Tables

Table 2.1. Optical and electrochemical properties of PDPP-FBT and PDPP-2FBT.

Table 2.2. Summary of the ground state and excited state dipole moment for DPP-BT, DPP-FBT, and DPP-2FBT monomer (TD-SCF, RB3LYP/6-311G (d) level).

Table 2.3. Crystallographic parameters calculated from GIXD profiles.

Table 2.4. Summary of OFETs performance data based on PDPP-FBT and PDPP-2FBT films.

Table 2.5. Summary of OFETs performance data based on PDPP-BT films.

Table 4.1. Summary of OFET performance obtained from DDFTTF thin films with and without AOCB[6] layers.

ULSAN NATIONAL INSTITUTE OF SCIENCE AND TECHNOLOGY

Chapter 1

Introduction to Organic Field-Effect Transistors

1.1. Organic Field-Effect Transistor (OFET) Overview

Inorganic semiconductor has been intensively studied and widely applied, however, it requires extremely high purity and very precisely controlling the process under highly demanding conditions. To overcome those challenges, organic semiconductors potentially offer possible solutions. Organic semiconductors including conjugated polymers and small-molecule-based materials have attracted great interest, because they have many promising advantages including their easy-processing, large-area, lightweight, good compatibility with a wide variety of substrates such as flexible plastics, and low cost. Due to their processability advantages and unique electrical, chemical, and optical properties, they have long been considered an impressive class of materials for use in diverse electronic devices such as organic field-effect transistors (OFETs),[1-5] diodes,[6] sensors,[7-9] solar cells,[10, 11] and memory devices.[12]

Among them, transistor based on organic semiconductors is a basic and fundamental building block, and OFETs are referred to as electronic switching elements in all modern electronic devices. The typical OFETs are composed of three main components, an active semiconductor layer, a dielectric (or insulator), and three-terminals (i.e., source, drain, and gate electrodes). Depending on the positon of the source and drain contacts onto the semiconductor layer, a top-contact and a bottom-contact OFET, two types of device architectures are possible (**Figure 1.1**). The former involves source and drain electrodes onto a prefabricated semiconductor layer, whereas the latter is constructed by depositing the organic semiconductor over the gate dielectric and contacts. The top-contact structure can have an electrical performance advantage in terms of larger effective contact area and smaller contact resistance, although the bottom-contact devices are preferable to printed electronics with direct high resolution patterning of the electrodes.[13, 14] However, the top-contact configuration is often difficult to realize with OFETs. Attachment of the electrodes is usually carried out thermally with metals and can destroy organic thin-films; moreover, metal atoms can diffuse into the organic layer.

The schematic and working principle of OFETs are described in **Figure 1.2**. Their performance critically depends on the efficiency with which charge carriers (electrons and/or holes) move within a very narrow conducting channel. OFETs operate as an electronic switch, in which the current flow between the source and drain electrodes is modulated by the gate electrode. A sufficiently high electric field provides the formation of the conducting channel at the interface between semiconductor and gate dielectric as a consequence. In this case, positive charge carriers (i.e., holes) are induced and localized in the semiconductor by applying negative voltage on the gate (with *p*-channel semiconductors). If at

ULSAN NATIONAL INSTITUTE OF SCIENCE AND TECHNOLOGY

the same time a voltage is applied at the drain electrode, holes can be injected from the source into the channel, and holes will be collected by the drain electrode. This conducting state is called the "on" state. However, instead of negative if the gate voltage is set, no holes are created within the conducting channel, which defines the "off" state. In principle, the source-drain current flows (I_D) in the very few semiconductor monolayers in the by potential difference between source and drain electrodes (V_{DS}). A negative/positive gate voltage (V_{GS}) induces positive/negative charge carriers (holes or electrons), OFETs are available in two channel type (P or N). In OFETs, the three key device parameters of interest include field-effect mobility (μ_{FET}, measured in $cm^2\ V^{-1}\ s^{-1}$), on/off current ratio (I_{ON}/I_{OFF}), and threshold voltage (V_{TH}), which were extracted from the transfer curves. V_{TH} is defined as the minimum gate voltage that required to make the transistor ON. The characteristic curve can be differentiated into two regions: at low drain voltage, the source–drain current increases almost linearly (linear region), later to convert into a saturation region. In saturation operation mechanism, the difference between the gate and the drain voltage drops to zero and pinch-off of the channel occurs, allowing that the I_D becomes independent of the drain bias. As the drain voltage increases more, there is behavior with a clear saturation of the I_D beyond the pinch-off point.

The μ_{FET} and V_{TH} were estimated in the linear regime (for $V_{DS} << V_{GS} - V_{TH}$) with the following equation:

$$I_D = \frac{W}{L}\mu_{FET}C_g\left(V_{GS} - V_{TH} - \frac{V_{DS}}{2}\right)V_{DS}, \quad (1)$$

and in the saturated regime (for V_{DS} > or = $V_{GS} - V_{TH}$):

$$I_D = \frac{W}{2L}\mu_{FET}C_g\left(V_{GS} - V_{TH}\right)^2, \quad (2)$$

Here, I_D is the drain current, W and L are the semiconductor channel width and length, respectively, C_g is the capacitance of the gate dielectric and V_{GS} is the gate-source voltage. By calculating these parameters, the key issues for high-performance OFETs are the development of new organic semiconducting films with optimal electronic properties (high charge-carrier mobility, high on/off ratio, and low threshold voltage).

ULSAN NATIONAL INSTITUTE OF SCIENCE AND TECHNOLOGY

1.2. Fabrication of High-Performance Organic Semiconductors

The semiconductor governs the charge transport in the OFET. A high quality and high performance organic semiconductor is a pre-requisite for a high performance transistor. As mentioned previously, small molecules or oligomers as well as polymers are suitable the active semiconducting layers for OFET applications. Owing to their crystallinity, strong intermolecular interactions between large π-conjugated systems generally lead to a high charge-carrier mobility. The development of high performance OFETs have attracted considerable attention in the materials/electronics community over the past two decades with high potential applications, such as radio frequency identification tags, driver circuits for flexible displays, sensors and nonvolatile memories. However, their practical applications are often limited by the relatively low field-effect mobility (μ_{FET}), caused by a poor quality of organic thin film, compared to widely used single-crystal silicon.[15]

The key points for development of high mobility OFETs have been highlighted from aspects of appropriate molecular engineering, process engineering and interface engineering. Based on these considerations, historically there have been more examples of good *p*-channel materials than *n*-channel materials for OFETs. The observation of a low *n*-channel mobility is generally the result of the extrinsic effects, such as the presence of specific traps for electrons (due to photo-oxidation of the π-conjugated backbone) or the instability of radical-anions towards water, hydroxyl groups, or oxygen.[16] However, unipolar *n*-channels and *n*-channel-dominant ambipolar (i.e., they conduct holes and electrons) OFETs are essential for developing low-power complementary integrated circuits that utilize both positive and negative gate voltages to turn transistors on and off. This can be achieved by introducing strong electron-withdrawing substituents such as fluorine, cyano, or diimide moieties into the conjugated backbone.[16-19] Its backbone turns into electron deficient states, which results in the increment of electron affinity and the decrement of LUMO energy levels.

Semiconductor/dielectric interface, another crucial important interface in OFETs, significantly affects the efficiency of charge transport through the channel region. Since charge carrier transport in OFETs is mainly located in the first few monolayers of an organic layer next to the dielectric surface, especially in a bottom-gate configuration, the properties of dielectric surface affects the growth and the morphology of the semiconducting layer, which in turn determines the whole device carrier mobility. By adding an interfacial layer between the semiconductor and the underlying substrate, the interface properties can be effectively controlled for favourable mesoscale/nanoscale ordering of the organic semiconducting layer. Accordingly, many studies have focused on surface modifications such as a self-assembled monolayer (SAM) or a thin polymeric layer on inorganic gate dielectrics.[20-23] It is generally known that the dielectric films should possess low trapping density at the surface, low surface roughness, low impurity concentration, and good compatibility with organic semiconductors.

ULSAN NATIONAL INSTITUTE OF SCIENCE AND TECHNOLOGY

1.3. Sensor Applications of Nanoscopically Engineered Organic Semiconductors

In addition to typical switching elements for logic circuits, OFETs can be utilized as sensor platforms. In general, OFET-based sensors and detectors show output electrical signals responding to the amount of target species diffused into the channel region, where the signals can be further modulated by applying additional gate field.[24] Their amplification features of detected signals are obtained by tuning the applied voltage on the third electrode (i.e., gate terminal), leading to higher sensitivity compared to conventional sensors that have two electrodes. Furthermore, a relatively high mobility OFET can facilitate a superior signal amplification and high response speed of an OFET sensor. Aiming to improve the sensing capability, structure and morphology of the semiconducting layer need to be specifically controlled to effectively detect the target analytes. For example, enhancing film durability against mechanical force is required for pressure sensors, and light pathways need to be adjusted for photodetectors.

Progress in research on OFET-based sensors has been greatly accelerated with sensing a wide range of analytes including chemical compounds,[25, 26] biological species,[27, 28] pressure,[8, 29] and light,[30, 31] as well as for food.[32]. **Figure 1.3** shows the schematic of typical organic-transistor-based sensors. The sensor response is closely related to charge transport in the device, which can be influenced by analyte dipole-induced charge trapping at grain boundaries. In some cases, the analyte dipoles lead to an increase in device current, because of more charges being induced in the channel. Organic materials with more grain boundaries result in higher sensitivity in OFET-based sensors, which typically occurs from the fact that the grain boundaries generally afford pathways for the diffusion of analytes into the channel region of the transistor.[7, 9] However, as grain boundaries[33] and dislocations[34] prevent efficient charge-carrier transport on the device performance, reducing such disorders in molecular packing has been extensively studied.[15, 35-37] In OFET-based sensors, the device architecture often limits their performance by blocking the efficient diffusion of analytes into the active channel region. Their physical structure can be controlled effectively by the properties of the semiconductor/dielectric interface. Controlling this interface has always been an important topic in the organic electronics community. Therefore, structurally engineered-organic semiconducting films with vertical porous structures that do not degrade charge transport may provide more efficient and direct pathways, which eventually lead to fast response and high sensitivity toward target analytes.

Actually, despite the above their high sensitivity, pristine OFET-based sensors without additional functionalization often exhibit low selectivity for target analytes because all elements, including analytes and impurities that typically diffuse into the channel region through grain boundaries, can contribute to changes in the detected signal. Therefore, highly selective detection with OFET-based sensors for real applications often requires chemical modification or immobilization of specific receptors on a device surface to capture target analytes.[7, 24, 38-41] General OFET-based sensors have utilized anchoring group and enzyme immobilization for enhanced selectivity of metabolic processes

ULSAN NATIONAL INSTITUTE OF SCIENCE AND TECHNOLOGY

so far. These systems still have shortcomings such as high cost, lack of long-term stability, and complicated fabrication processes. The sensors based on specific synthetic receptor-engineered OFET are a highly promising alternative to classical methods employing enzyme immobilization due to their high selectivity and sensitivity, and can provide a low cost, simple, and viable approach for the fabrication of high-performance OFET-based sensors. Their outstanding performance of sensor devices is expected due to the commendable combination of highly selective synthetic receptors and highly sensitive OFET devices. Furthermore, the sensitivity, stability, and selectivity of sensors can be optimized by choosing or engineering more suitable fabrication techniques and materials for the active layers of the devices. Such on-demand, structure-engineered, and surface-engineered organic semiconducting layers are highly desirable for practical applications of OFETs.

Remarkable progress in nanoscopically engineered organic-transistor-based sensors is of great importance for widespread applications as they surprisingly exhibit enhanced sensitivity, stability, and selectivity of the devices, which are core requirements of sensors.

ULSAN NATIONAL INSTITUTE OF SCIENCE AND TECHNOLOGY

1.4. References

[1] Natali D., Caironi M., *Adv. Mater.* **2012**, *24*, 1357-1387.
[2] Yan H.; Chen Z.; Zheng Y.; Newman C.; Quinn J. R.; Dotz F.; Kastler M., Facchetti A., *Nature* **2009**, *457*, 679-686.
[3] Mei Y.; Loth M. A.; Payne M.; Zhang W.; Smith J.; Day C. S.; Parkin S. R.; Heeney M.; McCulloch I.; Anthopoulos T. D.; Anthony J. E., Jurchescu O. D., *Adv. Mater.* **2013**, *25*, 4352-4357.
[4] Yamashita Y., *Sci. Technol. Adv. Mater.* **2009**, *10*, 024313.
[5] Tsao H. N.; Cho D. M.; Park I.; Hansen M. R.; Mavrinskiy A.; Yoon D. Y.; Graf R.; Pisula W.; Spiess H. W., Müllen K., *J. Am. Chem. Soc.* **2011**, *133*, 2605-2612.
[6] Tsiminis G.; Wang Y.; Kanibolotsky A. L.; Inigo A. R.; Skabara P. J.; Samuel I. D. W., Turnbull G. A., *Adv. Mater.* **2013**, *25*, 2826-2830.
[7] Torsi L.; Farinola G. M.; Marinelli F.; Tanese M. C.; Omar O. H.; Valli L.; Babudri F.; Palmisano F.; Zambonin P. G., Naso F., *Nat. Mater.* **2008**, *7*, 412-417.
[8] Mannsfeld S. C. B.; Tee B. C. K.; Stoltenberg R. M.; Chen C. V. H. H.; Barman S.; Muir B. V. O.; Sokolov A. N.; Reese C., Bao Z. N., *Nat. Mater.* **2010**, *9*, 859-864.
[9] Angione M. D.; Cotrone S.; Magliulo M.; Mallardi A.; Altamura D.; Giannini C.; Cioffi N.; Sabbatini L.; Fratini E.; Baglioni P.; Scamarcio G.; Palazzo G., Torsi L., *Proc. Natl. Acad. Sci. U.S.A.* **2012**, *109*, 6429-6434.
[10] Sun Y.; Welch G. C.; Leong W. L.; Takacs C. J.; Bazan G. C., Heeger A. J., *Nat. Mater.* **2012**, *11*, 44-48.
[11] Gao L.; Zhang Z.-G.; Bin H.; Xue L.; Yang Y.; Wang C.; Liu F.; Russell T. P., Li Y., *Adv. Mater.* **2016**, *28*, 8288-8295.
[12] Sekitani T.; Yokota T.; Zschieschang U.; Klauk H.; Bauer S.; Takeuchi K.; Takamiya M.; Sakurai T., Someya T., *Science* **2009**, *326*, 1516-1519.
[13] Chang J.; Zhang X.; Ge T., Zhou J., *Org. Electron.* **2014**, *15*, 701-710.
[14] Amir R.; Tomoyuki Y.; Tsuyoshi S., Takao S., *Appl. Phys. Express* **2015**, *8*, 091601.
[15] Minemawari H.; Yamada T.; Matsui H.; Tsutsumi J.; Haas S.; Chiba R.; Kumai R., Hasegawa T., *Nature* **2011**, *475*, 364-367.
[16] Jones B. A.; Facchetti A.; Wasielewski M. R., Marks T. J., *J. Am. Chem. Soc.* **2007**, *129*, 15259-15278.
[17] Yuan Z.; Ma Y.; Geßner T.; Li M.; Chen L.; Eustachi M.; Weitz R. T.; Li C., Müllen K., *Org. Lett.* **2016**, *18*, 456-459.
[18] Lee J.; Jang M.; Lee S. M.; Yoo D.; Shin T. J.; Oh J. H., Yang C., *ACS Appl. Mater. Interfaces* **2014**, *6*, 20390-20399.
[19] Oh J. H.; Suraru S. L.; Lee W.-Y.; Könemann M.; Höffken H. W.; Röger C.; Schmidt R.; Chung Y.; Chen W.-C.; Würthner F., Bao Z., *Adv. Funct. Mater.* **2010**, *20*, 2148-2156.
[20] Yang H. C.; Shin T. J.; Ling M. M.; Cho K.; Ryu C. Y., Bao Z. N., *J. Am. Chem. Soc.* **2005**, *127*, 11542-11543.
[21] Watanabe M.; Chang Y. J.; Liu S. W.; Chao T. H.; Goto K.; Islam M. M.; Yuan C. H.; Tao Y. T.; Shinmyozu T., Chow T. J., *Nat. Chem.* **2012**, *4*, 574-578.
[22] Liao K. C.; Ismail A. G.; Kreplak L.; Schwartz J., Hill I. G., *Adv. Mater.* **2010**, *22*, 3081-3085.
[23] Klauk H.; Zschieschang U.; Pflaum J., Halik M., *Nature* **2007**, *445*, 745-748.
[24] Someya T.; Dodabalapur A.; Huang J.; See K. C., Katz H. E., *Adv. Mater.* **2010**, *22*, 3799-3811.
[25] Sessolo M.; Rivnay J.; Bandiello E.; Malliaras G. G., Bolink H. J., *Adv. Mater.* **2014**, *26*, 4803-4807.
[26] Roberts M. E.; Mannsfeld S. C. B.; Queraltó N.; Reese C.; Locklin J.; Knoll W., Bao Z., *Proc. Natl. Acad. Sci. U.S.A.* **2008**, *105*, 12134-12139.
[27] Hammock M. L.; Knopfmacher O.; Naab B. D.; Tok J. B. H., Bao Z., *ACS Nano* **2013**, *7*, 3970-3980.
[28] Sokolov A. N.; Roberts M. E., Bao Z., *Mater. Today* **2009**, *12*, 12-20.
[29] Ramuz M.; Tee B. C. K.; Tok J. B. H., Bao Z., *Adv. Mater.* **2012**, *24*, 3223-3227.
[30] Yu H.; Bao Z., Oh J. H., *Adv. Funct. Mater.* **2013**, *23*, 629-639.
[31] Guo Y.; Du C.; Yu G.; Di C.-a.; Jiang S.; Xi H.; Zheng J.; Yan S.; Yu C.; Hu W., Liu Y., *Adv.*

ULSAN NATIONAL INSTITUTE OF SCIENCE AND TECHNOLOGY

Funct. Mater. **2010**, *20*, 1019-1024.
[32] Bartic C., Borghs G., *Anal. Bioanal. Chem.* **2006**, *384*, 354-365.
[33] Rivnay J.; Jimison L. H.; Northrup J. E.; Toney M. F.; Noriega R.; Lu S. F.; Marks T. J.; Facchetti A., Salleo A., *Nat. Mater.* **2009**, *8*, 952-958.
[34] Nickel B.; Barabash R.; Ruiz R.; Koch N.; Kahn A.; Feldman L. C.; Haglund R. F., Scoles G., *Phys. Rev. B* **2004**, *70*, 125401-125407.
[35] Ruiz R.; Choudhary D.; Nickel B.; Toccoli T.; Chang K. C.; Mayer A. C.; Clancy P.; Blakely J. M.; Headrick R. L.; Iannotta S., Malliaras G. G., *Chem. Mater.* **2004**, *16*, 4497-4508.
[36] Zhang J.; Rabe J. P., Koch N., *Adv. Mater.* **2008**, *20*, 3254-3257.
[37] Kang B.; Jang M.; Chung Y.; Kim H.; Kwak S. K.; Oh J. H., Cho K., *Nat. Commun.* **2014**, *5*, 4752.
[38] Sokolov A. N.; Roberts M. E.; Johnson O. B.; Cao Y., Bao Z., *Adv. Mater.* **2010**, *22*, 2349-2353.
[39] Yoon H.; Ko S., Jang J., *J. Phys. Chem. B* **2008**, *112*, 9992-9997.
[40] Khan H. U.; Roberts M. E.; Johnson O.; Knoll W., Bao Z., *Org. Electron.* **2012**, *13*, 519-524.
[41] Mulla M. Y.; Tuccori E.; Magliulo M.; Lattanzi G.; Palazzo G.; Persaud K., Torsi L., *Nat. Commun.* **2015**, *6*, 6010.

ULSAN NATIONAL INSTITUTE OF SCIENCE AND TECHNOLOGY

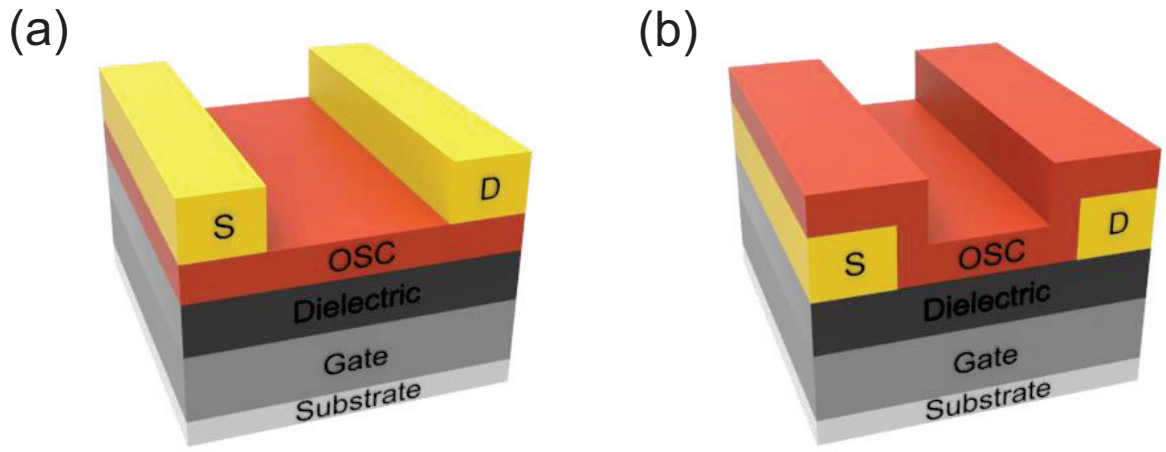

Figure 1.1. Schematic diagrams of two bottom-gate OFET configurations: a) top-contact and b) bottom contact. OSC, organic semiconductor; S, source; D, drain.

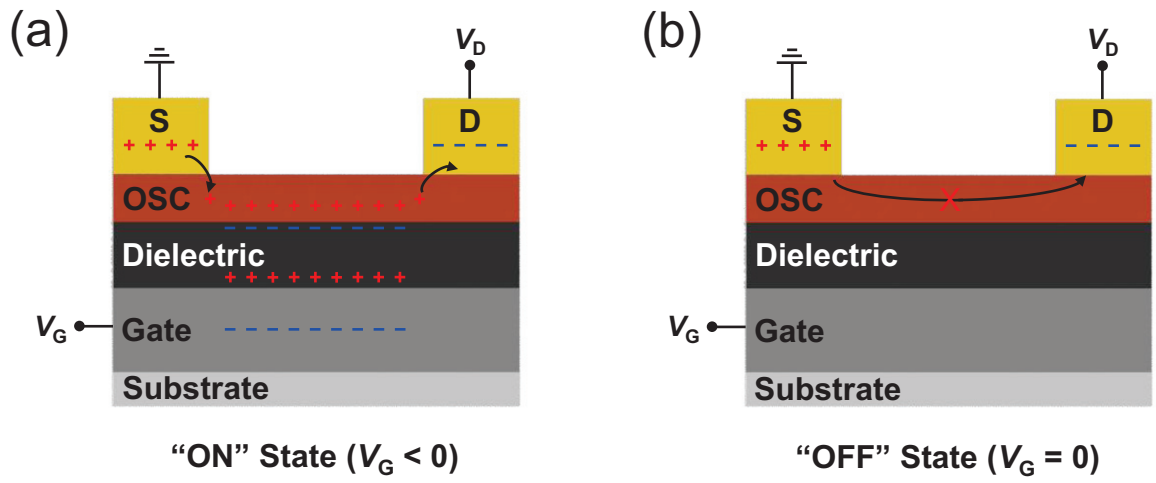

Figure 1.2. Simplified illustration of the operation principle of an OFET with *p*-channel semiconductor. OSC, organic semiconductor; S, source; D, drain.

ULSAN NATIONAL INSTITUTE OF SCIENCE AND TECHNOLOGY

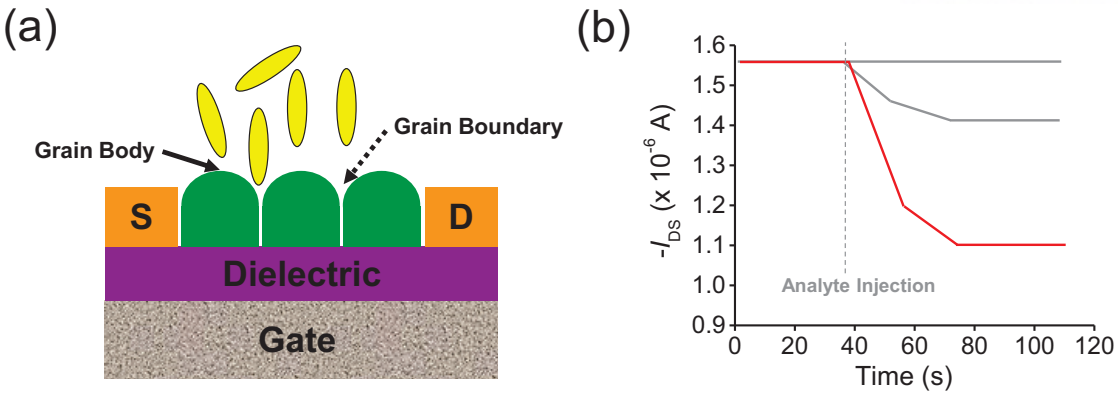

Figure 1.3. a) Schematic diagram of organic-transistor-based sensors. b) Typical device response upon exposure to analyte. The semiconductor used is *p*-channel material. Color code: OSC, green.

ULSAN NATIONAL INSTITUTE OF SCIENCE AND TECHNOLOGY

Chapter 2

Investigation of Charge-Transport Properties in Fluorinated DPP-Benzothiadiazole (BT) Polymer Semiconductors

Abstract

Over the past few years, one of the most remarkable advances in the field of polymer solar cells (PSCs) has been the development of fluorinated 2,1,3-benzothiadiazole (BT)-based polymers that lack the solid working principles of previous designs, but boost the power conversion efficiency. To assess a rich data set for the influence of the fluorinated BT units on the charge-transport characteristics in organic field-effect transistors (OFETs), we synthesized two new polymers (PDPP-FBT and PDPP-2FBT) incorporating diketopyrrolopyrrole (DPP) and either single- or double-fluorinated BT and thoroughly investigated them via a range of techniques. Unlike the small differences in the absorption properties of PDPP-FBT and its non-fluorinated analogue (PDPP-BT), the introduction of doubly fluorinated BT into the polymer backbone induces a noticeable change in its optical profiles and energy levels, which results in a slightly wider bandgap and deeper HOMO for PDPP-2FBT, relative to the others. Grazing incidence X-ray diffraction (GIXD) analysis reveals that both fluorinated polymer films have long-range orders along the out-of-plane direction, and π–π stacking in the in-plane direction, implying semicrystalline lamellar structures with edge-on orientations in the solid state. Thanks to the strong intermolecular interactions and highly electron-deficient π-systems driven by the inclusion of F atoms, the polymers exhibit electron mobilities of up to 0.42 and 0.30 $cm^2 V^{-1} s^{-1}$ for PDPP-FBT and PDPP-2FBT, respectively, while maintaining hole mobilities higher than 0.1 $cm^2 V^{-1} s^{-1}$. Our results highlight that the use of fluorinated BT blocks in the polymers is a promising molecular design strategy for improving electron transporting performance without sacrificing their original hole mobility values.

ULSAN NATIONAL INSTITUTE OF SCIENCE AND TECHNOLOGY

2.1. Introduction

The use of solution-processable semiconducting polymers for organic field-effect transistors (OFETs) continues to attract considerable interest since polymeric systems can offer the possibility of cheap raw materials, low processing costs, excellent film formation, and mechanical properties such as flexibility and large-area uniformity.[1-12] Recently, diketopyrrolopyrrole (DPP)-based donor–acceptor (D-A) polymers have been widely developed, and have proven themselves to be one of the most promising semiconductors for high-performance unipolar *p*-channels and *p*-channel-dominant ambipolar OFETs (with hole mobilities exceeding 3 $cm^2\ V^{-1}s^{-1}$).[13-18] Nonetheless, the development of DPP-based polymers with high-performance *n*-channel charge transport has lagged behind that of the aforementioned *p*-channel dominant polymers, primarily due to the inherent instability of the electron charge carriers in the presence of ambient oxidants such as O_2, H_2O, or O_3.[9]

The research efforts of our groups have recently focused on developing high electron-affinity polymers based on DPP, using a structural modification of the conventionally-used 2,1,3-benzothiadiazole (BT) acceptor moiety. For example, by copolymerizing with a stronger acceptor bis-benzothiadiazole (BBT) unit relative to BT, the resulting polymer (PDPP-BBT) showed even *n*-channel dominant characteristics, yet yielded unsatisfactory electron mobility results ($\sim 10^{-3}\ cm^2\ V^{-1}s^{-1}$).[19] In the meantime, many other groups have often highlighted the use of fluorinated BT units into the polymer backbone, and demonstrated improved photovoltaic performance.[20-27] Although the cause of the efficiency improvement varies noticeably depending upon the specific systems, it is generally recognized that the inclusion of fluorine (F) atoms can not only fine-tune the energy levels of polymers, but also promote non-covalent interactions through C-F···H, F···S on mesoscopic solid-state structures.[26-28] In addition, it is well known that the strong electron-withdrawing nature of F atoms allows for efficient electron injection into the LUMO and increases hydrophobicity, which can increase the electron affinity and environmental stability of semiconductors in OFET operations, relative to their fluorine-free analogues.[29-34]

These early results motivated us to design DPP-based polymers containing the ubiquitous fluorinated BT blocks (FBT (1F) and 2FBT (2F)), with a view to assessing semiconductors with high electron mobility and high environmental stability. Herein, as an attempt to investigate the effects of fluorinated BT blocks on the charge-carrier transport properties in OFETs, we report on the synthesis and characterization of *poly(3,6-dithien-2-yl-2,5-di(2-octyldodecyl)-pyrrolo[3,4-c]pyrrole-1,4-dione-5',5''-diyl-alt-fluorobenzo 2,1,3-thiadiazol-4,7-diyl]* and *poly(3,6-dithien-2-yl-2,5-di(2-octyldodecyl)-pyrrolo[3,4-c]pyrrole-1,4-dione-5',5''-diyl-alt-difluorobenzo 2,1,3-thiadiazol-4,7-diyl]* (PDPP-FBT and PDPP-2FBT, see **Scheme 2.1**), and show the differences in their optophysical and redox properties, molecular packings, and OFET performances. Furthermore, we elucidate how the degree of the substitution of F atoms on a BT unit affects the charge-carrier mobilities and the dynamics of dominant

ULSAN NATIONAL INSTITUTE OF SCIENCE AND TECHNOLOGY

polarity by comparison with a non-fluorinated analogue (PDPP-BT), and finally discuss the overall structure–property relationship.

2.2. Experimental Section

General procedures and methods: All starting materials were purchased either from Aldrich or Acros and used without further purification. All solvents are ACS grade unless otherwise noted. Anhydrous THF was obtained by distillation from sodium/benzophenone prior to use. Anhydrous toluene was used as received. 3,6-Bis-(5-(4,4,5,5-tetramethyl-1,3,2-dioxaborolan-thiophene-2-yl)-2,5-bis(2-octyldodecyl)-pyrrolo[3,4-*c*]pyrrole-1,4-dione (DPP) was prepared according to established literature procedures.[35] UV-Vis-NIR spectra were taken on Cary 5000 (Varian USA) spectrophotometer. Microwave reactions were performed by Microwave Synthesis Reactor (Microwave, Anton Paar). DFT calculations were performed using the Gaussian 09 package with the nonlocal hybrid Becke three-parameter Lee-Yang-Parr (B3LYP) function and the 6-311G basis set to elucidate the HOMO and LUMO levels after optimizing the geometry of DPP-BT, DPP-FBT, and DPP-2FBT trimer using the same method and time-dependenct self-consistent filed (TD-SCF) approximation was used for excited state dipole moment. Number-average (M_n) and weight average (M_w) molecular weights, and polydispersity index (PDI) of the polymer products were determined by gel permeation chromatography (GPC) with Waters 150C GPC using a series of mono disperse polystyrene as standards in THF (HPLC grade). Cyclic voltammetry (CV) measurements were performed on Solartron electrochemical station (METEK, Versa STAT3) with a three-electrode cell in a 0.1 M tetra-*n*-butylammonium hexafluorophosphate (*n*-Bu_4NPF_6) solution in acetonitrile at a scan rate of 100 mV/s at room temperature under argon. Ag/Ag^+ electrode, a platinum wire and a glass carbon disk were used as the reference electrode, counter electrode, and working electrode, respectively. The HOMO energy levels were obtained from the equation HOMO (eV) = − ($E_{(ox)}^{onset}$ + 4.4). The LUMO levels of polymers were obtained from the equation LUMO (eV) = − ($E_{(red)}^{onset}$ + 4.4). Ultraviolet photoelectron spectroscopy (UPS) was examined by AXIS-NOVA CJ109, Kratos. The polymer solution was prepared in chloroform with 5 mg mL^{-1} for PDPP-BT, PDPP-FBT, and PDPP-2FBT. The PDPP-BT, PDPP-FBT, and PDPP-2FBT solution was spin-coated on indium tin oxide (ITO) glass films, respectively. Film fabrication was done in a N_2-atmosphere glovebox. The UPS analysis chamber was equipped with a hemispherical electron-energy analyzer (Kratos Ultra Spectrometer), and was maintained at 1.0×10^{-9} Torr. The UPS measurements were carried out using the He I ($h\nu$ = 21.2 eV) source. Thermogravimetric analysis (TGA) was performed by Simutaneous DSC/TGA instrument (TA Instruments, USA) at the heating rate of 10 ^oC min^{-1}. Differential scanning calorimetry (DSC) curves were recorded by Differential Scanning Calorimeter (TA Instruments, USA) at the heating rate of 10 ^oC min^{-1}.

ULSAN NATIONAL INSTITUTE OF SCIENCE AND TECHNOLOGY

OFETs device fabrication and characterization: OFETs were fabricated in the top-contact bottom-gate configuration using a SiO_2/Si wafer. A 300-nm-thick SiO_2 layer (capacitance per unit area, C_i = 10 nF cm^{-2}) and the underlying highly n-doped Si (< 0.004 Ω·cm) were utilized as the gate dielectric and the gate electrode, respectively. The SiO_2 surface was modified with *n*-octadecyltrimethoxysilane (OTS) based self-assembled monolayer (SAM). Prior to the treatment of OTS SAM, the SiO_2 surface contamination was removed using Piranha (H_2SO_4 + H_2O_2) solution. The SiO_2/Si substrates were washed sequentially with deionized water and then used the UV-ozone treatment. The OTS solution (3 mM in trichloroethylene) was spin-coated on the cleaned substrate at 3000 rpm then, the substrates placed in a vacuum desiccator with NH_4OH vapor for overnight. The OTS solution treatment was used to remove OH groups from the SiO_2 surface, and to optimize dielectric/semiconductor interface. The SiO_2/Si substrates were washed with toluene, acetone, and isopropyl alcohol and dried by blowing nitrogen gas. The polymeric semiconducting layer was deposited on the cleaned substrates by drop casting. The polymer solution (~5 mg mL^{-1}) was prepared in 1,2,4-trichlorobenzene and filtered through a 0.22 μm syringe filter. The films were dried in vacuum oven at 100 °C to remove solvent residue. Then the PDPP-FBT and PDPP-2FBT thin films were annealed at 250 °C for 30 min on a hot plate. All the samples were fabricated inside a nitrogen-filled glovebox. A 40-nm thick gold layer was thermally deposited through a shadow mask to form the source and drain electrodes. OFETs have a channel length (L) of 50 μm and a channel width (W) of 1000 μm with W/L = 1000 μm/50 μm = 20. The transfer and output characteristics of ambipolar PDPP-FBT and PDPP-2FBT OFETs were measured by using a Keithley 4200 semiconductor parametric analyzer under nitrogen atmosphere. The carrier mobility was calculated in the saturated regime according to the equation:

$$I_{DS} = (W/2L)\mu C_i(V_G - V_T)^2$$

where I_{DS} is the drain current, W and L are the semiconductor channel width and length, respectively, μ is the mobility, C_i is the capacitance per unit area of the gate dielectric layer, and V_G and V_T are, respectively, the gate voltage and threshold voltage.

2,5-Bis(2-octhyldodecyl)-3,6-bis(5-(trimethylstannyl)thio-phen-2-yl) pyrrolo[3,4-c]pyrrole-1,4-dione (2): Compound **2** was prepared according to established literature procedures.[36] Isolated yield = 420 mg (87 %).

Typical Procedure for Suzuki coupling Polymerization and Polymer Purification: Boronic ester TDPP (0.20 mmol), dibromo FBT or 2FBT (0.20 mmol), tris(dibenzylidenacetone) dipalladium (0) (1.7 mg, 2.0 μmmol), anhydrous toluene (4 mL) were mixed in a Schlenk flask which was purged with argon for 30 minutes. To this solution, tri(*o*-tolyl)phosphine (1.2 mg, 4.0 μmol) and K_3PO_4 in demineralized water (2mL) were added and the reaction mixture was heated at 95 °C under vigorous stirring for 48 hours. The crude product was poured into a mixture of methanol (300 ml). The resulting solid was filtered off and subjected to sequential Soxhlet extraction with methanol (1 d), acetone (1 d) to remove

ULSAN NATIONAL INSTITUTE OF SCIENCE AND TECHNOLOGY

the low molecular weight fraction of the materials. The residue was extracted with chloroform in order to produce a dark purple product after precipitating again from methanol and drying *in vacuo*.

Poly(3,6-dithien-2-yl-2,5-di(2-octyldodecyl)-pyrrolo[3,4-c]pyrrole-1,4-dione-5',5''-diyl-alt-fluorobenzo 2,1,3-thiadiazol-4,7-diyl] (PDPP-FBT): Isolated yield of polymer PDPP-FBT = 100 mg (50 %). GPC analysis M_n = 6.1 kg/mol, M_w = 12.4 kg/mol, and PDI = 2.02 (against PS standard).

Poly(3,6-dithien-2-yl-2,5-di(2-octyldodecyl)-pyrrolo[3,4-c]pyrrole-1,4-dione-5',5''-diyl-alt-difluorobenzo 2,1,3-thiadiazol-4,7-diyl] (PDPP-2FBT): Isolated yield of polymer PDPP-2FBT = 100 mg (50 %). GPC analysis M_n = 6.6 kg/mol, M_w = 10.9 kg/mol, and PDI = 1.66 (against PS standard).

Typical Procedure for Stille coupling Polymerization and Polymer Purification: Stannylated TDPP (0.20 mmol), dibromo FBT or 2FBT (0.20 mmol), tris(dibenzylidenacetone)dipalladium (0) (1.7 mg, 2.0 μmmol), anhydrous toluene (4 mL) were mixed in a 10mL of microwave vessel which was purged with argon for 30 minutes. To this solution, tri(*o*-tolyl)phosphine (1.2 mg, 4.0 μmol) was added and the reaction mixture was heated at 120 °C under vigorous stirring for 6 hours using microwave machine. The crude product was poured into a mixture of methanol (300 ml). The resulting solid was filtered off and subjected to sequential Soxhlet extraction with methanol (1 d), acetone (1 d), and hexane (1d) to remove the low molecular weight fraction of the materials. The residue was extracted with chloroform in order to produce a dark purple product after precipitating again from methanol and drying *in vacuo*.

Poly(3,6-dithien-2-yl-2,5-di(2-octyldodecyl)-pyrrolo[3,4-c]pyrrole-1,4-dione-5',5''-diyl-alt-fluorobenzo 2,1,3-thiadiazol-4,7-diyl] (PDPP-FBT): Isolated yield of polymer PDPP-FBT = 150 mg (75 %). GPC analysis M_n = 24.0 kg/mol, M_w = 48.2kg/mol, and PDI = 2.01 (against PS standard).

Poly(3,6-dithien-2-yl-2,5-di(2-octyldodecyl)-pyrrolo[3,4-c]pyrrole-1,4-dione-5',5''-diyl-alt-difluorobenzo 2,1,3-thiadiazol-4,7-diyl] (PDPP-2FBT): Isolated yield of polymer PDPP-2FBT = 150 mg (75 %). GPC analysis M_n = 25.0 kg/mol, M_w = 58.6 kg/mol, and PDI = 2.34 (against PS standard). The polymers were synthesized by Dr. Junghoon Lee and Prof. Changduk Yang, UNIST.

2.3. Results and Discussion

2.3.1. Synthetic Strategies, Synthesis, and Characterization

The fluorinated BT (FBT and 2FBT) and diboronic ester DPP derivatives were easily synthesized according to the established methods.[26, 35] Polymerization of the FBT and 2FBT monomers using standard palladium(0)-catalyzed Suzuki polycondensation with the diboronic ester co-monomer produced the corresponding polymers (PDPP-FBT and PDPP-2FBT). However, the number-average molecular weight (M_n) was below 10 kDa with a polydispersity index (PDI) of approximately 2.5 for both the polymers, as determined by gel permeation chromatography (GPC) in THF after Soxhlet purification. It has been reported that a high molecular weight can play an important role in achieving nanometer-sized interconnected morphologies, hence resulting in efficient channels for charge-carrier

ULSAN NATIONAL INSTITUTE OF SCIENCE AND TECHNOLOGY

transport via a hopping mechanism.[11, 37, 38] Thereby, the observed relatively low molecular weights prompted us to screen various Suzuki coupling conditions, such as the utilization of a microwave-assisted heating protocol, the use of tiny amounts of catalyst, varying the solution concentration, the replacement of $Pd(PPh_3)_4$ with $Pd_2(dba)_3$ as a catalyst, and different ligand/palladium ratios, in order to improve the molecular weights. Nevertheless, the attempted synthesis of the polymers by Suzuki polymerization only afforded undesired low molecular weight materials, possibly due to either the competing base- and/or metal-catalyzed protodeborylation of the electron-rich thiophenes adjacent to the DPP monomer under our reaction conditions.[39-42] In addition, we found no appreciable difference in the molecular weight, even if the monomer was diiodo BT. Therefore, we decided to apply a Stille polycondensation instead of the Suzuki one, because the Stille-coupling reaction is generally recognized as a better alternative to the Suzuki protocol, when electron-rich species (thiophenes or pyrroles) are coupled.[43, 44] Thus, the key DPP monomer, distannyl DPP was prepared by lithiation using diisopropylamide (LDA) and subsequent quenching with trimethyltin chloride. Stille polymerization under microwave heating conditions was employed to form the PDPP-FBT and PDPP-2FBT respectively, which indeed proceeded in good yields (75–80%), with sufficiently high molecular weights (M_n of 24.0 kDa and 25.0 kDa with PDIs of 2.01 and 2.34 for PDPP-FBT and PDPP-2FBT respectively, as determined by GPC and THF eluent). Both polymers were soluble in common organic solvents such as tetrahydrofuran, chloroform, toluene, and chlorobenzene.

The UV-vis-NIR absorption spectra of the polymers in chloroform solution and in a solid state are shown in **Figure 2.1a** and **2.1b**. The absorption data are listed in **Table 2.1**. Upon changing from solutions to films, the absorption peaks for both polymers are not only red-shifted (~20 nm) and broadened to some extent, but also their low-energy shoulder bands at the range of 870–910 nm are intensified, presumably because of the occurrence of the aggregation or π–π stacking in solid state. This is a common phenomenon for rigid conjugated polymers.[45, 46] Very interestingly, although the spectral profile of PDPP-FBT is nearly identical to that of the non-fluorinated PDPP-BT (See **Figure 2.2**),[45, 47] the increment in the number of F atoms from 1 to 2 on the repeating unit leads to a blue shift in the absorption onset (λ_{onset}) and maximum (λ_{max}) of the polymer. This results in a larger optical band gap of PDPP-2FBT (E_g^{opt} = 1.26 eV), which is 0.06 eV larger than that of PDPP-FBT (E_g^{opt} = 1.20 eV). Therefore, one can conclude that the inclusion of one F atom on the BT unit of PDPP-BT hardly affects the absorption characteristics, but the incorporation of two F atoms can alter the intrinsic optical properties, compared to the non-fluorinated PDPP-BT.

Cyclic voltammetry (CV) reveals reversible oxidation/reduction behaviors for both polymers, with the PDPP-2FBT being oxidized at a voltage that is 0.15 eV higher, relative to the PDPP-FBT (**Figure 2.1c**). In addition, the ionization potential (IP) values of each polymer measured by ultraviolet photoelectron spectroscopy (UPS) (**Figure 2.1d** and **Table 2.1**) show similar trends with slight differences in their energy levels. On the other hand, the LUMO of PDPP-2FBT is -3.53 eV, which is

ULSAN NATIONAL INSTITUTE OF SCIENCE AND TECHNOLOGY

0.04 eV lower than that of PDPP-FBT (-3.49 eV), implying that doubly-fluorinated BT effectively lowers the HOMO level with only a minor effect on the LUMO.

The thermal properties of PDPP-FBT and PDPP-2FBT were investigated by thermogravimetric analyses (TGA), and differential scanning calorimetry (DSC). The combination of TGA and DSC data for the both polymers confirmed their good thermal stability without any phase transition processes (See **Figure 2.3**).

The computational calculations were carried out on the trimer systems of each polymer using density functional theory (DFT) with the B3LYP hybrid functional and the 6-311G(d) basis set, as implemented in Gaussian 09. **Figure 2.4** presents the adopted planar conformation with extremely small torsional angles for both cases, showing excellent co-planarity. In addition, both the HOMO and LUMO isosurfaces for the two model oligomers show delocalized characteristics, indicating the high possibility of ambipolar charge transport. Notably, upon taking a closer look at these structures, their HOMO isosurfaces were relatively more localized on the lateral axis π-systems, when compared to that observed for the non-fluorinated PDPP-BT (see **Figure 2.5**). Thereby, both fluorinated polymers would strengthen their electron charge-carrier transport and be expected to afford *n*-channel dominant ambipolar OFETs, in line with our aforementioned hypothesis. After the optimization of the geometrical structures, time-dependent DFT (TD-DFT) calculations for the polymer repeating unit were also performed for the analysis of the backbone chain dipole dependence (**Table 2.2**). The single unit of PDPP-FBT shows a larger change in dipole on transition from the ground to excited states ($\Delta\mu_{ge}$) than that of PDPP-2FBT, most likely due to the asymmetry-induced odd-numbered F-substitute on BT motif (see **Figure 2.6** and **Table 2.2**). Even though the current level of the theory above can only provide general trends, this database would be a useful benchmark for predicting the effect of more subtle structural modifications with fluorination for conjugated polymers.

2.3.2 Thin-Film Microstructure Analysis

The film morphologies of fluorine-substituted conjugated polymers were examined using tapping-mode atomic force microscopy (AFM). The polymer films were drop-casted onto *n*-octadecyltrimethoxysilane (OTS)-modified SiO_2/Si substrate from the polymer solution (~5 mg mL^{-1}) using 1,2,4-trichlorobenzene (b.p. = 214 °C) as the solvent. The drop-casting method typically provides a longer drying time than a spin-coating technique and enables the formation of films with a higher degree of crystallinity. The use of solvents with high-boiling points is known to be beneficial for forming higher crystallinity structures and larger crystal sizes, typically leading to enhanced performance in OFETs.[48-51] The drop-cast PDPP-FBT and PDPP-2FBT films exhibited granular structures (**Figure 2.7**). Remarkably, the as-cast polymer films showed relatively larger void areas and more distinct grain boundaries between crystalline domains, whereas the polymer films that were annealed at 250 °C for 30 min exhibited interconnected granular domains with more smooth surfaces. The PDPP-2FBT film had smaller granular domains with a larger root-mean-square (RMS) roughness

ULSAN NATIONAL INSTITUTE OF SCIENCE AND TECHNOLOGY

value of 8.6 nm, compared with that (6.9 nm) of the PDPP-FBT film. In addition, the optimized drying time for the preparation of PDPP-FBT films was significantly longer (about 1.5 times) than that of the PDPP-2FBT films. A longer drying time typically leads to the formation of polymer films with enhanced crystallinity.[49-51]

Two-dimensional grazing incidence X-ray diffraction (2D GIXD) analyses of the drop-cast films were also performed to investigate the effects of the F-containing benzothiadiazole moieties of the DPP-based copolymers on the crystallinity and molecular packing further. **Figure 2.8** shows 2D GIXD images and the corresponding diffractogram profiles of the annealed PDPP-FBT and PDPP-2FBT films. The calculated crystallographic parameters are summarized in **Table 2.3**. PDPP-FBT and PDPP-2FBT both exhibited well-defined diffraction peaks up to *(300)* diffraction in the out-of-plane directions, indicating that fluorinated polymers have a long-range ordered lamellar packing. Both polymer films displayed strong (*100*) diffractions at q_z values of 0.28 and 0.27 $Å^{-1}$, corresponding to *d*-spacings of 22.8 and 23.4 Å, respectively. It is known that fluorine-sulfur interactions can facilitate the planarization of the polymer backbone, leading to a reduction in the intermolecular packing distances.[24, 48, 52] However, the *d*(*100*)-spacing of the PDPP-2FBT film was larger than that of the PDPP-FBT film. This is presumably due to the increase in the number of bulky F atoms and the electrostatic repulsion between F atoms.[53] PDPP-FBT and PDPP-2FBT showed discernible (*010*) diffraction peaks in the in-plane direction, which corresponded to π–π stacking (π-stack distance ~3.8 Å). These results indicate that both polymers have a strong preference for edge-on molecular orientations that are effective for charge transport between source and drain electrodes.[54] The annealed polymer films exhibited decreased *d*(*100*)-spacings and increased coherence lengths, when compared to those of the as-cast films (see **Figure 2.9** for the 2D GIXD images and the corresponding diffractogram profiles of the as-cast films). This indicates that the polymer films exhibit denser molecular packing after the thermal annealing.

2.3.3 OFET Performance

To investigate the electrical performance of F-substituted DPP-BT copolymers, top-contact bottom-gate OFET devices were constructed with PDPP-FBT and PDPP-2FBT films as the semiconducting layer. The details about OFET fabrication are included in the Experimental Section. **Figure 2.10** exhibits the typical V-shaped ambipolar characteristics of OFETs based on PDPP-FBT and PDPP-2FBT films after thermal annealing. *I-V* characteristics of the as-prepared films are also presented in **Figure 2.11**. The electrical performance characteristics such as charge carrier mobilities, on/off ratios, and threshold voltages are listed in **Table 2.4**. The electrical performance of the F-substituted DPP-BT copolymers was enhanced after thermal annealing. This is mainly due to the denser molecular packing characteristic after thermal annealing, as described in thin-film microstructure analysis. The enhancement in electron mobility was relatively larger than that of the hole mobility after the thermal annealing. It has been reported that the trap density of electrons by ambient oxidants commonly tends to decrease after proper thermal annealing, leading to enhanced electron mobility in ambipolar

ULSAN NATIONAL INSTITUTE OF SCIENCE AND TECHNOLOGY

semiconductors.[5, 55] As a control experiment, we also tested the electrical performance of PDPP-BT OFETs with gold contacts. The thermally annealed PDPP-BT OFETs exhibited hole-dominant ambipolar transport behaviors, with the optimized hole and electron mobilities of up to 0.11 and 0.076 $cm^2\ V^{-1}s^{-1}$, respectively (**Table 2.5**). In general, the injection barriers of electrons from the gold electrode (work function ~ 5.1 eV) to the LUMO were usually much larger than to the HOMO, due to the high-lying LUMO of the common polymer semiconductors, and the current flow is typically dominated by hole transport. In our experiment, the introduction of fluorine atoms into the main backbone of the BT unit effectively lowered the energy levels of the resulting polymers. The respective HOMO levels of the PDPP-BT, PDPP-FBT, and PDPP-2FBT are -5.10, -5.38, -5.48 eV, while their respective LUMO levels are -3.90, -4.18, and -4.22 eV, due to the increase in the number of electron-withdrawing fluorine substituents. Consequently, the hole injection barriers from gold to F-substituted polymers would increase, while the electron injection barriers would decrease. Therefore, both F-substituted polymers exhibited electron-dominant ambipolar transport behavior after optimization (Table 2.4). However, the PDPP-FBT films showed a better electrical performance than PDPP-2FBT films, despite their higher LUMO and HOMO energy levels that are less favorable for the electron charge-carrier transport. The OFETs based on annealed PDPP-FBT films exhibited the maximum electron and hole mobilities of 0.42 $cm^2\ V^{-1}\ s^{-1}$ and 0.21 $cm^2\ V^{-1}s^{-1}$, whereas the average electron and hole mobilities were 0.33 ± 0.05 and 0.15 ± 0.03 $cm^2\ V^{-1}s^{-1}$, respectively. On the other hand, the OFETs constructed with the annealed PDPP-2FBT films showed the maximum electron and hole mobilities of 0.30 $cm^2\ V^{-1}s^{-1}$ and 0.10 $cm^2\ V^{-1}s^{-1}$, with the average electron and hole mobilities of 0.19 ± 0.07 and 0.077 ± 0.021 $cm^2\ V^{-1}s^{-1}$, respectively. These results can be attributed to the morphological factors, rather than to the energy levels. As shown by AFM and GIXD results, the PDPP-FBT films exhibited denser molecular packing with much larger grains. These findings indicate that the charge transport in these fluorinated polymers is significantly affected by the morphological features, in addition to energetic factors.

Two ambipolar transistors based on fluorinated DPP-BT copolymers were integrated into the complementary metal-oxide-semiconductor (CMOS)-like inverters. **Figure 2.12** shows the output voltage (V_{OUT}) as a function of the input voltage (V_{IN}) at a constant supply voltage (V_{DD}) of 100V. The gate voltage is the circuit input voltage, which varies from 0 V to V_{DD}. At a small input voltage (V_{IN}), the *p*-channel transistor was on, and the *n*-channel transistor was off. The inverter of PDPP-FBT with high charge carrier mobilities of both holes and electrons exhibited a gain of 12. However, a higher gain value of 25 was recorded from the PDPP-2FBT inverters. Furthermore, the sharp switching of the circuits was shifted to nearly $V_{DD}/2$ in PDPP-2FBT. This result is most likely due to the higher symmetry of the threshold voltages of PDPP-2FBT transistors in *p*-and *n*-channel operation modes.[6, 56, 57]

ULSAN NATIONAL INSTITUTE OF SCIENCE AND TECHNOLOGY

2.4. Conclusion

Two conceptually identical polymers apart from having a different number of F atoms on their repeating unit (PDPP-FBT (one F) and PDPP-2FBT (two F)) are synthesized and carefully investigated in a comparative manner, in order to understand the effects of introducing fluorinated BT moieties into DPP polymers. While PDPP-FBT shows very similar optical properties to those of its non-fluorinated analog (PDPP-BT); interestingly, a noticeable change in the optical profiles and energy levels is observed by increasing the number of F atoms on the BT unit atom from 1 to 2, thereby resulting in a wider bandgap and deeper HOMO for PDPP-2FBT, relative to the others. In GIXD analysis, the films of both polymers appear to have strong lamellar textures with three out-of-plane peaks and a π–π stacking peak in the in-plane diffraction, indicating that the polymers adopt a preferential edge-on orientation relative to the substrates. To our delight, the fluorinated polymers FETs exhibited high electron mobilities of up to 0.42 $cm^2\ V^{-1}s^{-1}$, together with hole mobilities as high as 0.21 $cm^2\ V^{-1}s^{-1}$. These results are rationalized through a combination of the stronger intermolecular non-covalent interactions and higher electron-affinity π-systems, both of which can be induced from the F substituents. Not only does this study therefore provide new insights into charge-transport characteristics and our understanding of semiconducting polymers with incorporated fluorinated BT units, but also offers a powerful strategy for the molecular design of high-performance *n*-channel OFETs.

ULSAN NATIONAL INSTITUTE OF SCIENCE AND TECHNOLOGY

2.5. References

[1] Arias A. C.; MacKenzie J. D.; McCulloch I.; Rivnay J., Salleo A., *Chem. Rev.* **2010**, *110*, 3-24.
[2] Cheng Y.-J.; Yang S.-H., Hsu C.-S., *Chem. Rev.* **2009**, *109*, 5868-5923.
[3] Dhoot A. S.; Yuen J. D.; Heeney M.; McCulloch I.; Moses D., Heeger A. J., *Proc. Natl. Acad. Sci. U.S.A.* **2006**, *103*, 11834-11837.
[4] Forrest S. R., *Nature* **2004**, *428*, 911-918.
[5] Lee J.; Han A. R.; Kim J.; Kim Y.; Oh J. H., Yang C., *J. Am. Chem. Soc.* **2012**, *134*, 20713-20721.
[6] Lee J.; Han A. R.; Yu H.; Shin T. J.; Yang C., Oh J. H., *J. Am. Chem. Soc.* **2013**, *135*, 9540-9547.
[7] Liang Y., Yu L., *Acc. Chem. Res.* **2010**, *43*, 1227-1236.
[8] McCulloch I.; Heeney M.; Bailey C.; Genevicius K.; MacDonald I.; Shkunov M.; Sparrowe D.; Tierney S.; Wagner R.; Zhang W.; Chabinyc M. L.; Kline R. J.; McGehee M. D., Toney M. F., *Nat. Mater.* **2006**, *5*, 328-333.
[9] Murphy A. R., Fréchet J. M. J., *Chem. Rev.* **2007**, *107*, 1066-1096.
[10] Pan H.; Li Y.; Wu Y.; Liu P.; Ong B. S.; Zhu S., Xu G., *J. Am. Chem. Soc.* **2007**, *129*, 4112-4113.
[11] Tsao H. N.; Cho D. M.; Park I.; Hansen M. R.; Mavrinskiy A.; Yoon D. Y.; Graf R.; Pisula W.; Spiess H. W., Müllen K., *J. Am. Chem. Soc.* **2011**, *133*, 2605-2612.
[12] Yan H.; Chen Z.; Zheng Y.; Newman C.; Quinn J. R.; Dotz F.; Kastler M., Facchetti A., *Nature* **2009**, *457*, 679-686.
[13] Chen H.; Guo Y.; Yu G.; Zhao Y.; Zhang J.; Gao D.; Liu H., Liu Y., *Adv. Mater.* **2012**, *24*, 4618-4622.
[14] Kang I.; An T. K.; Hong J.-a.; Yun H.-J.; Kim R.; Chung D. S.; Park C. E.; Kim Y.-H., Kwon S.-K., *Adv. Mater.* **2013**, *25*, 524-528.
[15] Kang I.; Yun H.-J.; Chung D. S.; Kwon S.-K., Kim Y.-H., *J. Am. Chem. Soc.* **2013**, *135*, 14896-14899.
[16] Kanimozhi C.; Yaacobi-Gross N.; Chou K. W.; Amassian A.; Anthopoulos T. D., Patil S., *J. Am. Chem. Soc.* **2012**, *134*, 16532-16535.
[17] Li J.; Zhao Y.; Tan H. S.; Guo Y.; Di C.-A.; Yu G.; Liu Y.; Lin M.; Lim S. H.; Zhou Y.; Su H., Ong B. S., *Sci. Rep.* **2012**, *2*.
[18] Park J. H.; Jung E. H.; Jung J. W., Jo W. H., *Adv. Mater.* **2013**, *25*, 2583-2588.
[19] Lee J.; Cho S.; Seo J. H.; Anant P.; Jacob J., Yang C., *J. Mater. Chem.* **2012**, *22*, 1504-1510.
[20] Kim J.; Yun M. H.; Kim G.-H.; Lee J.; Lee S. M.; Ko S.-J.; Kim Y.; Dutta G. K.; Moon M.; Park S. Y.; Kim D. S.; Kim J. Y., Yang C., *ACS Appl. Mater. Interfaces* **2014**, *6*, 7523-7534.
[21] Albrecht S.; Janietz S.; Schindler W.; Frisch J.; Kurpiers J.; Kniepert J.; Inal S.; Pingel P.; Fostiropoulos K.; Koch N., Neher D., *J. Am. Chem. Soc.* **2012**, *134*, 14932-14944.
[22] Bronstein H.; Frost J. M.; Hadipour A.; Kim Y.; Nielsen C. B.; Ashraf R. S.; Rand B. P.; Watkins S., McCulloch I., *Chem. Mater.* **2013**, *25*, 277-285.
[23] Dutta G. K.; Kim T.; Choi H.; Lee J.; Kim D. S.; Kim J. Y., Yang C., *Poly. Chem.* **2014**, *5*, 2540-2547.
[24] Schroeder B. C.; Huang Z.; Ashraf R. S.; Smith J.; D'Angelo P.; Watkins S. E.; Anthopoulos T. D.; Durrant J. R., McCulloch I., *Adv. Funct. Mater.* **2012**, *22*, 1663-1670.
[25] Stuart A. C.; Tumbleston J. R.; Zhou H.; Li W.; Liu S.; Ade H., You W., *J. Am. Chem. Soc.* **2013**, *135*, 1806-1815.
[26] Zhang Y.; Chien S.-C.; Chen K.-S.; Yip H.-L.; Sun Y.; Davies J. A.; Chen F.-C., Jen A. K. Y., *Chem. Commun.* **2011**, *47*, 11026-11028.
[27] Zhou H.; Yang L.; Stuart A. C.; Price S. C.; Liu S., You W., *Angew. Chem. Int. Ed.* **2011**, *50*, 2995-2998.
[28] Xu Y.-X.; Chueh C.-C.; Yip H.-L.; Ding F.-Z.; Li Y.-X.; Li C.-Z.; Li X.; Chen W.-C., Jen A. K. Y., *Adv. Mater.* **2012**, *24*, 6356-6361.
[29] Dimitrakopoulos C. D., Malenfant P. R. L., *Adv. Mater.* **2002**, *14*, 99-117.

ULSAN NATIONAL INSTITUTE OF SCIENCE AND TECHNOLOGY

[30] Facchetti A.; Mushrush M.; Yoon M.-H.; Hutchison G. R.; Ratner M. A., Marks T. J., *J. Am. Chem. Soc.* **2004**, *126*, 13859-13874.
[31] Facchetti A.; Yoon M.-H.; Stern C. L.; Katz H. E., Marks T. J., *Angew. Chem. Int. Ed.* **2003**, *42*, 3900-3903.
[32] Heidenhain S. B.; Sakamoto Y.; Suzuki T.; Miura A.; Fujikawa H.; Mori T.; Tokito S., Taga Y., *J. Am. Chem. Soc.* **2000**, *122*, 10240-10241.
[33] Jones B. A.; Facchetti A.; Wasielewski M. R., Marks T. J., *J. Am. Chem. Soc.* **2007**, *129*, 15259-15278.
[34] Sirringhaus H.; Tessler N., Friend R. H., *Science* **1998**, *280*, 1741-1744.
[35] Bürckstümmer H.; Weissenstein A.; Bialas D., Würthner F., *J. Org. Chem.* **2011**, *76*, 2426-2432.
[36] Hu X.; Zuo L.; Fu W.; Larsen-Olsen T. T.; Helgesen M.; Bundgaard E.; Hagemann O.; Shi M.; Krebs F. C., Chen H., *J. Mater. Chem.* **2012**, *22*, 15710-15716.
[37] Gölitz P., *Angew. Chem. Int. Ed.* **2013**, *52*, 1-1.
[38] Zhao K.; Khan H. U.; Li R.; Su Y., Amassian A., *Adv. Funct. Mater.* **2013**, *23*, 6024-6035.
[39] Barder T. E.; Walker S. D.; Martinelli J. R., Buchwald S. L., *J. Am. Chem. Soc.* **2005**, *127*, 4685-4696.
[40] Billingsley K., Buchwald S. L., *J. Am. Chem. Soc.* **2007**, *129*, 3358-3366.
[41] Kinzel T.; Zhang Y., Buchwald S. L., *J. Am. Chem. Soc.* **2010**, *132*, 14073-14075.
[42] Martin R., Buchwald S. L., *Acc. Chem. Res.* **2008**, *41*, 1461-1473.
[43] Ahmed M.; Pisula W., Mhaisalkar S., *Molecules* **2012**, *17*, 12163-12171.
[44] Stille J. K., *Angew. Chem. Int. Ed.* **1986**, *25*, 508-524.
[45] Cho S.; Lee J.; Tong M.; Seo J. H., Yang C., *Adv. Funct. Mater.* **2011**, *21*, 1910-1916.
[46] Wallquist O., Lenz R., *Macromol. Symp.* **2002**, *187*, 617-630.
[47] Sonar P.; Singh S. P.; Li Y.; Soh M. S., Dodabalapur A., *Adv. Mater.* **2010**, *22*, 5409-5413.
[48] Lee W. Y.; Giri G.; Diao Y.; Tassone C. J.; Matthews J. R.; Sorensen M. L.; Mannsfeld S. C. B.; Chen W. C.; Fong H. H.; Tok J. B. H.; Toney M. F.; He M. Q., Bao Z. A., *Adv. Funct. Mater.* **2014**, *24*, 3524-3534.
[49] Chang J.-F.; Sun B.; Breiby D. W.; Nielsen M. M.; Sölling T. I.; Giles M.; McCulloch I., Sirringhaus H., *Chem. Mater.* **2004**, *16*, 4772-4776.
[50] Lin H.-W.; Lee W.-Y., Chen W.-C., *J. Mater. Chem.* **2012**, *22*, 2120-2128.
[51] Liu C.; Li Y.; Minari T.; Takimiya K., Tsukagoshi K., *Org. Electron.* **2012**, *13*, 1146-1151.
[52] Yum S.; An T. K.; Wang X.; Lee W.; Uddin M. A.; Kim Y. J.; Nguyen T. L.; Xu S.; Hwang S.; Park C. E., Woo H. Y., *Chem. Mater.* **2014**, *26*, 2147-2154.
[53] Schmidt R.; Ling M. M.; Oh J. H.; Winkler M.; Könemann M.; Bao Z., Würthner F., *Adv. Mater.* **2007**, *19*, 3692-3695.
[54] Kim K.-H.; Yu H.; Kang H.; Kang D. J.; Cho C.-H.; Cho H.-H.; Oh J. H., Kim B. J., *J. Mater. Chem. A* **2013**, *1*, 14538-14547.
[55] Oh J. H.; Sun Y.-S.; Schmidt R.; Toney M. F.; Nordlund D.; Könemann M.; Würthner F., Bao Z., *Chem. Mater.* **2009**, *21*, 5508-5518.
[56] Chen Z.; Lee M. J.; Shahid Ashraf R.; Gu Y.; Albert-Seifried S.; Meedom Nielsen M.; Schroeder B.; Anthopoulos T. D.; Heeney M.; McCulloch I., Sirringhaus H., *Adv. Mater.* **2012**, *24*, 647-652.
[57] Graz I. M., Lacour S. P., *Org. Electron.* **2010**, *11*, 1815-1820.

Reprinted with permission from J. Lee and M. Jang, *et al*., *ACS Appl. Mater. Interfaces*, **2014, *6*, 20390–20399. Copyright © 2014 American Chemical Society.

ULSAN NATIONAL INSTITUTE OF SCIENCE AND TECHNOLOGY

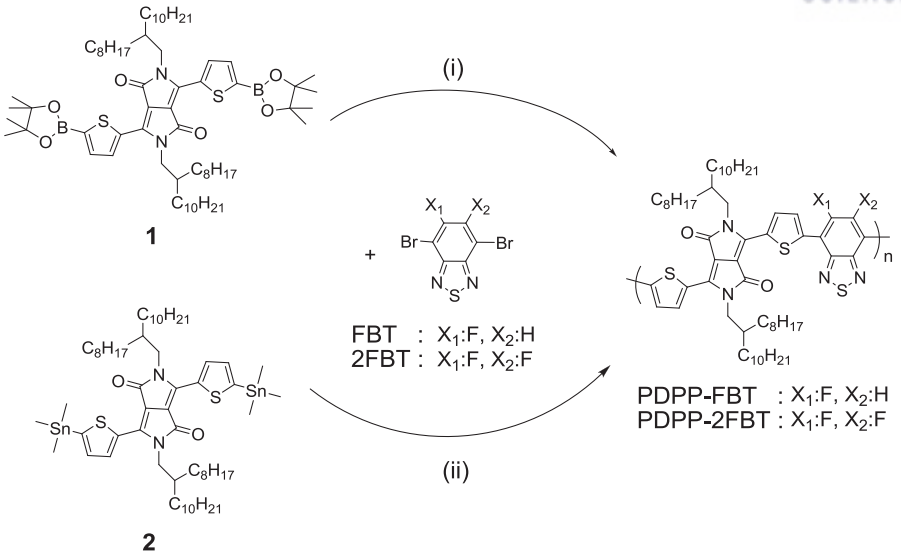

Scheme 2.1. Synthetic route to PDPP-FBT and PDPP-2FBT. [a]Suzuki polycondensation conditions (i): $Pd_2(dba)_3$, P(*o*-tolyl)$_3$, K_3PO_4, toluene/H_2O, 95 °C; Stille polycondensation conditions (ii): $Pd_2(dba)_3$, P(*o*-tolyl)$_3$, toluene, 120 °C, microwave.

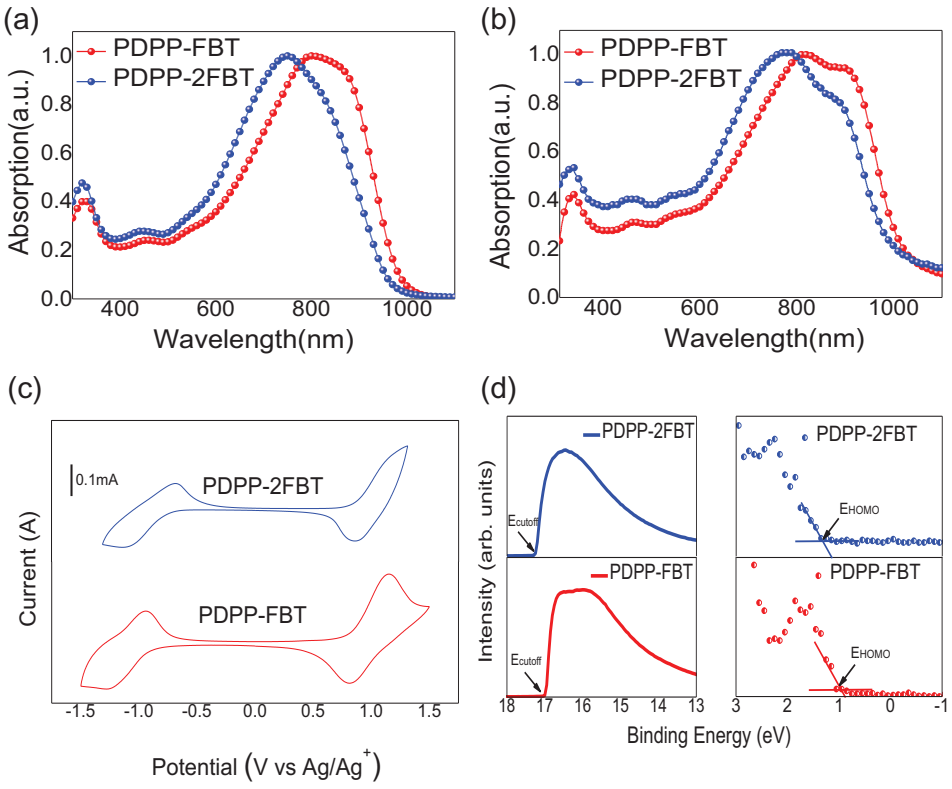

Figure 2.1. UV–vis–NIR absorption spectra of PDPP-FBT and PDPP-2FBT in dilute chloroform (a) solution and (b) thin film on glass plate. (c) Cyclic voltammograms of PDPP-FBT and PDPP-2FBT. (d) UPS spectra of PDPP-FBT and PDPP-2FBT.

ULSAN NATIONAL INSTITUTE OF SCIENCE AND TECHNOLOGY

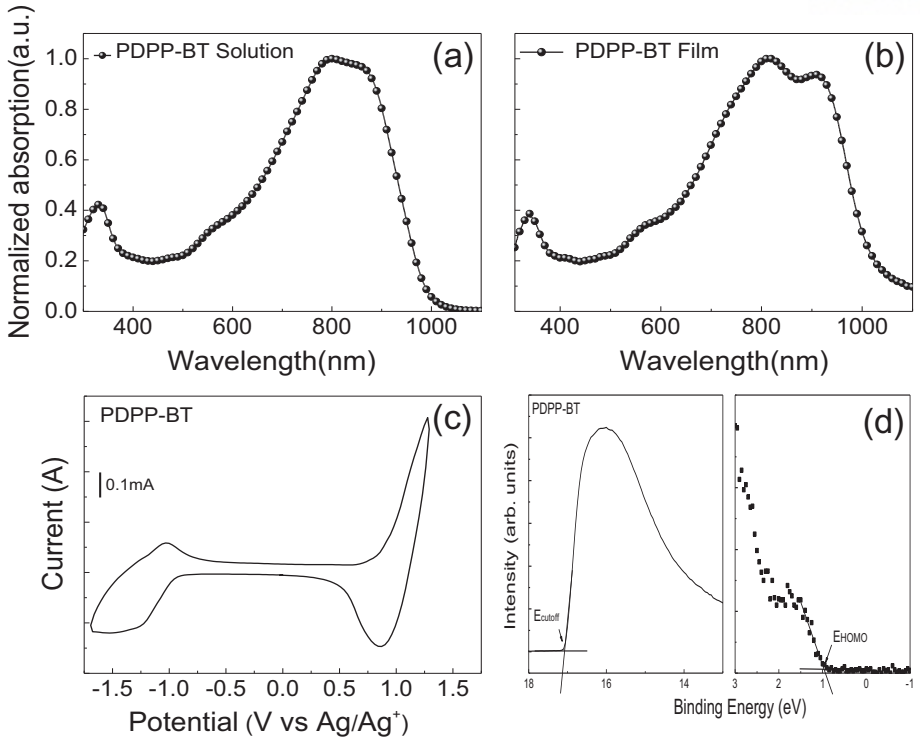

Figure 2.2. UV-vis-NIR absorption spectra of PDPP-BT in dilute chloroform (a) solution and (b) thin film on glass plate. Cyclic voltammograms of (c) PDPP-BT and UPS spectrum of (d) PDPP-BT.

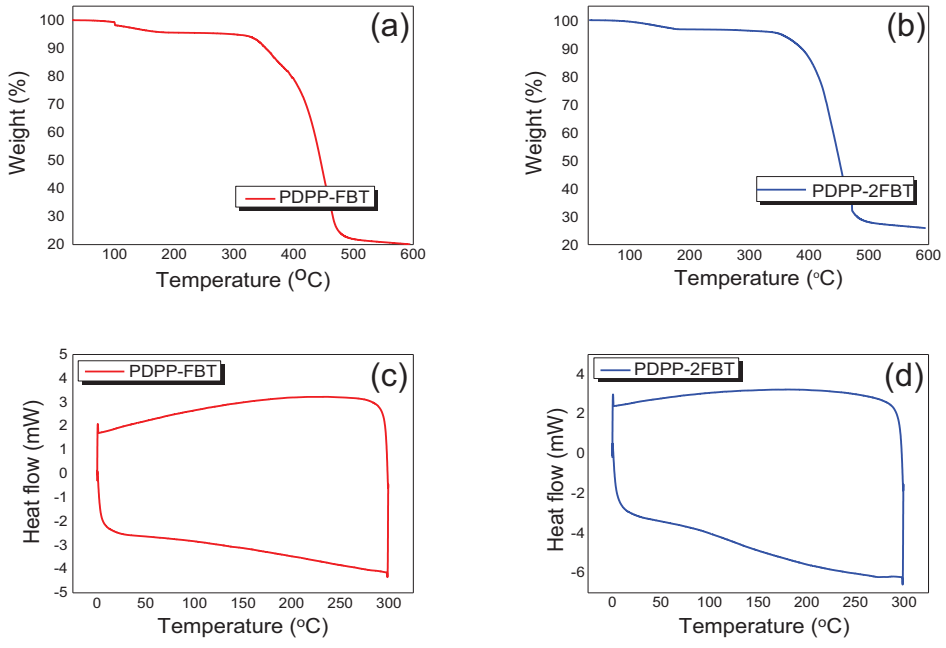

Figure 2.3. TGA traces of (a) PDPP-FBT and (b) PDPP-2FBT, the heating rate is 10 °C min^{-1}. DSC curve of (c) PDPP-FBT and (d) PDPP-FBT at a heating rate of 10 °C min^{-1}.

ULSAN NATIONAL INSTITUTE OF SCIENCE AND TECHNOLOGY

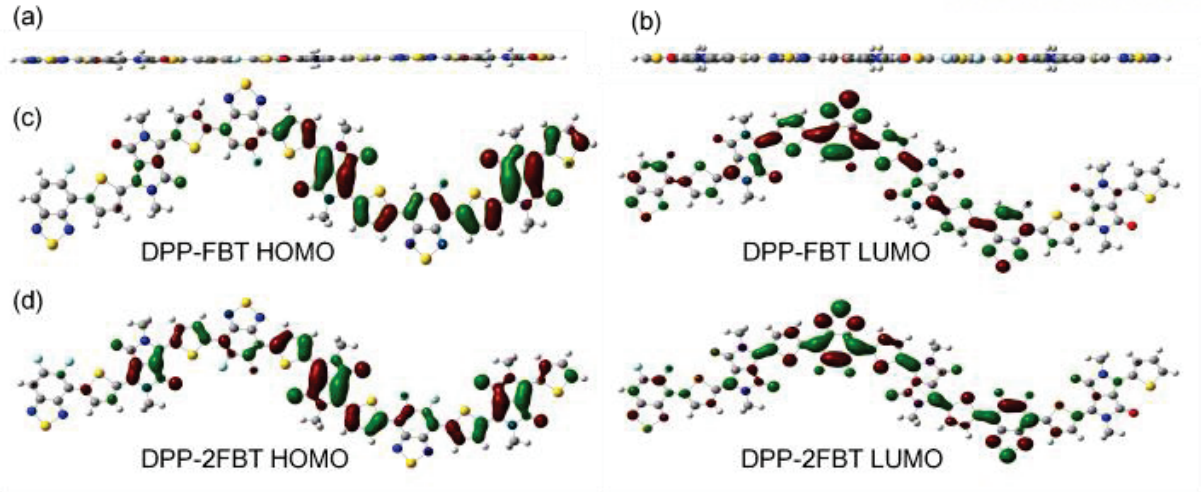

Figure 2.4. Calculated side view of model trimers for (a) DPP-FBT and (b) DPP-2FBT; DFT-optimized geometries and charge-density isosurfaces for (c) DPP-FBT and (d) DPP-2FBT HOMO and LUMO levels.

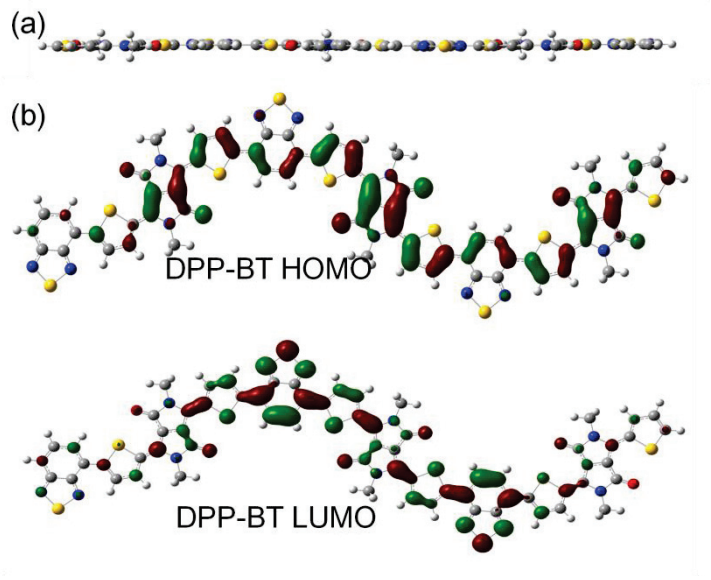

Figure 2.5. Calculated side view of model trimer (a) DPP-BT. DFT-optimized geometries and charge-density isosurfaces for (b) DPP-BT HOMO and LUMO energy levels.

ULSAN NATIONAL INSTITUTE OF SCIENCE AND TECHNOLOGY

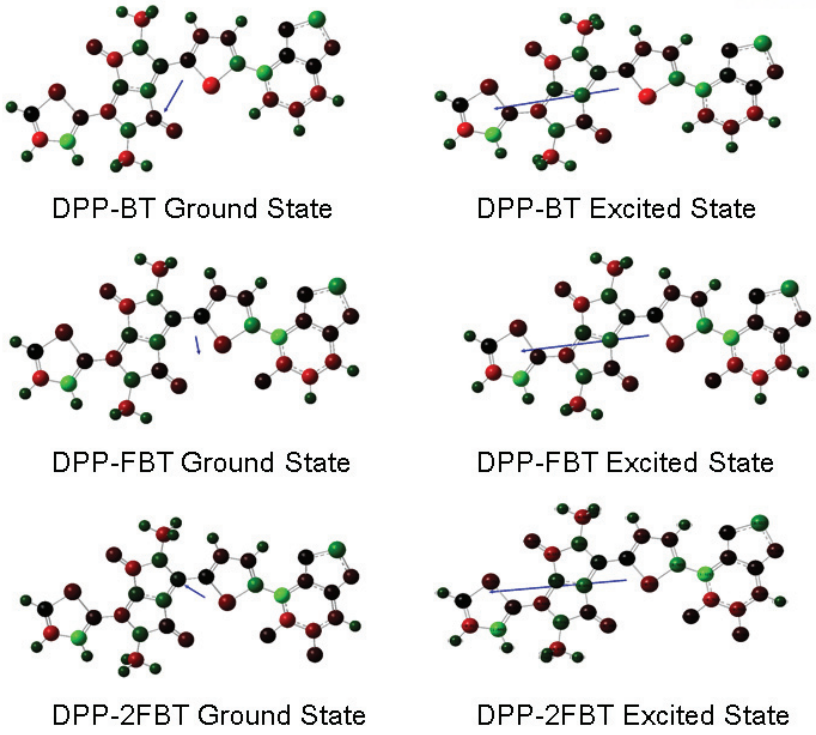

Figure 2.6. Net dipole moments of DPP-BT, DPP-FBT, and DPP-2FBT units in the ground and excited state, respectively (blue line: dipole moment vector).

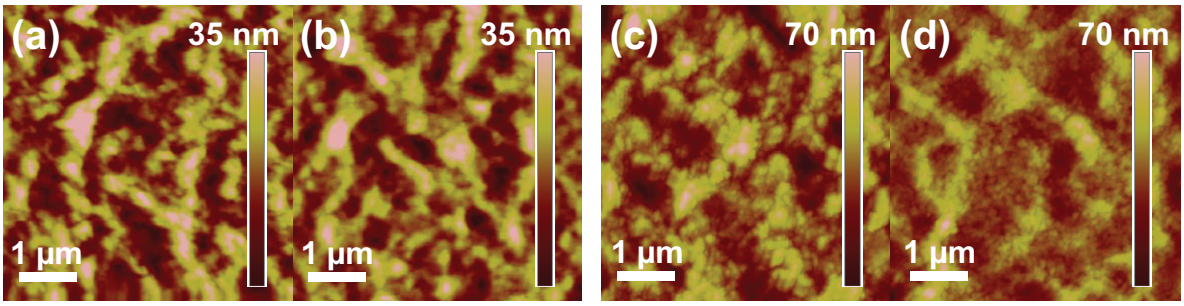

Figure 2.7. AFM height images (5 μm × 5 μm) of drop-cast (a, b) PDPP-FBT and (c, d) PDPP-2FBT films (a, c) before and (b, d) after the thermal annealing at 250 °C, on OTS-modified SiO_2/Si substrates. RMS roughness: (a) = 7.67 nm, (b) = 6.90 nm, (c) = 11.80 nm, (d) = 8.57 nm.

ULSAN NATIONAL INSTITUTE OF SCIENCE AND TECHNOLOGY

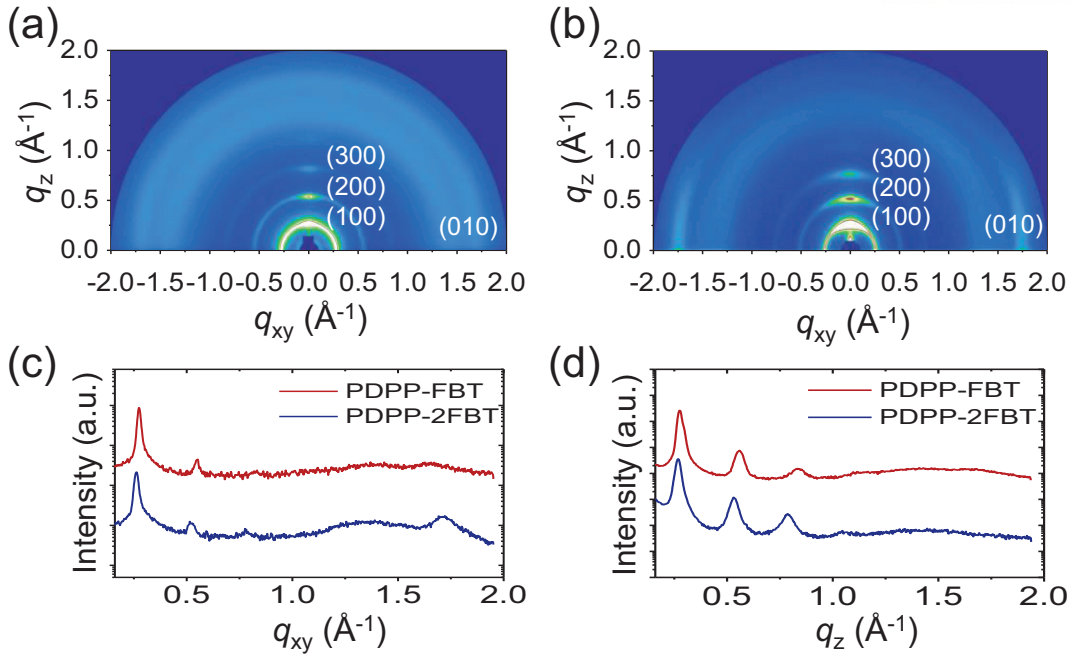

Figure 2.8. 2D-GIXD images of drop-cast films of fluorinated DPP-BT copolymers annealed at 250 °C: (a) PDPP-FBT and (b) PDPP-2FBT. The corresponding GIXD diffractogram profiles: (c) in-plane and (d) out-of-plane GIXD patterns.

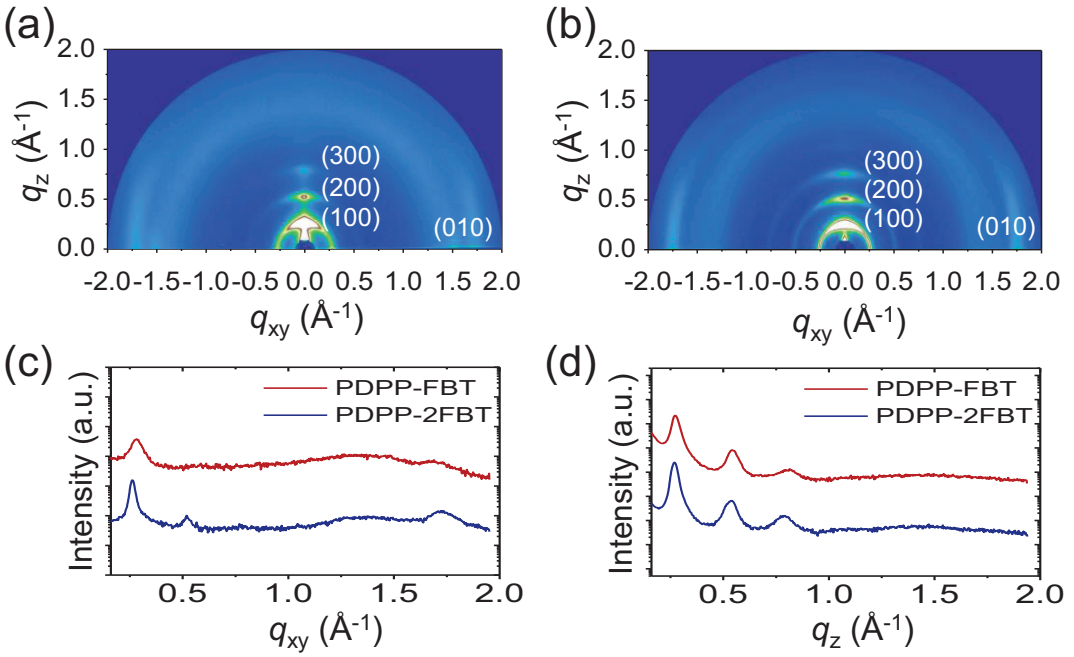

Figure 2.9. 2D-GIXD images of as-cast films of fluorinated DPP-BT copolymers: (a) PDPP-FBT and (b) PDPP-2FBT. The corresponding GIXD diffractogram profiles: (c) in-plane and (d) out-of-plane GIXD patterns.

ULSAN NATIONAL INSTITUTE OF SCIENCE AND TECHNOLOGY

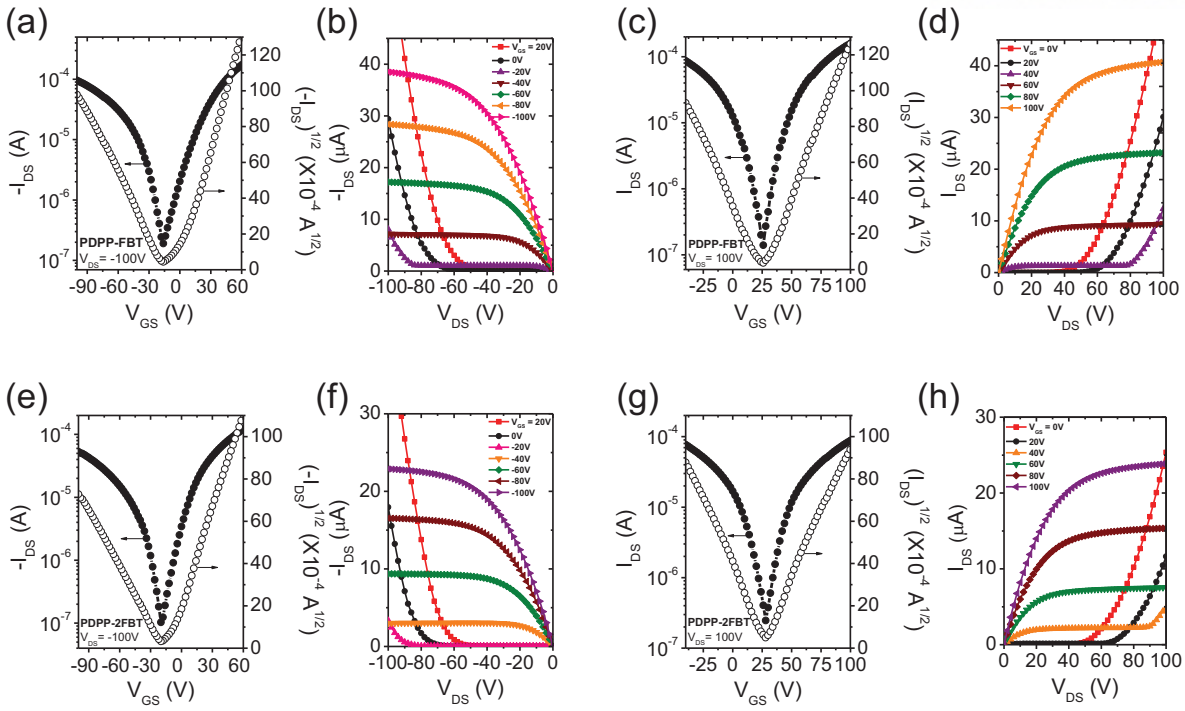

Figure 2.10. Current-voltage (*IV*) characteristics of OFETs based on ambipolar (a–d) PDPP-FBT and (e–h) PDPP-2FBT films of annealed at 250 °C. Transfer characteristics for polymer films in (a, e) *p*-channel operation (V_{DS} = -100 V) and (c, g) *n*-channel operation (V_{DS} = +100 V) mode. (b, d, f, and h) Output characteristics for PDPP-FBT and PDPP-2FBT films.

ULSAN NATIONAL INSTITUTE OF SCIENCE AND TECHNOLOGY

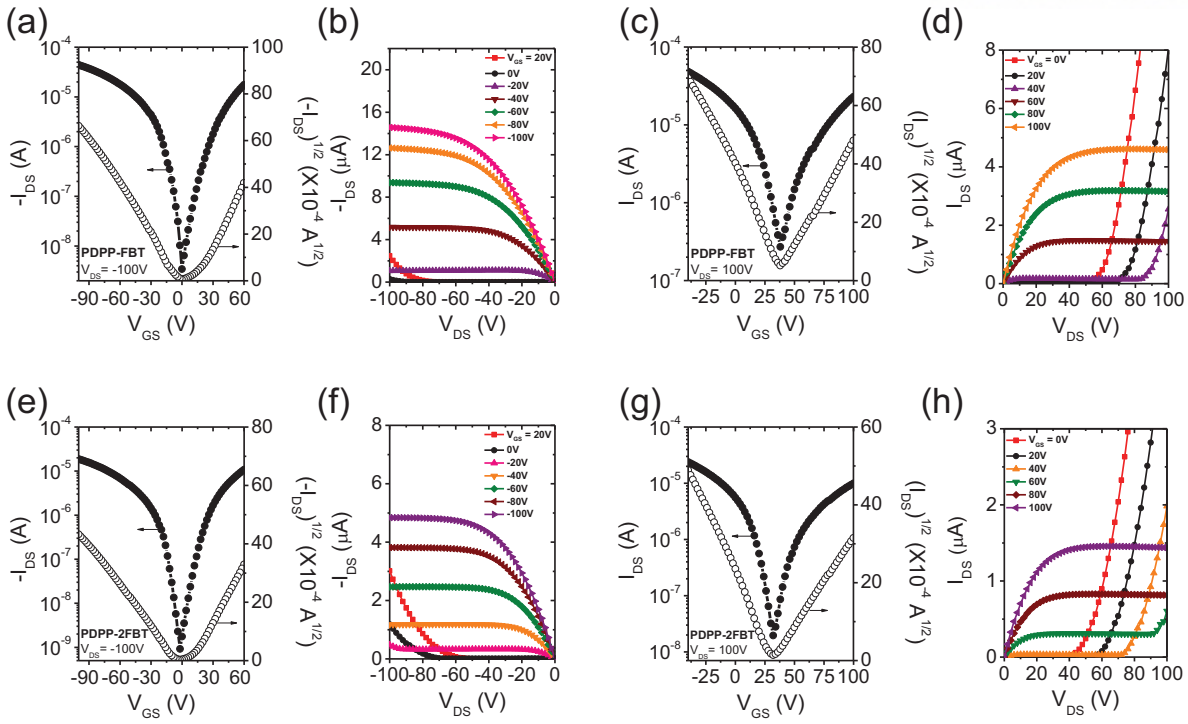

Figure 2.11. Current-voltage (*IV*) characteristics of OFETs based on as-cast film of ambipolar {(a)-(d)} PDPP-FBT and {(e)-(h)} PDPP-2FBT. Transfer characteristics for polymer films in (a), (e) *p*-channel operation (V_{DS} = -100 V) and (c), (g) *n*-channel operation (V_{DS} = +100 V) mode. {(b), (d), (f) and (h)} Output characteristics for PDPP-FBT and PDPP-2FBT films.

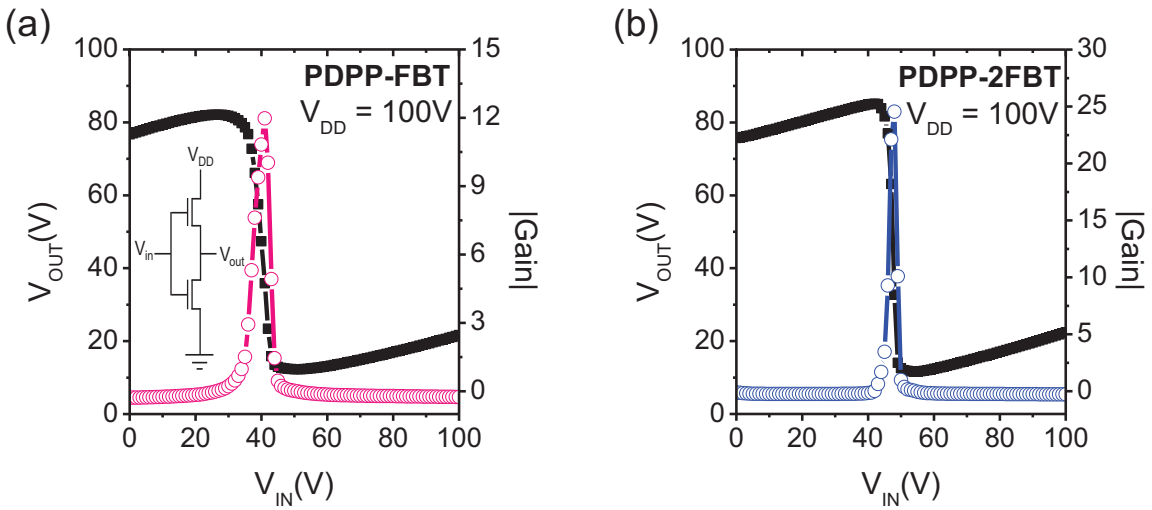

Figure 2.12. Inverter characteristic based on (a) ambipolar PDPP-FBT and (b) PDPP-2FBT OFETs (V_{DD} = 100V).

ULSAN NATIONAL INSTITUTE OF SCIENCE AND TECHNOLOGY

Table 2.1. Optical and electrochemical properties of PDPP-FBT and PDPP-2FBT.

Polymer	UV			CV			UPS
	λ_{max}^{sol} [nm][a]	λ_{max}^{film} [nm][b]	E_g^{opt} [eV][c]	E_{HOMO} [eV][d]	E_{LUMO} [eV][d]	E_g^{CV} [eV][e]	E_{IP}^{UPS} [eV][f]
PDPP-FBT	798	816	1.20	–5.22	–3.49	1.73	5.38
PDPP-2FBT	750	772	1.26	–5.37	–3.53	1.84	5.48

[a]Chloroform solution. [b]Spin-coated from chloroform solution. [c]Determined from the onset of the electronic absorption spectra. [d]Cyclic voltammetry determined with (E_{HOMO} = -($E_{(OX)}^{onset}$ + 4.4 eV) and (E_{LUMO} = -($E_{(Red)}^{onset}$ + 4.4 eV); [e]$E_g^{CV} = E_{LUMO} - E_{HOMO}$; [f]$E_{IP}^{UPS} = h\nu - (E_{cutoff} - E_{HOMO})$, incident photon energy ($h\nu$ = 21.2 eV) for He I.

Table 2.2. Summary of the ground state and excited state dipole moment for DPP-BT, DPP-FBT, and DPP-2FBT monomer (TD-SCF, RB3LYP/6-311G (d) level).

Unit	μ_g (D)[a]	μ_e (D)[b]	$\Delta\ \mu_{ge}$ (D)[c]
TDPP-BT	1.8588	15.5770	14.31069
TDPP-FBT	0.9139	16.4406	16.50265
TDPP-2FBT	1.2191	17.0104	16.04434

[a]μ_g : ground state dipole moment; [b]μ_g : excited state dipole moment; [c]μ_{ge} : overall change calculated by the following equation, $\Delta\ \mu_{ge} = [(\mu_{gx} - \mu_{ex})^2 + (\mu_{gy} - \mu_{ey})^2 + (\mu_{gz} - \mu_{ez})^2]^{1/2}$

Table 2.3. Crystallographic parameters calculated from GIXD profiles.

Preparation condition		Crystallographic parameters		PDPP-FBT	PDPP-2FBT
Drop-casting	As-cast	(*100*)	q (Å^{-1})	0.273	0.269
			d-spacing (Å)	23.0	23.4
			FWHM (Å^{-1})	0.032	0.028
			Coherence length (Å)	177.9	205.0
	Annealing at 250 °C	(*100*)	q (Å^{-1})	0.276	0.268
			d-spacing (Å)	22.8	23.4
			FWHM (Å^{-1})	0.022	0.024
			Coherence length (Å)	259.0	239.9

ULSAN NATIONAL INSTITUTE OF SCIENCE AND TECHNOLOGY

Table 2.4. Summary of OFETs performance data based on PDPP-FBT and PDPP-2FBT films.

Sample[a]		*p*-channel				*n*-channel			
Polymer	Condition	$\mu_{h,max}$[c] [$cm^2 V^{-1} s^{-1}$]	$\mu_{h,avg}$[d] [$cm^2 V^{-1} s^{-1}$]	I_{on}/I_{off}	V_T [V]	$\mu_{e,max}$ [$cm^2 V^{-1} s^{-1}$]	$\mu_{e,avg}$ [$cm^2 V^{-1} s^{-1}$]	I_{on}/I_{off}	V_T [V]
PDPP-FBT	Without annealing	0.087	0.060 (±0.020)[e]	$>10^4$	–6.4	0.061	0.044 (±0.013)	>10	36.6
	Thermal annealing[b]	0.21	0.15 (±0.03)	$>10^2$	–17.5	0.42	0.33 (±0.05)	$>10^3$	30.9
PDPP-2FBT	Without annealing	0.033	0.023 (±0.004)	$>10^4$	–7.1	0.029	0.016 (±0.001)	$>10^2$	32.8
	Thermal annealing	0.10	0.077 (±0.021)	$>10^2$	–19.1	0.30	0.19 (±0.07)	$>10^2$	28.6

[a]The *p*-channel and *n*-channel characteristics of ambipolar OFETs were measured in a nitrogen atmosphere. [b]Thermal annealing was applied at 250 °C. [c]The maximum mobility of the OFET devices (L = 50 μm and W = 1000 μm). [d]The average mobility of the OFET devices (L = 50 μm and W = 1000 μm). [e]The standard deviation was carried out by using more than 10 devices.

Table 2.5. Summary of OFETs performance data based on PDPP-BT films.

Sample[a]		*p*-channel				*n*-channel			
Polymer	Condition	$\mu_{h,max}$[c] [$cm^2 V^{-1} s^{-1}$]	$\mu_{h,avg}$[d] [$cm^2 V^{-1} s^{-1}$]	I_{on}/I_{off}	V_T [V]	$\mu_{e,max}$ [$cm^2 V^{-1} s^{-1}$]	$\mu_{e,avg}$ [$cm^2 V^{-1} s^{-1}$]	I_{on}/I_{off}	V_T [V]
PDPP-BT	Without annealing	0.023	0.019 (±0.003)[e]	$>10^6$	–19.7	0.0047	0.0040 (±0.001)	>10	60.6
	Thermal annealing[b]	0.11	0.080 (±0.023)	$>10^5$	–24.3	0.076	0.057 (±0.021)	$>10^2$	47.3

[a]The *p*-channel and *n*-channel characteristics of ambipolar OFETs were measured in a nitrogen atmosphere. [b]Thermal annealing was applied at 250 °C. [c]The maximum mobility of the OFET devices (L = 50 μm and W = 1000 μm). [d]The average mobility of the OFET devices (L = 50 μm and W = 1000 μm). [e]The standard deviation was carried out by using more than 10 devices.

ULSAN NATIONAL INSTITUTE OF
SCIENCE AND TECHNOLOGY

Chapter 3

Fabrication of Nanostructured Organic Semiconductor Thin Films and Their Chemical Sensor Applications

Abstract

The physical structure of an organic solid is strongly affected by the surface of the underlying substrate. Controlling this interface is an important issue to improve device performance in the organic electronics community. Here we report an approach that utilizes an organic heterointerface to improve the crystallinity and control the morphology of an organic thin film. Pentacene is used as an active layer above, and *m*-bis(triphenylsilyl)benzene is used as the bottom layer. Sequential evaporations of these materials result in extraordinary morphology with far fewer grain boundaries and myriad nanometre-sized pores. These peculiar structures are formed by difference in molecular interactions between the organic layers and the substrate surface. The pentacene film exhibits high mobility up to 6.3 $cm^2 V^{-1} s^{-1}$, and the pore-rich structure improves the sensitivity of organic-transistor-based chemical sensors. Our approach opens a new way for the fabrication of nanostructured semiconducting layers towards high-performance organic electronics.

ULSAN NATIONAL INSTITUTE OF SCIENCE AND TECHNOLOGY

3.1. Introduction

The semiconductor-dielectric interface significantly affects the performance and the reliability of field-effect transistors[1-4]. In organic field-effect transistors (OFETs), especially in a bottom-gate configuration, the surface of the gate dielectric affects the growth and the morphology of the semiconducting layer, which in turn determines how fast charge carriers can move in the channel region[5]. As grain boundaries[6] and dislocations[7] prevent efficient charge transport between adjacent molecules, reducing such disorders in molecular packing has been extensively studied[8-10]. By adding an interfacial layer, such as self-assembled monolayers (SAMs) and polymeric materials, between the semiconductor and the underlying substrate, the interface properties can be controlled effectively for favourable mesoscale/nanoscale ordering of the organic semiconducting layer[5]. It is generally known that the surface of well-ordered SAMs promotes the two-dimensional (2D) growth of vacuum-deposited organic semiconductor thin films and improves the crystallinity; the surface of disordered SAMs is believed to degrade the film quality by reducing the interaction between the surface and admolecules, inducing the three-dimensional (3D) growth rather than the 2D growth[11, 12].

Here we report that a soft and rubbery organic surface that has a suitable interaction energy with organic admolecules can induce the quasi 2D growth with few nuclei and result in high-quality organic thin films with indistinct grain boundaries. Compared with previous high-quality pentacene grains in the rage of few micrometres, our pentacene films exhibited much larger grains and crystalline homogeneity. Furthermore, a high-quality macroporous pentacene thin film was formed by selective adsorption and enhanced lateral diffusion on an organic heterointerface. Sequential evaporations of a small-molecule dielectric and pentacene resulted in high field-effect mobility (μ_{FET}), up to 6.3 $cm^2\ V^{-1}\ s^{-1}$, as well as nanometer-sized pores in the organic layers having vertical orientation with respect to the substrate. We attribute this high μ_{FET} to the large and continuously-connected pentacene grains and to the clean interface between the two organic layers, which were evaporated without breaking vacuum. The macropores were found to enhance the sensitivity of OFET-based chemical sensors because of the enhanced diffusion of analytes into the active channel region.

3.2. Experimental Section

Device fabrication: Heavily doped silicon wafers (n-type, < 0.004 Ω·cm) with thermally grown 300-nm-thick SiO_2 were used as substrates. The SiO_2/Si wafers were cleaned with piranha solution (a mixture of 70 vol% H_2SO_4 and 30 vol% H_2O_2), followed by UV-ozone treatment. The surface of the wafers was modified with *n*-octadecyltrimethoxysilane (OTS) self-assembled monolayer.[13] The OTS solution (3 mM in trichloroethylene) was spin-coated at 3000 rpm for 30 s onto the wafers, and then the samples were kept overnight in a vacuum desiccator with a few drops of NH_4OH. The wafers were washed with toluene, acetone and isopropyl alcohol, and dried under nitrogen gas. The contact angle of

ULSAN NATIONAL INSTITUTE OF SCIENCE AND TECHNOLOGY

deionized water on the OTS-treated SiO_2 was typically above 110°.

To fabricate the OFETs, TSB3 (15 nm) and pentacene (45 nm) layers were sequentially deposited onto the OTS-treated SiO_2/Si substrates in a thermal evaporator without breaking vacuum. The base pressure was below 5.0×10^{-6} torr, and the deposition rate was maintained at 0.1-0.2 Å s^{-1}. For pentacene OFETs without TSB3, only a pentacene layer (45 nm) was thermally evaporated. During the evaporation, the samples were heated at 60 °C. Gold source/drain electrodes (40 nm) were thermally evaporated through a shadow mask onto the pentacene layer. The source/drain patterns had a channel length (L) of 50 μm and a channel width (W) of 1000 μm (W/L = 20).

To measure the capacitance of the gate dielectric, TSB3 (15 nm) and gold electrode patterns (40 nm) were deposited sequentially onto OTS-treated SiO_2/Si with gold electrode patterns in a single vacuum process.

Electrical Measurement: The current-voltage characteristics of the OFETs were measured inside a glove box filled with nitrogen gas by using a Keithley 4200-SCS semiconductor parametric analyzer. The field-effect mobility (μ_{FET}) and the threshold voltage (V_{TH}) were estimated in the saturation regime (V_{DS} = -100 V) with the following equation:[14]

$$I_D = \frac{W}{2L} \mu_{FET} C_g \left(V_{GS} - V_{TH}\right)^2, \quad (1)$$

where I_D is the drain current, C_g is the capacitance of the gate dielectric and V_{GS} is the gate-source voltage.

In the sensor measurements, methanol vapour was produced by flowing nitrogen gas into a flask filled with liquid methanol. Vapourized methanol then flowed to the sensor device through a 3-mm-wide tube. The end of the tube was installed 5 cm above the surface of the device. While the flow of methanol was on, the gas flow was maintained at 4 sccm.

The capacitance of the gate dielectric was measured with an Agilent 4284A. Both OTS-SiO_2 (300 nm) and TSB3 (15 nm)-OTS-SiO_2 (300 nm) samples had almost identical capacitance of 11 nF cm^{-2}.

Morphology Characterization: The surface morphologies were characterized with AFM (Digital Instruments Multimode) and SEM (Hitachi S-4200).

2D GIXD measurements were performed at the 3C and 9A beamlines of the Pohang Accelerator Laboratory.

Cross-sectional HRTEM images were obtained by using a field emission electron microscope (JEOL, JEM-2100F). In the preparation of HRTEM specimens, aluminum (250 nm) and platinum (1.3 μm) layers were sequentially deposited on the samples to protect the organic layers against high-energy gallium ions (acceleration voltage of 30 kV) during focused-ion-beam milling process (FEI, Helios).

Material Analysis: The optical and thermal behaviors of TSB3 were measured by using a UV-Vis spectrophotometer (Varian, CARY-5000) and a differential scanning calorimetry (Perkin-Elmer DSC7), respectively.

ULSAN NATIONAL INSTITUTE OF SCIENCE AND TECHNOLOGY

Cyclic voltammetry was performed by using a PowerLab/AD instrument model system. A tetrabutylammonium hexafluorophosphate (Bu_4NPF_6) solution in acetonitrile (0.1 M) was used as the electrolyte solution. Three kinds of electrodes were used in the measurements: Ag/AgCl reference electrode, glassy carbon working electrode, and platinum counter electrode. The potential of the Ag/AgCl reference electrode was internally calibrated by using the ferrocene/ferrocenium redox couple (Fc/Fc+). The energy levels of organic semiconductors were estimated with the equations below:

$$E_{HOMO} = -\left(\left(E_{onset,ox} - E_{1/2(Ferrocene)}\right) + 4.8\right)[eV], \quad (2)$$

$$E_{LUMO} = -\left(\left(E_{onset,red} - E_{1/2(Ferrocene)}\right) + 4.8\right)[eV], \quad (3)$$

DFT calculation: DFT calculations were performed by using the Gaussian 03 package with the Becke, 3-parameter, Lee-Yang-Parr (B3LYP) function and the 6-31G* basis set after optimizing the geometry of TSB3.

Molecular dynamics simulation: To interpret the bonding and non-bonding interactions in the atomic systems of interest, the COMPASS (Condensed-phase Optimized Molecular Potentials for Atomistic Simulation Studies) force field was employed. The equation for the total interaction energy, V (R), which contains nearly 30 potential energy parameters, has the generic form:

$$V(R) = \left(\sum v_{stretching} + \sum v_{bending} + \sum v_{tortion} + \sum v_{deformation}\right)_b + \left(\sum v_{Coulomb} + \sum v_{van\ der\ Waals} + \sum v_{Morse-dispersion}\right)_{nb}, \quad (4)$$

The first four terms are the energies of bond stretching, angle bending, torsion and deformation, respectively, which mostly are fitted into anharmonic forms. The next three terms are the long-range electrostatic (i.e., Coulombic), van der Waals (i.e., 9-6 Lennard-Jones) and dispersion (i.e., Morse type) interaction energies, respectively. The final term is present for the simulation of semi-ionic systems. The total interaction energy, V(R), is integrated with respect to time following the Verlet algorithm to provide pair-wise momenta between atoms, and the time interval was set to be 1 fs. We performed all-atom molecular dynamics simulations with the isometric and isothermal ensemble (i.e. constant NVT, where N is the number of molecules, V is the volume and T is the temperature) at 60 °C. All systems with interfaces were constructed by adding each constituent system and allowing it to undergo energy minimization with a relaxation period for 10 ps. After each interfacial system was constructed, it was relaxed with the same ensemble for 20 to 30 ps and run for 100 ps to calculate the binding energies and obtain other results. Molecular dynamics (MD) simulations were performed by Prof. Sang Kyu Kwak, UNIST.

3.3. Results and Discussion

ULSAN NATIONAL INSTITUTE OF SCIENCE AND TECHNOLOGY

3.3.1. Material properties and device fabrication

For the insulating small-molecule organic layer, we employed *m*-bis(triphenylsilyl)benzene (TSB3), as shown in **Figure 3.1a**. This organosilicon compound has a high energy gap of 3.6 eV in a thin film (**Figure. 3.2a**), due to the electronically isolated phenyl rings. The highest occupied molecular orbital (HOMO) level of TSB3 was estimated to be -7.1 eV by density functional theory (DFT) calculations, which is far lower than that of pentacene (-5.0 eV) (**Figure. 3.2b**). The HOMO level was also experimentally confirmed by using cyclic voltammetry (**Figure. 3.2c**). As a result, unfavourable charge transfer between TSB3 and pentacene is minimized during OFET operations. The glass transition temperature (T_g) and melting temperature (T_m) of TSB3 were estimated to be 33 °C and 238 °C, respectively (**Figure. 3.2d**). For the fabrication of OFETs, TSB3 and pentacene molecules were sequentially deposited in a thermal evaporator (< 10^{-6} torr) while *n*-octadecyltrimethoxysilane (OTS)-treated SiO_2 substrates were heated to 60 °C, which is higher than the T_g of TSB3. Detailed fabrication process is described in the Methods section. The structure of the OFET is schematically illustrated in Figure 1a. As control devices, another set of pentacene OFETs was also fabricated on OTS-treated SiO_2 excluding the evaporation of TSB3.

3.3.2 Macroporous pentacene film with indistinct grain boundaries

We first examined the morphological and the crystalline characteristics of the organic thin films. As shown in the atomic force microscopy (AFM) images of **Figure 3.1b**, the presence of the TSB3 layer drastically alters the morphology of pentacene. In contrast to the small pentacene grains obtained in the absence of TSB3, the pentacene layer with TSB3 is continuously connected with indistinct grain boundaries. Dendritic or faceted grains have been commonly observed from pentacene thin films evaporated on a variety of substrates such as polymers, SAMs and inorganic layers[9]. The extraordinary pentacene morphology on TSB3 indicates that the TSB3 layer significantly affects the growth of pentacene film. The pores in the pentacene film on TSB3 range in size from 50 to 150 nm, and their depth is found to be similar to the thickness of the organic layers (**Figure 3.1b**). A cross-sectional image of the pores was obtained with high-resolution transmission electron microscopy (HRTEM) in **Figure 3.1c**. The pores are connected to the OTS surface, which confirms that the pore depth corresponds to the combined thickness of the organic layers. It is noteworthy that no grain boundary defects are visible in the cross-sectional HRTEM image within the pentacene layer on TSB3, which is in agreement with the AFM image in **Figure 3.1b** (detailed cross-sectional HRTEM analysis can be found in **Figure. 3.3**).

The electrical characteristics of the pentacene OFETs with and without TSB3 were measured in the saturation regime inside a nitrogen-filled glovebox. As shown in **Figure 3.4a**, the pentacene OFETs with TSB3 exhibited higher output currents compared with the pentacene OFETs without TSB3 (**Figure. 3.5** for current-voltage curves in logarithmic scale and drain current vs. drain-source voltage curves). The pentacene OFETs with TSB3 had an average μ_{FET} of 5.5 (±0.7) $cm^2 V^{-1} s^{-1}$, whereas the pentacene OFETs without TSB3 showed an average μ_{FET} of only 1.5 (±0.2) $cm^2 V^{-1} s^{-1}$. The I_{ON}/I_{OFF} ratios of both

ULSAN NATIONAL INSTITUTE OF SCIENCE AND TECHNOLOGY

sets of OFETs were more than 10^6, and the threshold voltage values were -37.5 (±0.8) V (with TSB3) and -33.5 (±1.1) V (without TSB3).

A thorough investigation of the pentacene/TSB3 interface is needed to elucidate the remarkably high μ_{FET} of the pentacene OFETs with TSB3, because charge transport in OFETs occurs in the channel region in the vicinity of the gate dielectric[14]. The morphology of TSB3 is, however, unstable due to its low T_g, so the growth dynamics of pentacene thin films on TSB3 is difficult to study directly. We observed huge clusters of TSB3 after deposition of a 15-nm-thick TSB3 layer on OTS-treated SiO_2 (**Figure 3.4b**). Such clusters were also found in pentacene (5 and 10 nm) / TSB3 (15 nm) layers; however, such clustering was not observed when a thick layer of pentacene (more than 20 nm) was deposited onto the TSB3 film (**Figure 3.4c-f**). We speculate that the TSB3 layer becomes stable in the presence of a thick upper pentacene layer, which suppresses the agglomeration of the bottom TSB3. We performed 2D grazing incidence X-ray diffraction (GIXD) measurements on 5-nm-thick pentacene on TSB3. The 2D GIXD pattern in **Figure 3.4g** indicates that the first few layers of pentacene on TSB3 have predominant thin-film phase. It is known that the coexistence of different pentacene polymorphs can contribute to an increase in the charge-transfer resistance due to the inter-grain and inter-domain structural mismatches between different crystalline phases[10, 15, 16]. We attribute the high μ_{FET} of pentacene OFETs with TSB3 to the structural homogeneity of the first few layers of pentacene, which contain far fewer grain boundaries, as well as to the clean semiconductor (pentacene) / dielectric (TSB3 on OTS-treated SiO_2) interface, produced by the sequential evaporation process without breaking vacuum, as illustrated schematically in **Figure 3.4h**.

3.3.3 Application of macropores to OFET-based chemical sensor

In addition to the typical switching operation in logic circuits, OFETs can be used for sensor devices[17-20]. In general, the output current of OFET-based sensors and detectors is scaled with the amount of target species diffused into the channel region[21]. In OFET-based chemical sensors, the device structure often limits their performance by blocking the efficient diffusion of analytes into the active channel region. Thus, organic semiconducting films with porous structure that facilitate charge transport may be ideal for OFET-based chemical sensors. The vertical macropores in the pentacene/TSB3 layers can improve the sensitivity of OFET-based chemical sensors by enhancing the diffusion of analytes into the channel region. In contrast to previous OFET-based sensors, in which the analytes diffuse into the channel through grain boundaries[21], the macropores provide more efficient and direct pathways, which eventually leads to fast response and high sensitivity to the changes in analyte concentration (**Figure 3.6a**). We monitored the changes in the output current of pentacene OFETs with and without TSB3 while the flow of vapourized methanol was turned on and off sequentially. In order to confirm that methanol does not swell nor dissolve TSB3, a TSB3 layer was exposed to vapourized methanol, and its morphology was examined by AFM. The exposure of the TSB3 layer to methanol did not affect its physical structure. It is known that methanol molecules typically

ULSAN NATIONAL INSTITUTE OF SCIENCE AND TECHNOLOGY

decrease the channel charge density of p-channel devices due to its electron-donating characteristics[22]. As shown in **Figure 3.6b**, the OFET-based sensor with TSB3 exhibited a significant decrease in the output current when the device was exposed to methanol vapour. In addition, the response and recovery occurred within a few seconds, which demonstrates a remarkably fast and stable performance compared with previous OFET-based sensors[23, 24] as well as for other chemical sensors based on conducting polymers[25], carbon nanotubes[26] or inorganic semiconductors[27]. On the other hand, the OFET-based sensors without TSB3 showed much lower sensitivity under the same condition. These results indicate that the macroporous structure induced by TSB3 is highly beneficial to improving the performance of OFET-based sensor devices.

3.3.4 Discussions

The flat and smooth morphology of pentacene on TSB3 is evidence for the Frank-van der Merwe growth of the pentacene admolecules[3]. In the Frank–van der Merwe growth, admolecules attach preferentially to the substrate surface rather than to the pre-deposited area, which leads to the formation of atomically smooth and fully covered layers[28]. **Figure 3.7** shows 2D GIXD patterns of pentacene thin films with and without TSB3. The (00*l*) reflections in the q_z direction (out-of-plane) indicate that pentacene molecules have stand-up orientation on TSB3. The two intense in-plane reflections, appearing vertically at a given q_{xy}, can be indexed to $\{1, \pm1\}$ and $\{0, 2\}$, respectively; each reflection index represents two distinct crystalline polymorphs of pentacene thin film, which are referred to as the pseudo-orthorhombic "thin-film" phase and the triclinic "bulk" phase[29]. The multiple reflection spots in these vertical "Bragg-rods" suggest that our pentacene films consist of ordered multi-stacked layers in both vertical and lateral directions[30]. Interestingly, the pentacene film on TSB3 consists predominantly of the thin-film phase, whereas both thin-film and bulk phases are present in the pentacene film without TSB3. Note that the circular pattern at $q_r \approx 1.37$ Å^{-1} in **Figure 3.7a** is due to the underneath TSB3 layer, which is not preferentially oriented on the substrate (**Figure. 3.8**).

We devise the mechanism in **Figure 3.9** for the growth of pentacene on TSB3 to explain the indistinct grain boundaries and the formation of the pores. Molecular dynamics (MD) simulations were performed to test our model[31, 32]. Firstly, the direct contact between TSB3 and OTS was studied in an attempt to explain the dewetting of TSB3. The interaction energy between TSB3 molecules is more negative, i.e., more attractive, than the interaction energy between TSB3 and OTS (**Figure. 3.10**). This result indicates that agglomeration of TSB3 occurs instead of covering the substrate. The atomically smooth OTS layer with low surface energy may also expedite the dewetting of TSB3, which is already in a rubbery state because the substrate temperature is higher than its T_g. Once pentacene is evaporated, it starts to be adsorbed onto the rubbery TSB3 film rather than onto the dewetted OTS area. We calculated the TSB3-pentacene and OTS-pentacene interaction energies with MD simulations. Monolayer, bilayer and trilayer of pentacene were constructed on TSB3 and OTS (**Figure. 3.11**); the relatively unfavourable interaction (i.e., larger positive binding energy) is estimated between pentacene and OTS. This result

ULSAN NATIONAL INSTITUTE OF SCIENCE AND TECHNOLOGY

indicates that the deposition of evaporated pentacene molecules occur preferentially on the TSB3 surface rather than OTS. When the pentacene molecules encounter the dewetted OTS surface, they are captured by the pentacene/TSB3 layers through the van der Waals force. To confirm this selective growth, we simulated the movement of the pentacene molecules by placing them at the boundary between the TSB3 and OTS layers, as shown in **Figure 3.12**. After 50 ps, the pentacene molecules, which straddled at the boundary, have diffused towards the TSB3 layer. Previously, Bao and coworkers estimated the mean travelling distance of pentacene molecules on OTS surfaces by using the capture zone model: 0.67 and 1.12 μm for crystalline and amorphous OTS, respectively[33]. Since in our study the size of the pores in the pentacene film with TSB3 range from 50 to 150 nm, the pentacene molecules deposited on dewetted OTS have enough time to escape to the pentacene/TSB3 layer. Thus, the large number of macropores in the pentacene thin film on TSB3 is attributed to the dewetting of TSB3 and the preferential growth of pentacene via diffusion onto TSB3 rather than OTS.

The high μ_{FET} of the pentacene OFETs with TSB3 indicates that the macropores in the pentacene layer do not severely affect the charge transport, as depicted in Figure 2h. During the growth of pentacene, the nucleation density (N) in the first seeding layer is known to be related to the ratio between the diffusion constant (D) and the deposition rate (F) by the following equation: $N \approx F/D$[34]. In our experiment, N is mainly dependent on the D of pentacene adsorbed on the surface because F remains constant by controlling the evaporation condition. The D value seems to be larger on the TSB3 surface than on the OTS, as inferred from the enlarged crystal domains with indistinct grain boundaries on the TSB3 layer. The soft and rubbery characteristics of the TSB3 surface facilitate the lateral diffusion of pentacene molecules[33, 35]. Similarly, previous studies revealed higher D values for pentacene admolecules on disordered SAMs, which have mobile alkyl chains and soft surface, than on ordered SAMs[11, 12]. This enhanced surface diffusion contributes to the self ordering of pentacene with far fewer grain boundaries in the first seeding layer. Kim et al. reported that the surface viscoelasticity of polymer gate dielectrics affects the performance of pentacene transistors; pentacene thin films deposited at substrate temperatures higher than the T_g of the polymer dielectrics had inferior pentacene crystallinity and morphology[36]. In the case of these polymer dielectrics, however, the attractive interactions with pentacene molecules are much stronger than our soft small-molecule dielectric TSB3 (see the MD simulation results in **Figure. 3.13**). Therefore, the diffusivity of pentacene admolecules is reduced on the polymers, which hinders the growth of high-quality pentacene thin film.

3.4. Conclusion

In summary, we have investigated the effects of the organic heterointerface between rubbery small-molecule dielectric and pentacene on the performance of OFETs and chemical sensors. TSB3, an organosilicon insulating compound with low T_g, significantly changed the morphology of pentacene

ULSAN NATIONAL INSTITUTE OF SCIENCE AND TECHNOLOGY

thin layer and affected the device performance. Continuously interconnected pentacene grains with far fewer grain boundaries were formed on TSB3, leading to remarkably high μ_{FET} up to 6.3 $cm^2 V^{-1} s^{-1}$. In addition, a large number of vertical macropores observed in the organic layers significantly improved the sensitivity of chemical sensors. Our finding demonstrates that organic small-molecule heterointerfaces, enabling a sophisticated control of the growth and morphology in organic thin films, can be utilized to improve the performance of organic electronic devices and to expand their applications.

ULSAN NATIONAL INSTITUTE OF SCIENCE AND TECHNOLOGY

3.5. References

[1] Podzorov V.; Menard E.; Borissov A.; Kiryukhin V.; Rogers J. A., Gershenson M. E., *Phys. Rev. Lett.* **2004**, *93*, 086602-086605.
[2] Chua L. L.; Zaumseil J.; Chang J. F.; Ou E. C. W.; Ho P. K. H.; Sirringhaus H., Friend R. H., *Nature* **2005**, *434*, 194-199.
[3] Heringdorf F. J. M. Z.; Reuter M. C., Tromp R. M., *Nature* **2001**, *412*, 517-520.
[4] Klauk H.; Zschieschang U.; Pflaum J., Halik M., *Nature* **2007**, *445*, 745-748.
[5] Lee W. H.; Cho J. H., Cho K., *J. Mater. Chem.* **2010**, *20*, 2549-2561.
[6] Rivnay J.; Jimison L. H.; Northrup J. E.; Toney M. F.; Noriega R.; Lu S. F.; Marks T. J.; Facchetti A., Salleo A., *Nat. Mater.* **2009**, *8*, 952-958.
[7] Nickel B.; Barabash R.; Ruiz R.; Koch N.; Kahn A.; Feldman L. C.; Haglund R. F., Scoles G., *Phys. Rev. B* **2004**, *70*, 125401-125407.
[8] Minemawari H.; Yamada T.; Matsui H.; Tsutsumi J.; Haas S.; Chiba R.; Kumai R., Hasegawa T., *Nature* **2011**, *475*, 364-367.
[9] Ruiz R.; Choudhary D.; Nickel B.; Toccoli T.; Chang K. C.; Mayer A. C.; Clancy P.; Blakely J. M.; Headrick R. L.; Iannotta S., Malliaras G. G., *Chem. Mater.* **2004**, *16*, 4497-4508.
[10] Zhang J.; Rabe J. P., Koch N., *Adv. Mater.* **2008**, *20*, 3254-3257.
[11] Virkar A.; Mannsfeld S.; Oh J. H.; Toney M. F.; Tan Y. H.; Liu G. Y.; Scott J. C.; Miller R., Bao Z., *Adv. Funct. Mater.* **2009**, *19*, 1962-1970.
[12] Lee H. S.; Kim D. H.; Cho J. H.; Hwang M.; Jang Y., Cho K., *J. Am. Chem. Soc.* **2008**, *130*, 10556-10564.
[13] Ito Y.; Virkar A. A.; Mannsfeld S.; Oh J. H.; Toney M.; Locklin J., Bao Z. A., *J. Am. Chem. Soc.* **2009**, *131*, 9396-9404.
[14] Horowitz G., *Adv. Mater.* **1998**, *10*, 365-377.
[15] Street R. A.; Knipp D., Volkel A. R., *Appl. Phys. Lett.* **2002**, *80*, 1658-1660.
[16] Kang J. H.; da Silva D.; Bredas J. L., Zhu X. Y., *Appl Phys Lett* **2005**, *86*, 152115-152117.
[17] Torsi L.; Farinola G. M.; Marinelli F.; Tanese M. C.; Omar O. H.; Valli L.; Babudri F.; Palmisano F.; Zambonin P. G., Naso F., *Nat. Mater.* **2008**, *7*, 412-417.
[18] Mannsfeld S. C. B.; Tee B. C. K.; Stoltenberg R. M.; Chen C. V. H. H.; Barman S.; Muir B. V. O.; Sokolov A. N.; Reese C., Bao Z. N., *Nat. Mater.* **2010**, *9*, 859-864.
[19] Gelinck G. H.; Huitema H. E. A.; Van Veenendaal E.; Cantatore E.; Schrijnemakers L.; Van der Putten J. B. P. H.; Geuns T. C. T.; Beenhakkers M.; Giesbers J. B.; Huisman B. H.; Meijer E. J.; Benito E. M.; Touwslager F. J.; Marsman A. W.; Van Rens B. J. E., De Leeuw D. M., *Nat. Mater.* **2004**, *3*, 106-110.
[20] Sekitani T.; Yokota T.; Zschieschang U.; Klauk H.; Bauer S.; Takeuchi K.; Takamiya M.; Sakurai T., Someya T., *Science* **2009**, *326*, 1516-1519.
[21] Someya T.; Dodabalapur A.; Huang J.; See K. C., Katz H. E., *Adv. Mater.* **2010**, *22*, 3799-3811.
[22] Thompson T. L., Yates J. T., *J. Phys. Chem. B* **2005**, *109*, 18230-18236.
[23] Zhu Z. T.; Mason J. T.; Dieckmann R., Malliaras G. G., *Appl. Phys. Lett.* **2002**, *81*, 4643-4645.
[24] Li L. Q.; Gao P.; Baumgarten M.; Mullen K.; Lu N.; Fuchs H., Chi L. F., *Adv. Mater.* **2013**, *25*, 3419-3425.
[25] Geng L.; Zhao Y. Q.; Huang X. L.; Wang S. R.; Zhang S. M., Wu S. H., *Sens. Actuators B* **2007**, *120*, 568-572.
[26] Snow E. S.; Perkins F. K.; Houser E. J.; Badescu S. C., Reinecke T. L., *Science* **2005**, *307*, 1942-1945.
[27] Jia Y.; He L. F.; Guo Z.; Chen X.; Meng F. L.; Luo T.; Li M. Q., Liu J. H., *J. Phys. Chem. C* **2009**, *113*, 9581-9587.
[28] Cheng H. L.; Mai Y. S.; Chou W. Y.; Chang L. R., Liang X. W., *Adv. Funct. Mater.* **2007**, *17*, 3639-3649.
[29] Drummy L. F., Martin D. C., *Adv. Mater.* **2005**, *17*, 903-907.
[30] Yang H. C.; Shin T. J.; Ling M. M.; Cho K.; Ryu C. Y., Bao Z. N., *J. Am. Chem. Soc.* **2005**, *127*, 11542-11543.

ULSAN NATIONAL INSTITUTE OF SCIENCE AND TECHNOLOGY

[31] Allen M. P., Tildesley D. J., *Computer simulation of liquids*, Oxford University Press, New York 1987.
[32] Frenkel D., Smith B., *Understanding molecular simulation: from algorithms to applications*, Academic Press, San Diego 2002.
[33] Virkar A. A.; Mannsfeld S. C. B., Bao Z. N., *J. Mater. Chem.* **2010**, *20*, 2664-2671.
[34] Ruiz R.; Nickel B.; Koch N.; Feldman L. C.; Haglund R. F.; Kahn A.; Family F., Scoles G., *Phys. Rev. Lett.* **2003**, *91*, 136102-136105.
[35] Kim D. H.; Lee H. S.; Yang H. C.; Yang L., Cho K., *Adv. Funct. Mater.* **2008**, *18*, 1363-1370.
[36] Kim C.; Facchetti A., Marks T. J., *Science* **2007**, *318*, 76-80.

Reprinted in part with permission from B. Kang, M. Jang and Y. Chung *et al*., *Nat. Commun.* **2014, *5*, 4752. Copyright © 2014, Rights Managed by Nature Publishing Group.

ULSAN NATIONAL INSTITUTE OF SCIENCE AND TECHNOLOGY

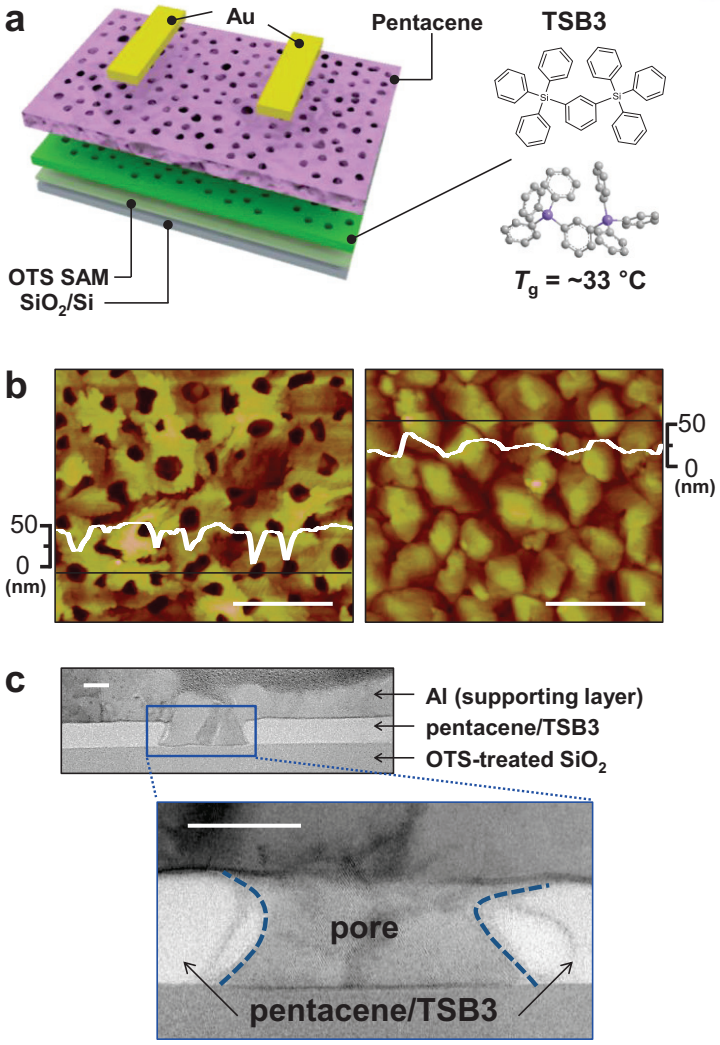

Figure 3.1. Device structure and Morphology of organic layers: a) Device schematic and the molecular structure of TSB3. b) AFM height images of (*left*) pentacene / TSB3 and (*right*) pentacene on OTS-treated SiO_2. A large number of pores are present in the pentacene-TSB3 film. The scale bars are 1 μm. c) Cross-sectional HRTEM image of pentacene (45 nm) / TSB3 (15 nm) on OTS-treated SiO_2. The depth of the pore, also clearly observed in the AFM image of Figure 3.1b, is the same as the thickness of the pentacene/TSB3 layers. The scale bars are 50 nm.

ULSAN NATIONAL INSTITUTE OF SCIENCE AND TECHNOLOGY

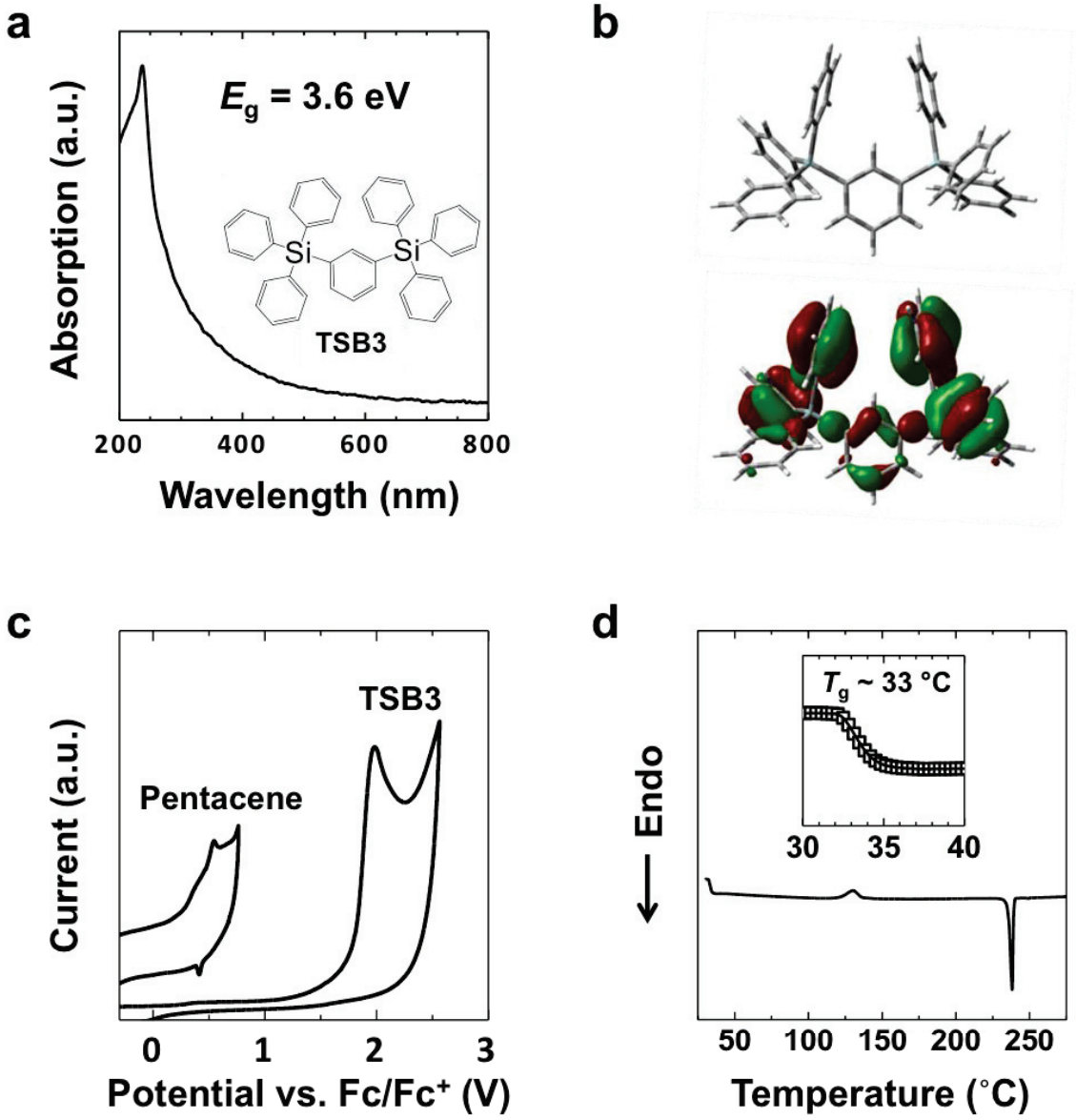

Figure 3.2. Analysis on TSB3 molecules: a) Ultraviolet–visible spectrum of TSB3 thin film. The band gap of a TSB3 thin film (15 nm) was measured to be 3.6 eV. b) (Upper) Optimized geometry of a TSB3 molecule in vacuum and (lower) its charge-density isosurfaces calculated by density functional theory (DFT) calculations. c) Cyclic voltammetry results of pentacene and TSB3 molecules. [HOMO_Pentacene: −5.04 eV and HOMO_TSB3: −6.58 eV] d) Differential scanning calorimetry data of TSB3 molecules. The glass transition temperature (T_g) and melting temperature (T_m) of TSB3 were estimated to be 33 °C and 238 °C, respectively.

ULSAN NATIONAL INSTITUTE OF SCIENCE AND TECHNOLOGY

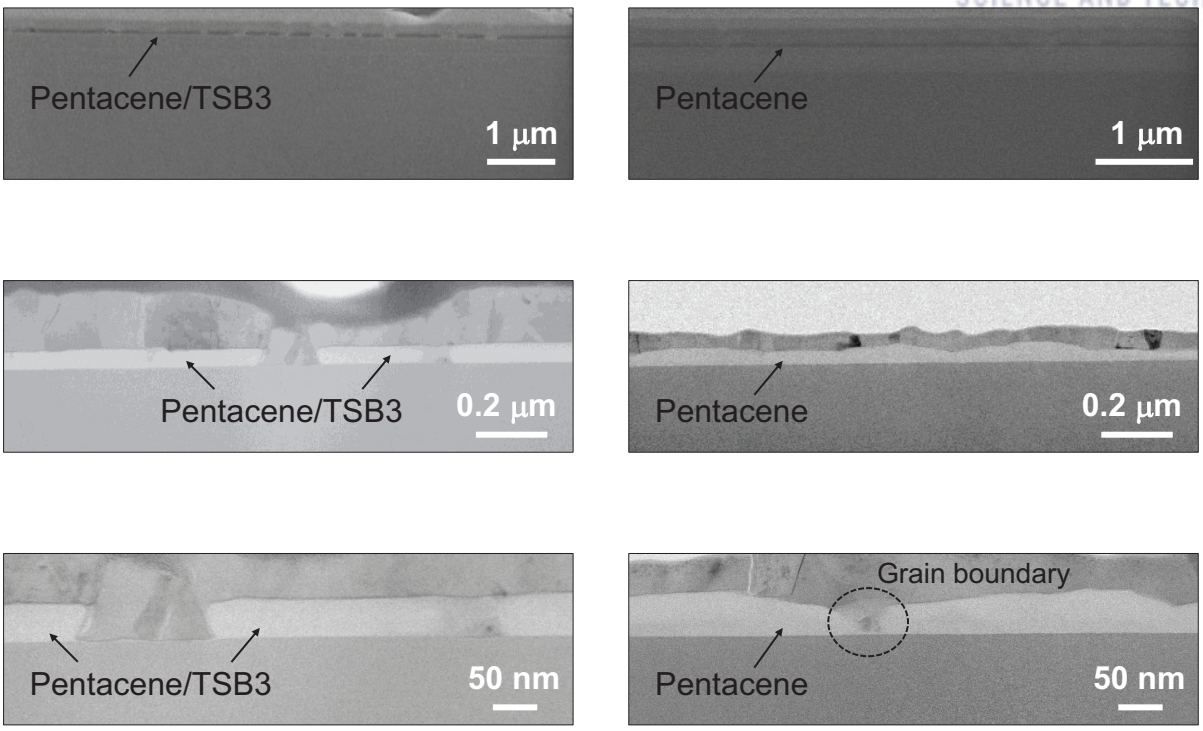

Figure 3.3. Cross-sectional SEM (first row) and HRTEM (second and third rows) images of pentacene (45 nm) / TSB3 (15 nm) and pentacene (45 nm) on OTS-treated SiO_2. The pentacene/TSB3 film exhibits much smoother surface than the pentacene film without TSB3, which corroborates more 2D growth of pentacene on TSB3.

ULSAN NATIONAL INSTITUTE OF SCIENCE AND TECHNOLOGY

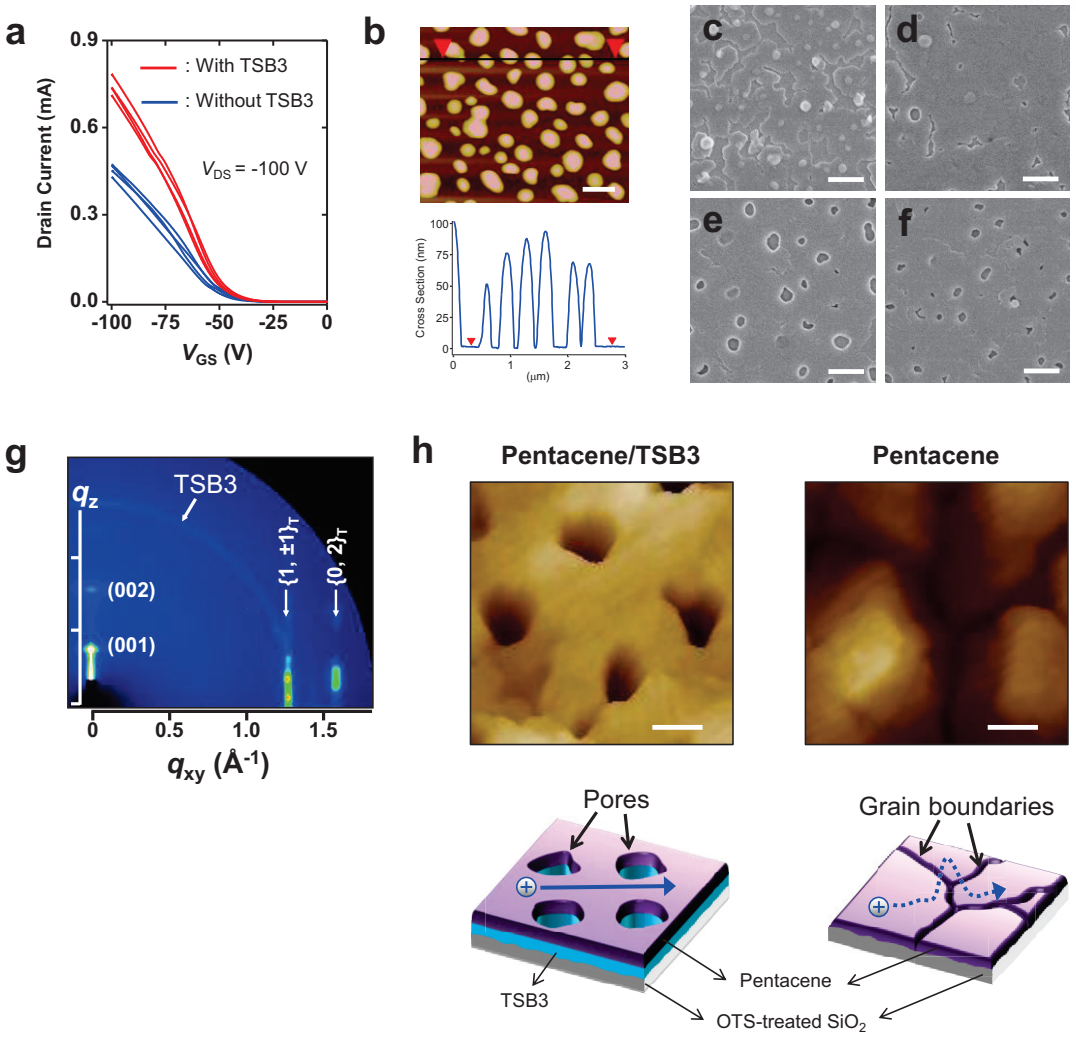

Figure 3.4. Electrical measurement data for the pentacene OFETs and morphological analysis: a) Current-voltage curves for pentacene OFETs with and without TSB3, measured inside a nitrogen-filled glovebox. Pentacene/TSB3 OFETs: [μ_{FET} = 5.5 (±0.7) cm^2 V^{-1} s^{-1}, V_{TH} = -37.5 (±0.8) V, I_{ON}/I_{OFF} = 3.7 (±0.5) ×10^6]; Pentacene OFETs: [μ_{FET} = 1.5 (±0.2) cm^2 V^{-1} s^{-1}, V_{TH} = -33.5 (±1.1) V, I_{ON}/I_{OFF} = 6.9 (±3.2) ×10^6] b) AFM height image and cross-sectional profile of a 15-nm-thick TSB3 film on OTS-treated SiO_2. When the TSB3 thin film is deposited without a rigid layer on top, the substrate surface is severely dewetted, and the TSB3 film becomes agglomerated. The scale bar is 500 nm. c–f) SEM images of pentacene (film thicknesses c) 5, d) 10, e) 20, f) 45 nm) / TSB3 (15 nm) on OTS-treated SiO_2. Similar to Figure 3.4b, clusters are also found in pentacene (5 and 10 nm) / TSB3 layers. However, such clusters are not observed when a thick layer of pentacene (20 and 45 nm) was deposited onto the TSB3 film. The scale bars are 500 nm. g) 2D GIXD image of pentacene (5 nm) / TSB3 (15 nm) on OTS-treated SiO_2. Predominantly the thin-film-phase peaks are present. h) Magnified AFM images of pentacene (45 nm) / TSB3 (15 nm) and pentacene (45 nm) on OTS-treated SiO_2, and a schematic diagram of the charge transport inside pentacene layers with and without TSB3. The scale bars are 200 nm.

ULSAN NATIONAL INSTITUTE OF SCIENCE AND TECHNOLOGY

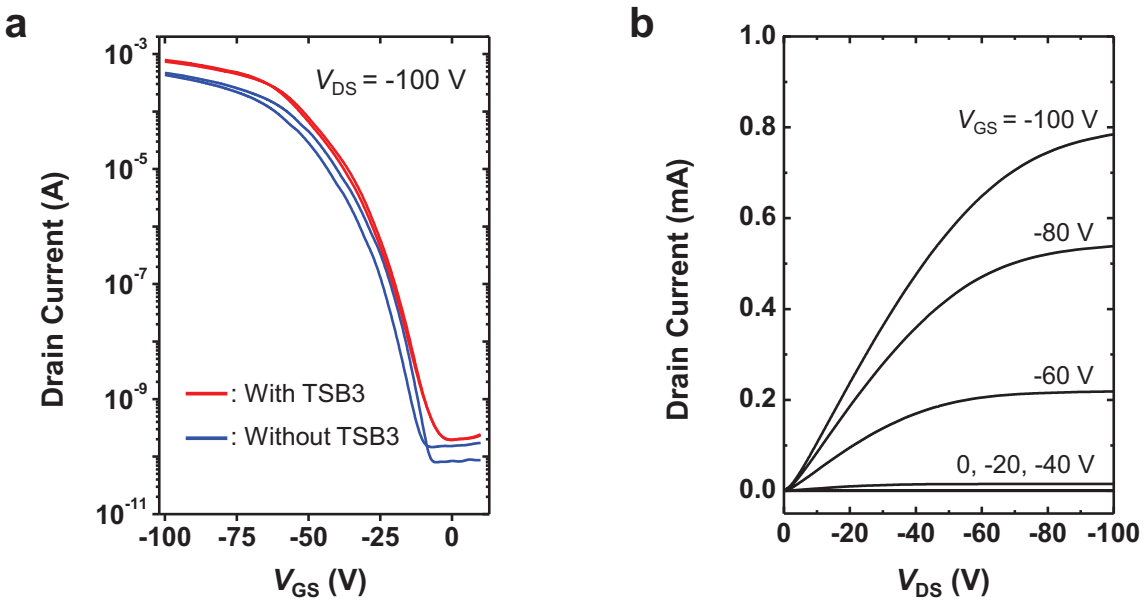

Figure 3.5. Current-voltage curves of pentacene OFETs measured inside a nitrogen-filled glovebox: a) Drain current vs. gate-source voltage curves with and without TSB3 in logarithmic scale. b) Drain current vs. drain-source voltage curves of pentacene OFET with TSB3.

ULSAN NATIONAL INSTITUTE OF SCIENCE AND TECHNOLOGY

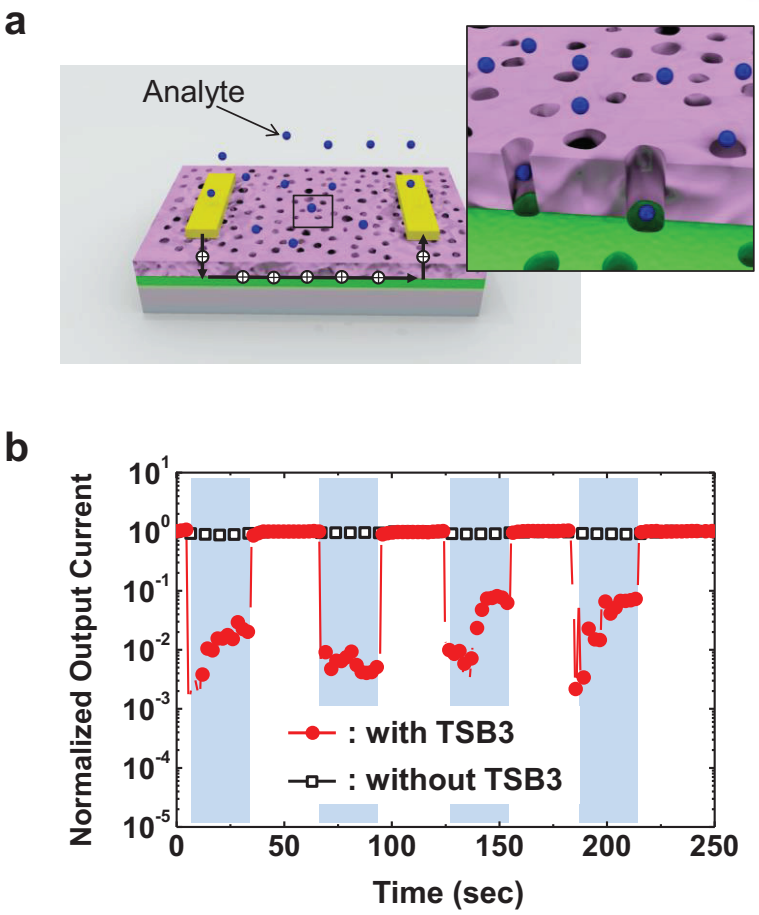

Figure 3.6. OFET-based chemical sensor utilizing the vertical macropores: a) Schematic diagram of an OFET-based sensor with macroporous layers made of pentacene and TSB3. b) Variation of the output current in the sensor as a function of time. The bias stress effect was compensated by dividing the measured current data by the current without the flow of analyte, and the data was normalized to the initial current at t=0. The blue regions indicate the flow of methanol gas (analyte). As clearly shown in the plot, the sensor with TSB3, having vertical macropores, exhibits higher sensitivity than the sensor without TSB3. Both V_{GS} and V_{DS} were fixed at -100 V.

ULSAN NATIONAL INSTITUTE OF SCIENCE AND TECHNOLOGY

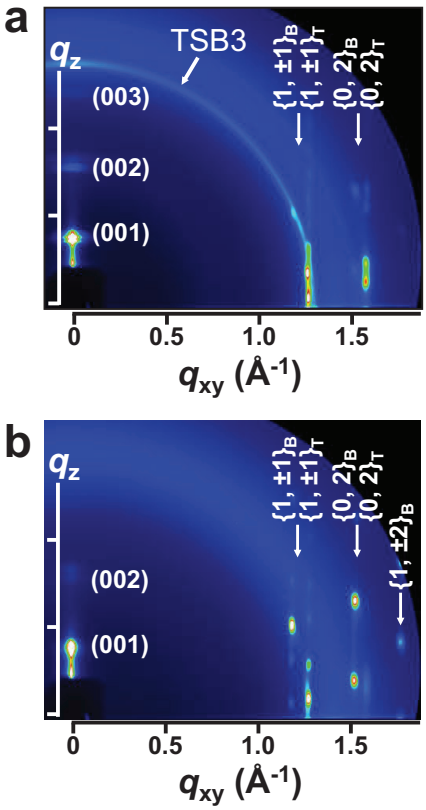

Figure 3.7. GIXD images of pentacene thin film with and without TSB3: a) Pentacene (45 nm) / TSB3 (15 nm) on OTS-treated SiO_2. The pentacene layer with TSB3 shows dominant thin-film-phase peaks. b) Pentacene (45 nm) on OTS-treated SiO_2. The pentacene layer without TSB3 shows dominant bulk-phase peaks.

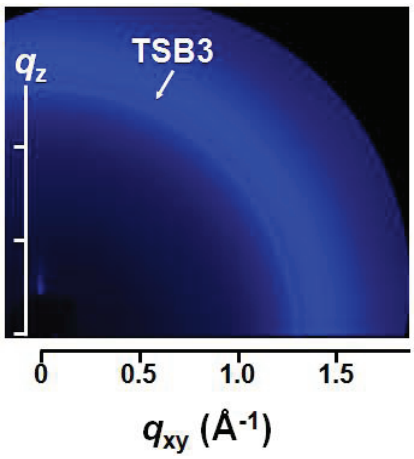

Figure 3.8. Two-dimensional grazing incidence X-ray diffraction pattern of 15-nm-thick TSB3 on OTS-treated SiO_2. The circular pattern indicates that the TSB3 film is not preferentially oriented on the substrate.

ULSAN NATIONAL INSTITUTE OF
SCIENCE AND TECHNOLOGY

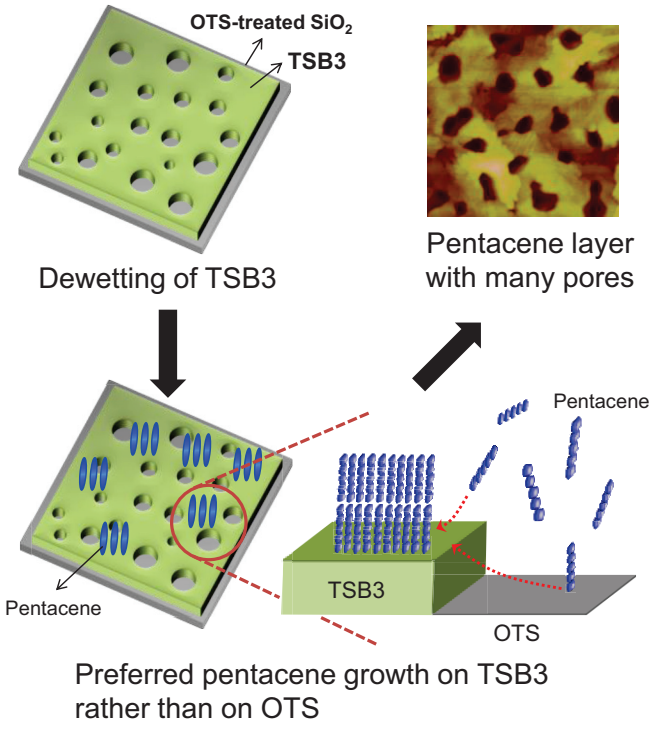

Figure 3.9. Proposed mechanism for the growth of pentacene on TSB3. In this growth model, the pores in pentacene are expected to form on the exposed OTS surface.

ULSAN NATIONAL INSTITUTE OF
SCIENCE AND TECHNOLOGY

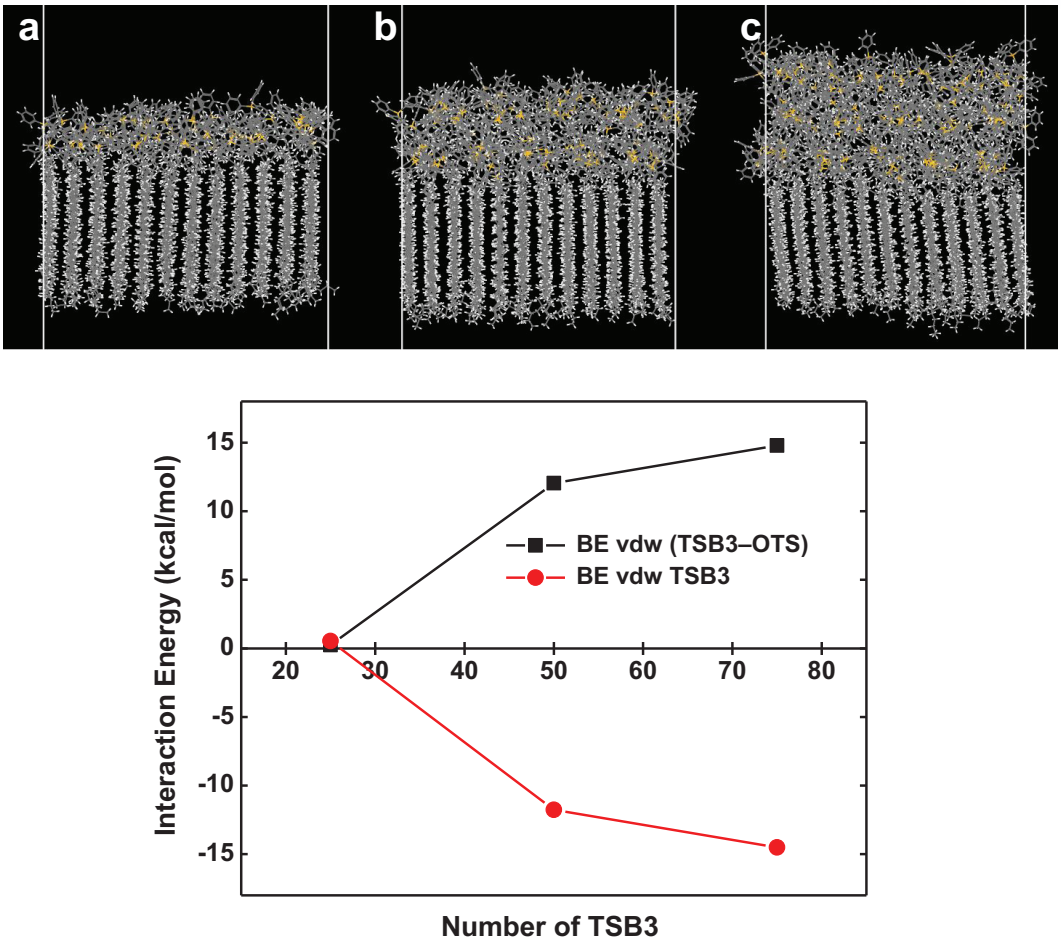

Figure 3.10. Snapshots of molecular dynamics systems of TSB3 on OTS and their van der Waals (vdw) interaction energies at 60 °C. Each system contains 144 OTS molecules in the bottom layer with a, 25, b, 50 and c, 75 TSB3 molecules on top. Vacuum is introduced above TSB3 and below OTS. The term "BE" stands for binding energy.

ULSAN NATIONAL INSTITUTE OF SCIENCE AND TECHNOLOGY

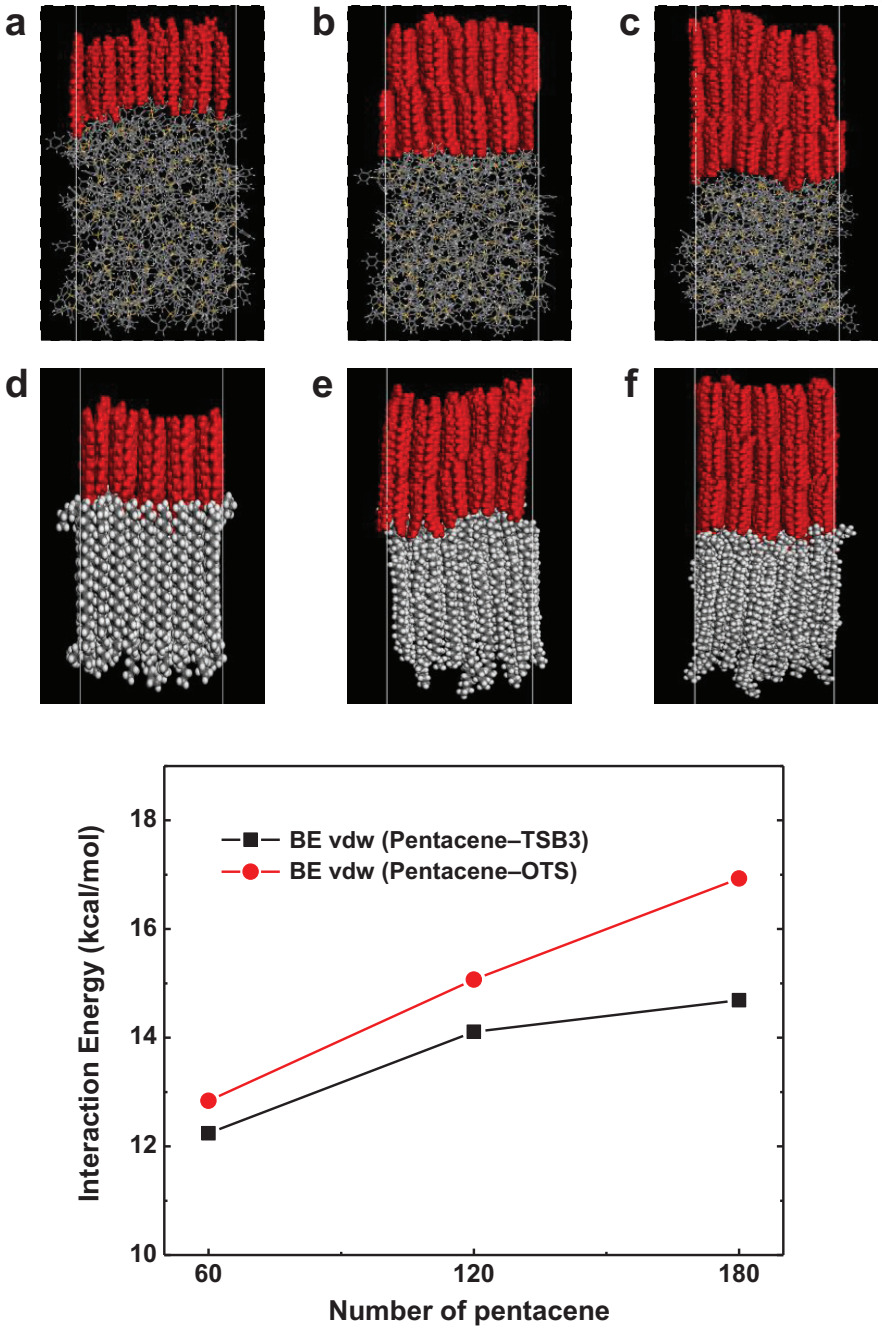

Figure 3.11. Snapshots of molecular dynamics systems of (a, b, c) pentacene on TSB3 and (d, e, f) pentacene on OTS, and their van der Waals (vdw) interaction energies at 60 °C. The TSB3 and OTS layers contain 66 and 81 molecules, respectively. One layer of pentacene is composed of 60 molecules. (a, d) Monolayers, (b, e) bilayers and (c, f) trilayers of pentacene were simulated. Vacuum is introduced above pentacene and below the bottom layer (TSB3 or OTS). The term "BE" stands for binding energy.

ULSAN NATIONAL INSTITUTE OF SCIENCE AND TECHNOLOGY

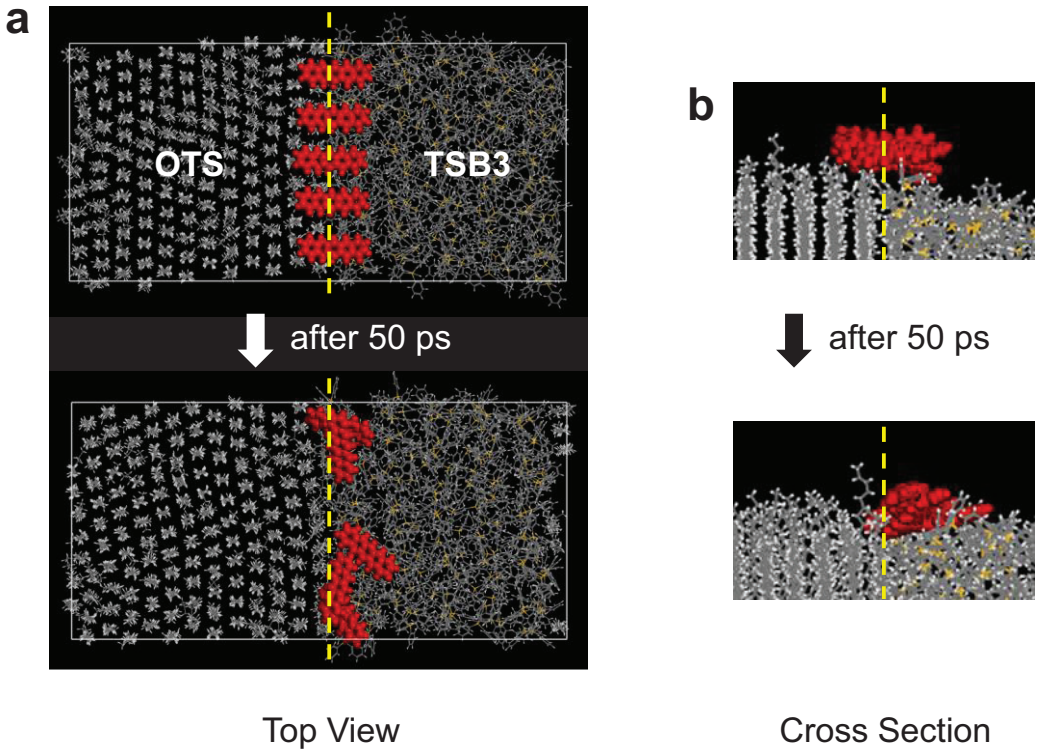

Figure 3.12. Molecular dynamics simulation of pentacene diffusion: a) Top-view and b) cross-sectional snapshots of the molecular dynamics system of pentacene on the interfacial region between TSB3 and OTS. The upper images show the beginning of the simulation. After 50 ps, the pentacene molecules gradually diffuse towards TSB3, which confirms that pentacene has higher attractive interaction with TSB3 than OTS. Yellow dashed lines indicate the boundary between OTS and TSB3.

ULSAN NATIONAL INSTITUTE OF SCIENCE AND TECHNOLOGY

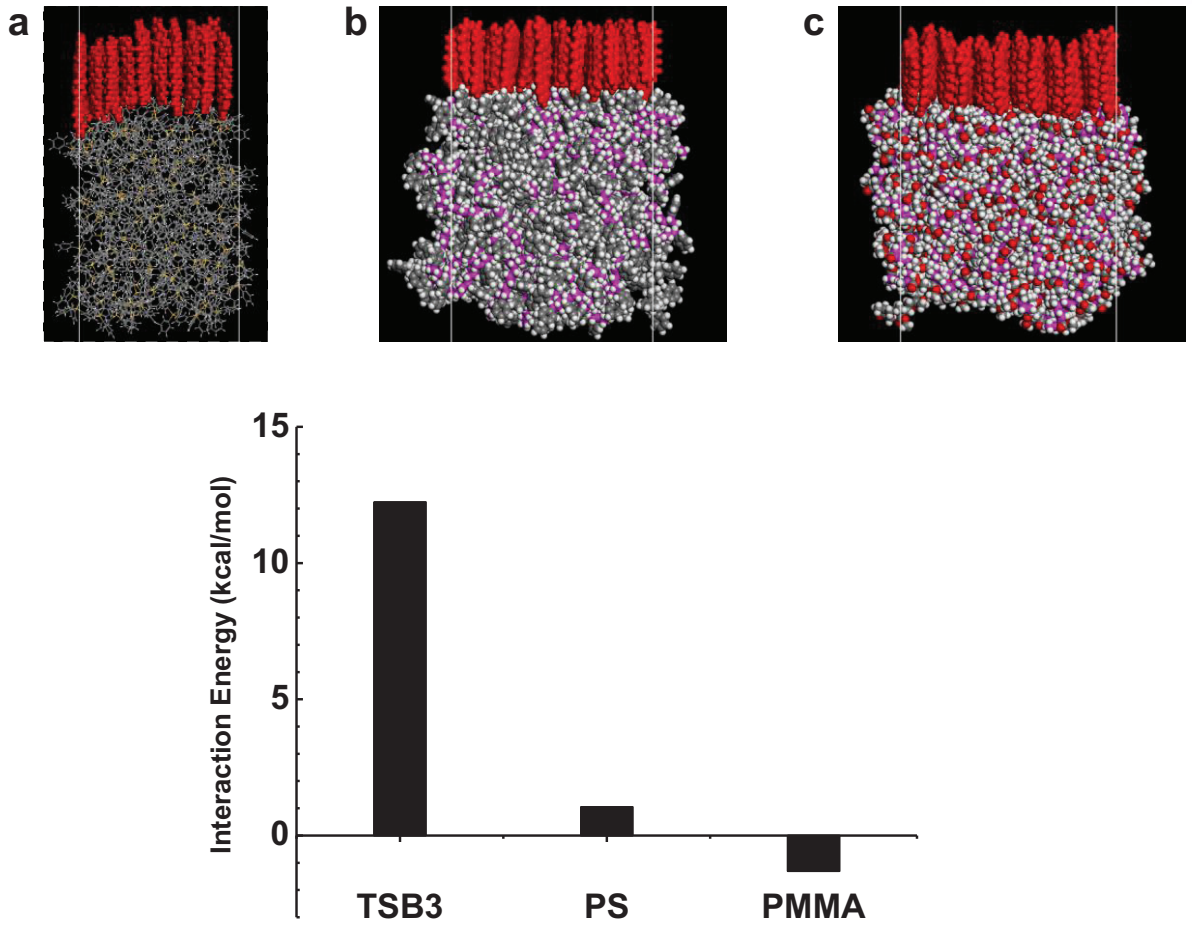

Figure 3.13. Snapshots of molecular dynamics systems of monolayer pentacene on a) TSB3, b) polystyrene (PS) and c) poly(methyl methacrylate) (PMMA), and their van der Waals interaction energies at 60 °C. a) The TSB3 and pentacene layers contain 66 and 60 molecules, respectively. b) and c) Each system contains 84 pentacene molecules on 50 decamers of PS or PMMA. Vacuum is introduced above pentacene and below the bottom layer (TSB3, PS or PMMA). The interaction energy in the y-axis represents binding energy.

ULSAN NATIONAL INSTITUTE OF SCIENCE AND TECHNOLOGY

Chapter 4

Highly Sensitive and Selective Biosensors Based on Functionalized Organic Semiconductors

Abstract

Biosensors based on a field-effect transistor (FET) platform allow continuous monitoring of biologically active species with high sensitivity due to the amplification capability of detected signals. To date, a large number of sensors for biogenic substances have used high-cost enzyme immobilization methods. Here, we report highly sensitive organic field-effect transistor (OFET)-based sensors functionalized with synthetic receptors that can selectively detect acetylcholine (ACh^+), a critical ion related to the delivery of neural stimulation. A cucurbit[6]uril (CB[6]) derivative, perallyloxyCB[6] ($(allyloxy)_{12}CB[6]$, AOCB[6]), which is soluble in methanol but insoluble in water, has been solution-deposited as a selective sensing layer onto a water-stable *p*-channel semiconductor, 5,5′-bis-(7-dodecyl-9H-fluoren-2-yl)-2,2′-bithiophene (DDFTTF) layer. The OFET-based sensors exhibit a detection limit down to 1 pM of ACh^+, which is six orders of magnitude lower than that of ion-selective electrode (ISE)-based sensors. Moreover, these OFET-based sensors show highly selective discrimination of ACh^+ over choline (Ch^+). Our findings demonstrate a viable method for the fabrication of OFET-based biosensors with high sensitivity and selectivity, and allow for practical applications of OFETs as high-performance sensors for biogenic substances.

ULSAN NATIONAL INSTITUTE OF SCIENCE AND TECHNOLOGY

4.1. Introduction

Sensors based on organic field-effect transistor (OFET) platforms show great promise for use in chemical and biological sensors, as they have many advantages including high sensitivity, ultra-low cost, simple fabrication, and flexible applications.[1-4] In particular, OFET-type sensors can amplify electrical signals obtained from binding events with analytes by tuning the applied gate voltage, leading to higher sensitivity compared to conventional sensors with two electrodes.[5-9] OFET-based sensors have been applied in various fields, such as environmental monitoring,[10, 11] drug delivery,[12, 13] food safety tests,[14, 15] and homeland security.[16, 17] One of our research groups has recently reported highly sensitive chemical sensors using highly crystalline pentacene layers with macroporous structures, which are helpful for the diffusion of analytes into the channel region.[18] However, pristine OFET-based sensors without additional functionalization often exhibit low selectivity for target analytes because all elements, including analytes and impurities that typically diffuse into the channel region through grain boundaries, can contribute to changes in the detected signal. Therefore, highly selective detection with OFET-based sensors requires chemical modification or immobilization of specific receptors to capture target analytes on a device surface.[19-28]

In particular, sensors for biogenic substances have received great interest for use in early diagnosis and consultation, and thereby for treating a disease during the initial stages. Acetylcholine (ACh^+) is a prominent neurotransmitter in the human central nervous system, and choline (Ch^+) is an important constituent of ACh^+. They are involved in various functions such as learning, memory, and muscle contraction.[29-31] More importantly, a deficiency in ACh^+ is associated with Alzheimer's disease, which is considered the most common neurodegenerative disease in the elderly. Therefore, the detection of ACh^+ concentration is of great importance for perceiving pathological conditions. Many amperometric sensors for the detection of ACh^+ have utilized enzyme immobilization by acetylcholine esterase (AChE) for enhanced selectivity of metabolic processes.[29, 32-35] The detection limits of these methods are typically in the range of μM to nM. Among them, ACh^+ sensors based on carbon nanotube FETs have shown outstanding performance with the detection limit of sub-nM (100 pM) due to their current-amplifying characteristics.[35] Despite their high sensitivity, these systems still require enzyme immobilization and have shortcomings such as high cost, lack of long-term stability, and complicated fabrication processes.

Recently, synthetic receptor-functionalized ion-selective electrodes (ISEs) have been reported as a reliable alternative to classical methods employing enzyme immobilization for making low-cost and high-performance electronic ACh^+ sensors.[36, 37] However, the two-electrode-system ISE sensors exhibit detection limits in the μM range for ACh^+, which is not sufficient for early-stage disease diagnosis. To date, there has been no report concerning synthetic receptor-functionalized FET-type sensors for the sensitive and selective detection of ACh^+ without any enzymatic reactions.

ULSAN NATIONAL INSTITUTE OF SCIENCE AND TECHNOLOGY

Here, we demonstrate highly sensitive and selective OFET-based ACh^+ sensors that function in the absence of AChE. A water-stable *p*-channel semiconductor, 5,5′-bis-(7-dodecyl-9H-fluoren-2-yl)-2,2′-bithiophene (DDFTTF) layer, was chosen as the active layer due to its relatively high mobility and operational stability in water.[38] In addition, a cucurbit[6]uril (CB[6]) derivative, perallyloxyCB[6] ($(allyloxy)_{12}$CB[6], AOCB[6]), was utilized as the receptor molecule to functionalize the semiconductor film.[39] CB[6] has a carbonyl group-fringed hydrophobic cavity (~5.5 Å diameter) which can encapsulate small organic molecules and ions.[40-43] Particularly, AOCB[6] shows high affinity and selectivity toward ACh^+,[36] and it is freely soluble in alcohol, but insoluble in water. Therefore, the AOCB[6] layer can easily be deposited using the spin coating method with an alcoholic solution of AOCB[6] on top of the DDFTTF semiconducting layer, and the deposited film acts as a stable and selective sensing layer for ACh^+ in the aqueous phase. Compared to previous highly sensitive ion-selective biosensors, our OFET-based sensors show remarkably enhanced sensitivity with the much lower detection limit, down to 1 pM of ACh^+, which is six orders of magnitude lower than that of ISE-based sensors. Moreover, these OFET-based sensors show highly selective discrimination of ACh^+ over choline (Ch^+). Our findings demonstrate the high effectiveness of a synthetic receptor-functionalized OFET platform for ACh^+ sensing. In addition, the developed OFET-based sensing platform provides a low-cost, simple, and viable approach for the fabrication of highly sensitive and selective water-stable OFET-based sensors for biogenic substances.

4.2. Experimental Section

Materials: Acetylcholine chloride, and choline chloride were used as received from Aldrich. DDFTTF was obtained from Lumtech (Taiwan). AOCB[6] was prepared according to the synthetic procedure reported in the literature.[39]

Fabrication of DDFTTF-Based OFET Sensors: Heavily n-doped Si wafers (<0.004 Ω cm) with a thermally grown 300 nm-thick oxide layer (SiO_2, C_g = 10 nF cm^{-2}) were cleaned with Piranha (H_2SO_4 and H_2O_2 with volume ratio of 7:3) solution. The SiO_2/Si substrates were sequentially modified by UV-ozone treatment. The SiO_2 surface was treated with OTS as self-assembled monolayer. The OTS solution (3 mM) prepared in trichloroethylene was spin-coated onto the wafers at 3000 rpm for 30 s, and then the wafers were placed overnight in a vacuum desiccator with ammonia vapor. The wafers were sequentially washed with toluene, acetone, and isopropyl alcohol, followed by drying under the gentle flow of nitrogen gas. The contact angle of DI water on the OTS-treated wafer was approximately 110°. The DDFTTF films (~15 nm thickness) were deposited by thermal evaporation at a rate of 0.1–0.2 Å s^{-1} under a base pressure of 5.0×10^{-6} torr. During the evaporation, the optimal substrate temperature for DDFTTF deposition was 105 °C. The films were annealed at 150 °C for 30 min in a nitrogen atmosphere. The top-contact bottom-gate devices were completed by depositing gold layer (~40 nm

ULSAN NATIONAL INSTITUTE OF SCIENCE AND TECHNOLOGY

thickness) through a shadow mask with a channel width (W) and a channel length (L) of 9000 μm and 50 μm, respectively. A silicon monoxide (SiO, ~20 nm thickness) layer was thermally deposited onto the electrodes except for the gold contacts. The SiO layer was used as a passivation layer for the liquid-phase sensing. Then, the solution-processable AOCB[6] (~5 mg mL^{-1} in methanol) was spin-coated onto the underlying film at 5000 rpm for 30 s. The films were dried in a vacuum oven at 60 °C for ~12 h and annealed at 150 °C for 30 min to remove the residual solvent.

Sensing Tests and Characterizations: For the sensing test, DDFTTF OFET-based sensors were exposed to solutions containing three analytes (acetylcholine chloride, choline chloride, and sodium chloride) in DI water. The electrical performance and sensing tests of OFETs were measured using a Keithley 4200 semiconductor parametric analyzer. The field-effect mobility ($_{FET}$) was calculated in the saturated regime with the following equation:

$$I_D = \frac{W}{2L}\mu_{FET}C_g\left(V_{GS}-V_{TH}\right)^2 \quad (1)$$

where I_D is the drain current, C_g is the capacitance per unit area of the gate dielectric layer, and V_{GS} and V_{TH} are the gate voltage and threshold voltage, respectively.

AFM characterization: AFM images were recorded with Agilent 5500 scanning probe microscope (SPM) running with a Nanoscope V controller. The film morphologies were characterized by high-resolution tapping mode under ambient conditions.

Density Functional Theory (DFT) Calculations: Since the guest binding of AOCB[6] is essentially the same as CB[6], we did the following calculations with CB[6]. To delineate the features of acetylcholine (ACh^+), choline (Ch^+) and Na^+ bound CB[6], we derived the gas phase structures of their 1:1 complexes in the regime of density functional theory (DFT). Hybrid meta exchange-correlation functional M06-2X, a member from family of Minnesota functional[44] was employed incorporating the 6-31G(d) basis set using Q-Chem software package.[45] All molecular structures in this work were built using the program Avogadro.[46] The binding energy ΔE_{bind} was obtained by subtracting the sum of the electronic energies of the unbound CB[6] and ACh^+, Ch^+, Na^+ from that of their corresponding complexes.

Molecular Dynamics (MD) Simulations and Natural Population Analysis (NPA): We parameterized atomic partial charges with the RESP approach[47] and adopted other parameters from the GAFF force field[48] for three guest molecules and CB[6]. In all cases, we solvated the complex of CB[6] and a guest molecule with TIP3P water[49] in a cubic box with each side of 35 Å, and a chloride ion is added to neutralize the system. For each complex, we conducted an equilibrium MD simulation for 3.5 ns after carrying out the energy minimization on initial structures. We propagated a MD trajectory for 1 ns for each given complex. The integration time step was 1 fs with constraints on hydrogen atoms with the LINCS algorithm.[50] Temperature was maintained at 300 K with the velocity rescaling thermostat proposed by Bussi et al.[51] and pressure was controlled to 1 atm with the Berendsen's weak coupling

ULSAN NATIONAL INSTITUTE OF SCIENCE AND TECHNOLOGY

scheme.[52] Non-covalent interactions in the range of 10−12 Å were gradually modified to zero at 12 Å. We sampled 500 structures from MD trajectories with 2 ps interval, and subsequently performed the natural population analysis (NPA)[53] on these sampled structures at M06-2X/6-31G(d) level with Q-Chem software package.[45] Specifically, we computed natural populations of CB[6] and guest molecules by treating water molecules and a chloride ion as point charges. The GROMACS software package[54] was used to carry out all MD simulations.

4.3. Results and Discussion

4.3.1. Device Fabrication and Characterization

OFET-based sensors with AOCB[6] were prepared with bottom-gate top-contact configuration. The DDFTTF thin film (~15 nm thickness) was thermally evaporated onto *n*-octadecyltrimethoxysilane (OTS)-treated SiO_2/Si substrates at an optimal substrate temperature of 105 °C. Source and drain electrodes (~40 nm thickness) were formed by evaporating gold through a shadow mask. In addition, the source and drain electrodes in the channel area were covered with a SiO passivation layer (~20 nm thickness). The SiO layer acts as an electrical insulator and chemical barrier to prevent the source-drain electrodes from peeling off during the OFET sensor operation in liquid solutions.[23, 38, 55] An AOCB[6] solution (~5 mg mL^{-1}) in methanol was spin-coated to form a stable and homogeneous receptor layer on the semiconductor film for selective analyte adsorption. Further details on the fabrication of OFET-based sensors are described in the Experimental Section. The corresponding device structure and AOCB[6] are shown in **Figure 4.1a** and **4.1b**, respectively. The electrical characteristics of OFETs with and without AOCB[6] were measured in the saturation regime as shown in **Figure 4.2**. The DDFTTF OFETs without AOCB[6] had an average field-effect mobility (μ_{FET}) of 0.053 $cm^2\ V^{-1}\ s^{-1}$, with an on/off current ratio (I_{on}/I_{off}) of more than 10^6. After functionalization with the AOCB[6] layer, the DDFTTF OFETs showed an average μ_{FET} of 0.028 $cm^2\ V^{-1}\ s^{-1}$ and I_{on}/I_{off} larger than 10^5. The electrical performances of DDFTTF OFETs fabricated with and without AOCB[6] are summarized in **Table 4.1**. The mobility degradation after functionalization with AOCB[6] may arise from the electron-donating effect of AOCB[6] molecules that decreases the density of holes (charge carriers of *p*-channel devices), as well as from the trapped impurities generated during solution processing.[56] The off-current increased by one order of magnitude most likely due to the effect of doping by oxygen, leading to the decreased I_{on}/I_{off} under ambient conditions.[57] The threshold voltage (V_{TH}) was changed from –26.3 V to –5.6 V, indicative of the easier turn-on after functionalization with AOCB[6]. Despite the minor degradation in the charge carrier mobility of the OFET devices, they showed ample device performance for sensing analytes in the aqueous phase (*vide infra*).

4.3.2. Thin-Film Microstructure Analysis

ULSAN NATIONAL INSTITUTE OF SCIENCE AND TECHNOLOGY

We investigated the morphological characteristics of organic thin films using atomic force microscopy (AFM) analysis (see **Figure 4.3**). The DDFTTF thin films showed various grain sizes and distinct grain boundaries with a relatively large surface roughness (a root-mean-square (RMS) roughness of 7.5 nm) (**Figure 4.3a** and **4.3b**). The thin films became smoother with a RMS roughness of 1.8 nm after thermal annealing at 150 °C (**Figure 4.3c** and **4.3d**). The AOCB[6] layer spin-coated on DDFTTF film was annealed at 150 °C in a nitrogen atmosphere to remove the residual solvent. The thermogravimetric analysis (TGA) of AOCB[6] revealed that it was stable up to ~310 °C. The AOCB[6] layer covered the DDFTTF device uniformly and completely with a RMS roughness of 2.5 nm (**Figure 4.3e** and **4.3f**), and the cross-sectional AFM analysis revealed that the thickness of the AOCB[6] layer was 17.0 nm. As the height and diameter of AOCB[6] was about 0.9 nm and 2.2 nm, respectively, it is considered that approximately 10 or more layers of AOCB[6] were deposited with a high density on the semiconductor film.

4.3.3. Sensitivity and Selectivity of OFET-Based Sensors

In OFET-based sensors, chemical or physical adsorption of target analytes leads to a change in the channel current, which depends on the analyte composition, concentration, and OFET operating conditions.[24, 58-60] In addition, the OFET-based sensors have excellent current-amplifying properties induced by an external gate field. A sensing platform was prepared by placing a polydimethylsiloxane (PDMS) mold reservoir onto the OFET sensor device, and sensing experiments were performed under ambient conditions. Prior to detecting the analytes, a baseline current was estimated with deionized (DI) water. The DDFTTF OFET-based sensors exhibited minimal sensing signals upon continuous exposure to DI water, as shown in **Figure 4.4a**. After stabilizing the drain current, solutions (~15 μL) containing analytes were injected into the PDMS reservoir. The sensitivity of sensors was calculated by dividing the measured data by the baseline current.

Figure 4.4a shows the liquid-phase sensing behaviors of DDFTTF OFET-based sensors functionalized with AOCB[6] toward ACh^+ and Ch^+. The sensors showed positive sensing behaviors, in which the drain current was enhanced after injection of the analytes. Surprisingly, the detection limit (1 pM) of the DDFTTF sensors with AOCB[6] toward ACh^+ was six orders of magnitude lower than that (~μM) of ISE-based sensors[36] and two orders of magnitude lower than that (100 pM) of AChE-based biosensors,[35] respectively. We also monitored changes in the drain current of the sensors with and without the AOCB[6] layer, while the devices were exposed to 1 pM of ACh^+ (**Figure 4.5**). The sensors with AOCB[6] showed much higher sensitivity for ACh^+ compared to the sensors without AOCB[6]. The OFET-based sensors without AOCB[6] exhibited low sensitivity because the grain boundary defects in organic semiconductors could solely provide pathways for the diffusion of analytes into the channel region. These results indicate that introduction of the AOCB[6] layer significantly improves the sensitivity of the sensors through selective binding of ACh^+ on the device surface.

In addition, responses of the sensors with AOCB[6] toward sodium ion (Na^+), which is also known

ULSAN NATIONAL INSTITUTE OF SCIENCE AND TECHNOLOGY

as interfering species for the detection of ACh^+, were monitored (**Figure 4.6a**). Interestingly, the sensing signals of Ch^+ and Na^+ were very different from ACh^+. For Ch^+, almost no signals were detected at concentrations lower than μM. Moreover, no signals were detected for Na^+ at μM concentrations. **Figure 4.4b** shows the statistical comparison of the sensing data for the concentration of ACh^+ and Ch^+. The change in the drain current for ACh^+ was observed at a wide concentration range (1 pM – 100 mM), whereas the sensors for Ch^+ and Na^+ (**Figure 4.6b**) exhibited no detectable signals at concentrations lower than 1 μM. These results support the excellence of our sensor devices for the selective and sensitive detection of ACh^+. Such superior sensing ability of our sensor devices originates from the commendable combination of highyl selective synthetic receptors and highly sensitive OFET devices. We also monitored sensing signals of ACh^+ by using a baseline buffer solution, instead of DI water (**Figure 4.7**). For the sensing test, acetylcholine chloride solutions were prepared in a phosphate-buffered saline (PBS) solution (pH 7.4, 0.01 M) containing sodium chloride (137 mM) and potassium chloride (2.7 mM). This sensing condition was close to the normal physiological conditions found in blood. The AOCB[6]-functionalized OFET sensors could also detect ACh^+ with the detection limit down to 1 pM in the PBS solution, although they exhibited relatively lower sensitivity compared with that in DI water due to the interfering effects of cations.

To understand the superior selective sensing nature of our sensor devices, we performed density functional theory (DFT) calculations of AOCB[6] with these three analytes. In these calculations, CB[6] was used as a host material because the guest binding nature of AOCB[6] is essentially the same as CB[6]. Note that the allyloxy group is only introduced for solvent orthogonality. DFT optimized structures of ACh^+ and Ch^+ interacting with the CB[6] host are shown in **Figure 4.8**. In the energy-minimized configuration, ACh^+ is parallel to the cavity axis and the acetyloxy end group was penetrated inside the cavity with its methyl group interacting with one of the carbonyl portals. The positively charged trimethylammonium group was located over the opposite carbonyl portal. Thus, complexation between CB[6] and ACh^+ showed a strong binding energy of −86.5 kcal mol^{-1}, which is attributed to the strong charge-diople interactions and hydrogen bonding between CB[6] and ACh^+. When AOCB[6] forms a complex with ACh^+, the carbonyl group of AOCB[6] would partially donate electrons to the positively charged ammonium group of ACh^+, and these charge-dipole interactions tend to increase the electron-withdrawing characteristics into the channel region, thereby leading to an increase in the hole current of the *p*-channel OFET sensor devices. For complexation between CB[6] and Ch^+, the ammonium group of Ch^+ weakly interacts with the portal of the host and the hydroxyethyl group of Ch^+ does not enter the host cavity. Thus, AOCB[6] forms a weak host-guest complex with Ch^+, which showed a lower binding energy of –69.5 kcal mol^{-1} than that of CB[6]-ACh^+. The calculated structures were well matched with the ^{1}H-NMR spectra of each complex.[36, 37] In ^{1}H-NMR, protons of trimethylammonium groups of ACh^+ show small downfield shifts and protons of the acetyl group show large upfield shifts upon complexation with AOCB[6], which indicate the formation of strong host-

ULSAN NATIONAL INSTITUTE OF SCIENCE AND TECHNOLOGY

guest complexes as shown in **Figure 4.8a**. However, all protons of Ch^+ show very small downfield shifts upon addition of AOCB[6], which indicates that the ammonium group of Ch^+ interacts weakly with the portals of the host and the hydroxyethyl of the molecule exists outside the cavity, as shown in **Figure 4.8b**. For complexation between CB[6] and Na^+, Na^+ interacts weakly at the portal of the host (**Figure 4.9**).

Since DDFTTF OFET-based sensors are *p*-channel devices, complexation of the host molecule with cationic guest molecules would increase the signals by increasing the hole carrier density in the channel region owing to the overall electron-withdrawing characteristics toward the active layer. Because all three analytes have the same +1 charge, we assume that the differences between sensing behaviors of guest molecules should be related to their binding constants to the host molecule. In addition to this, the partial charge change differences of the host molecule upon complexation with each guest molecule would also affect the differences in the sensing signals. Therefore, we calculated the partial charge changes in the host molecule upon complexation with each guest molecule (**Figure 4.10**). As in the case of sensing signals, complexation with ACh^+ shows the largest charge changes on CB[6] (0.063 ±0.008), Na^+ shows the smallest charge changes (0.020 ±0.005), and Ch^+ shows moderate changes (0.052 ±0.009). Considering the sensing results of each molecule, the difference in charge changes between ACh^+ and Ch^+ should be larger than the value shown in **Figure 4.10**. The reason for the difference between calculated and experimental results may originate from the differences in binding probabilities (i.e. binding constant) of each guest molecule to the host molecule on the device surface. In contrast to ACh^+, which strongly binds to the host, Ch^+ has a very weak interaction with the host. These large differences in the binding probability and accumulation of each binding event on the device surface may cause such a large difference in the sensing signals.

For ACh^+ sensors, a significant analytical challenge is the detection of ACh^+ with high sensitivity and selectivity in the presence of Ch^+. Thus, the signal intensities of the sensors for analyte blend systems were investigated using a mixture solution of two analytes (**Figure 4.11**). Mixed solutions containing 1 μM ACh^+ and Ch^+ analytes were prepared with various volume ratios (1:1, 2:1, and 3:1) of ACh^+ relative to Ch^+. The sensors with AOCB[6] showed enhanced signal intensities with an increasing volume ratio of ACh^+ in the mixed solutions, indicative of the high selectivity toward ACh^+ compared to Ch^+. This was due to the relatively higher binding affinity of AOCB[6] toward ACh^+ compared to Ch^+.

In addition to amplification of the detected signals, OFET-based sensors are suitable for applications in low-cost and flexible electronics. To explore the possibility of using a flexible sensor platform, our sensors were also fabricated with indium tin oxide (ITO)-coated polyethylene naphthalate (PEN) as the polymer substrate and aluminum oxide (Al_2O_3) as the transparent dielectric (**Figure 4.12a**). A 100 nm-thick Al_2O_3 gate dielectric layer was deposited on the PET substrate via a radio frequency (RF) magnetron sputtering technique, and a photograph of the resulting flexible sensor is shown in **Figure**

ULSAN NATIONAL INSTITUTE OF SCIENCE AND TECHNOLOGY

4.12b. The transfer and output characteristics of the DDFTTF OFET-based sensor with AOCB[6] are shown in **Figure 4.13a** and **4.13b**, respectively. The results of the sensing experiments for ACh^+ exhibited performances similar to SiO_2 dielectric-based sensors. The flexible sensors could also detect ACh^+ with a detection limit of 1 pM under low-voltage operation conditions (V_{DS} = −0.5 V and V_{GS} = −10 V) (**Figure 4.12c**). These results describe the first demonstration of ACh^+ sensing without any enzymatic reactions using synthetic receptor-functionalized flexible FET-type sensors. In addition, our findings expand the range of practical applications of OFET-based sensors.

4.4. Conclusion

We demonstrated highly sensitive OFET-based sensors that can selectively detect a neurotransmitter in the human central nervous system, ACh^+, without enzyme immobilization processes. AOCB[6], a synthetic receptor molecule with selective recognition sites for ACh^+, could effectively be functionalized on top of the water-stable organic semiconductor DDFTTF layer due to solvent orthogonality. All OFET-based sensors prepared on a rigid Si wafer and a flexible plastic substrate showed a detection limit for ACh^+ down to 1 pM, which was six orders of magnitude lower than the detection limit (~μM) of ISE-based sensors and two orders of magnitude lower than that (100 pM) of AChE-based biosensors, respectively. Furthermore, the sensors could detect ACh^+ with high sensitivity and selectivity even in the presence of Ch^+, due to the higher binding affinity of AOCB[6] toward ACh^+ compared to Ch^+. These results describe the first demonstration of ACh^+ sensing without any enzymatic reactions using a synthetic receptor-functionalized OFET-platform. This work also describes a low-cost, simple, and viable methodology for the fabrication of highly sensitive and selective water-stable OFET-based sensors for biogenic substances, and opens up the possibilities of replacing current enzyme-based biosensors.

ULSAN NATIONAL INSTITUTE OF SCIENCE AND TECHNOLOGY

4.5. References

[1] Janata J., Josowicz M., *Nat. Mater.* **2003**, *2*, 19-24.
[2] Hammock M. L.; Knopfmacher O.; Naab B. D.; Tok J. B. H., Bao Z., *ACS Nano* **2013**, *7*, 3970-3980.
[3] Royer J. E.; Lee S.; Chen C.; Ahn B.; Trogler W. C.; Kanicki J., Kummel A. C., *Sens. Actuators B* **2011**, *158*, 333-339.
[4] Tanese M. C.; Fine D.; Dodabalapur A., Torsi L., *Biosens. Bioelectr.* **2005**, *21*, 782-788.
[5] Roberts M. E.; Sokolov A. N., Bao Z., *J. Mater. Chem.* **2009**, *19*, 3351-3363.
[6] Lin P., Yan F., *Adv. Mater.* **2012**, *24*, 34-51.
[7] Yu H.; Bao Z., Oh J. H., *Adv. Funct. Mater.* **2013**, *23*, 629-639.
[8] Yan F., Tang H., *Expert Rev. Mol. Diagn.* **2010**, *10*, 547-549.
[9] Yu H.; Joo P.; Lee D.; Kim B.-S., Oh J. H., *Adv. Optical Mater.* **2015**, *3*, 241-247.
[10] Zang Y.; Zhang F.; Huang D.; Di C.-a.; Meng Q.; Gao X., Zhu D., *Adv. Mater.* **2014**, *26*, 2862-2867.
[11] Huang W.; Yu J.; Yu X., Shi W., *Org. Electron.* **2013**, *14*, 3453-3459.
[12] Angione M. D.; Cotrone S.; Magliulo M.; Mallardi A.; Altamura D.; Giannini C.; Cioffi N.; Sabbatini L.; Fratini E.; Baglioni P.; Scamarcio G.; Palazzo G., Torsi L., *Proc. Natl. Acad. Sci. U.S.A.* **2012**, *109*, 6429-6434.
[13] Berggren M., Richter-Dahlfors A., *Adv. Mater.* **2007**, *19*, 3201-3213.
[14] Park S. J.; Kwon O. S.; Lee S. H.; Song H. S.; Park T. H., Jang J., *Nano Lett.* **2012**, *12*, 5082-5090.
[15] Bartic C., Borghs G., *Anal. Bioanal. Chem.* **2006**, *384*, 354-365.
[16] Huang J.; Dawidczyk T. J.; Jung B. J.; Sun J.; Mason A. F., Katz H. E., *J. Mater. Chem.* **2010**, *20*, 2644-2650.
[17] Kong H.; Jung B. J.; Sinha J., Katz H. E., *Chem. Mater.* **2012**, *24*, 2621-2623.
[18] Kang B.; Jang M.; Chung Y.; Kim H.; Kwak S. K.; Oh J. H., Cho K., *Nat. Commun.* **2014**, *5*, 4752.
[19] Someya T.; Dodabalapur A.; Huang J.; See K. C., Katz H. E., *Adv. Mater.* **2010**, *22*, 3799-3811.
[20] Sokolov A. N.; Roberts M. E.; Johnson O. B.; Cao Y., Bao Z., *Adv. Mater.* **2010**, *22*, 2349-2353.
[21] Yoon H.; Ko S., Jang J., *J. Phys. Chem. B* **2008**, *112*, 9992-9997.
[22] Khan H. U.; Roberts M. E.; Johnson O.; Knoll W., Bao Z., *Org. Electron.* **2012**, *13*, 519-524.
[23] Khan H. U.; Roberts M. E.; Johnson O.; Förch R.; Knoll W., Bao Z., *Adv. Mater.* **2010**, *22*, 4452-4456.
[24] Khan H. U.; Jang J.; Kim J.-J., Knoll W., *J. Am. Chem. Soc.* **2011**, *133*, 2170-2176.
[25] Lee M. Y.; Kim H. J.; Jung G. Y.; Han A. R.; Kwak S. K.; Kim B. J., Oh J. H., *Adv. Mater.* **2015**, *27*, 1540-1546.
[26] Mulla M. Y.; Tuccori E.; Magliulo M.; Lattanzi G.; Palazzo G.; Persaud K., Torsi L., *Nat. Commun.* **2015**, *6*, 6010.
[27] Torsi L.; Farinola G. M.; Marinelli F.; Tanese M. C.; Omar O. H.; Valli L.; Babudri F.; Palmisano F.; Zambonin P. G., Naso F., *Nat. Mater.* **2008**, *7*, 412-417.
[28] Magliulo M.; Mallardi A.; Mulla M. Y.; Cotrone S.; Pistillo B. R.; Favia P.; Vikholm-Lundin I.; Palazzo G., Torsi L., *Adv. Mater.* **2013**, *25*, 2090-2094.
[29] Liu Y.; Erdman A. G., Cui T., *Sens. Actuators A* **2007**, *136*, 540-545.
[30] Croxson P. L.; Kyriazis D. A., Baxter M. G., *Nat. Neurosci.* **2011**, *14*, 1510-1512.
[31] Niwa O.; Horiuchi T.; Kurita R., Torimitsu K., *Anal. Chem.* **1998**, *70*, 1126-1132.
[32] Zhao W.; Sun S.-X.; Xu J.-J.; Chen H.-Y.; Cao X.-J., Guan X.-H., *Anal. Chem.* **2008**, *80*, 3769-3776.
[33] Zhang L.; Chen J.; Wang Y.; Yu L.; Wang J.; Peng H., Zhu J., *Sens. Actuators B* **2014**, *193*, 904-910.
[34] Kergoat L.; Piro B.; Simon D. T.; Pham M.-C.; Noël V., Berggren M., *Adv. Mater.* **2014**, *26*, 5658-5664.

ULSAN NATIONAL INSTITUTE OF SCIENCE AND TECHNOLOGY

[35] Kim B.; Song H. S.; Jin H. J.; Park E. J.; Lee S. H.; Lee B. Y.; Park T. H., Hong S., *Nanotechnology* **2013**, *24*, 285501.
[36] Kim H.; Oh J.; Jeon W. S.; Selvapalam N.; Hwang I.; Ko Y. H., Kim K., *Supramol. Chem.* **2012**, *24*, 487-491.
[37] Zhao J.; Kim H.-J.; Oh J.; Kim S.-Y.; Lee J. W.; Sakamoto S.; Yamaguchi K., Kim K., *Angew. Chem. Int. Ed.* **2001**, *113*, 4363-4365.
[38] Roberts M. E.; Mannsfeld S. C. B.; Queraltó N.; Reese C.; Locklin J.; Knoll W., Bao Z., *Proc. Natl. Acad. Sci. U.S.A.* **2008**, *105*, 12134-12139.
[39] Jon S. Y.; Selvapalam N.; Oh D. H.; Kang J.-K.; Kim S.-Y.; Jeon Y. J.; Lee J. W., Kim K., *J. Am. Chem. Soc.* **2003**, *125*, 10186-10187.
[40] Lee J. W.; Samal S.; Selvapalam N.; Kim H.-J., Kim K., *Acc. Chem. Res.* **2003**, *36*, 621-630.
[41] Lagona J.; Mukhopadhyay P.; Chakrabarti S., Isaacs L., *Angew. Chem. Int. Ed.* **2005**, *44*, 4844-4870.
[42] Masson E.; Ling X.; Joseph R.; Kyeremeh-Mensah L., Lu X., *RSC Adv.* **2012**, *2*, 1213-1247.
[43] Assaf K. I., Nau W. M., *Chem. Soc. Rev.* **2015**, *44*, 394-418.
[44] Zhao Y., Truhlar D. G., *Theor Chem Account* **2008**, *120*, 215-241.
[45] Shao Y.; Molnar L. F.; Jung Y.; Kussmann J.; Ochsenfeld C.; Brown S. T.; Gilbert A. T. B.; Slipchenko L. V.; Levchenko S. V.; O'Neill D. P.; DiStasio Jr R. A.; Lochan R. C.; Wang T.; Beran G. J. O.; Besley N. A.; Herbert J. M.; Yeh Lin C.; Van Voorhis T.; Hung Chien S.; Sodt A.; Steele R. P.; Rassolov V. A.; Maslen P. E.; Korambath P. P.; Adamson R. D.; Austin B.; Baker J.; Byrd E. F. C.; Dachsel H.; Doerksen R. J.; Dreuw A.; Dunietz B. D.; Dutoi A. D.; Furlani T. R.; Gwaltney S. R.; Heyden A.; Hirata S.; Hsu C.-P.; Kedziora G.; Khalliulin R. Z.; Klunzinger P.; Lee A. M.; Lee M. S.; Liang W.; Lotan I.; Nair N.; Peters B.; Proynov E. I.; Pieniazek P. A.; Min Rhee Y.; Ritchie J.; Rosta E.; David Sherrill C.; Simmonett A. C.; Subotnik J. E.; Lee Woodcock Iii H.; Zhang W.; Bell A. T.; Chakraborty A. K.; Chipman D. M.; Keil F. J.; Warshel A.; Hehre W. J.; Schaefer Iii H. F.; Kong J.; Krylov A. I.; Gill P. M. W., Head-Gordon M., *Phys. Chem. Chem. Phys.* **2006**, *8*, 3172-3191.
[46] Hanwell M. D.; Curtis D. E.; Lonie D. C.; Vandermeersch T.; Zurek E., Hutchison G. R., *J. Cheminformatics* **2012**, *4*, 17.
[47] Wang J.; Cieplak P., Kollman P. A., *J. Comput. Chem.* **2000**, *21*, 1049-1074.
[48] Wang J.; Wolf R. M.; Caldwell J. W.; Kollman P. A., Case D. A., *J. Comput. Chem.* **2004**, *25*, 1157-1174.
[49] Jorgensen W. L.; Chandrasekhar J.; Madura J. D.; Impey R. W., Klein M. L., *J. Chem. Phys.* **1983**, *79*, 926-935.
[50] Hess B.; Bekker H.; Berendsen H. J., Fraaije J. G., *J. Comput. Chem.* **1997**, *18*, 1463-1472.
[51] Bussi G.; Donadio D., Parrinello M., *J. Chem. Phys.* **2007**, *126*, 014101.
[52] Berendsen H. J. C.; Postma J. P. M.; van Gunsteren W. F.; DiNola A., Haak J. R., *J. Chem. Phys.* **1984**, *81*, 3684-3690.
[53] Reed A. E.; Curtiss L. A., Weinhold F., *Chem. Rev.* **1988**, *88*, 899-926.
[54] Van Der Spoel D.; Lindahl E.; Hess B.; Groenhof G.; Mark A. E., Berendsen H. J. C., *J. Comput. Chem.* **2005**, *26*, 1701-1718.
[55] Bradley K.; Gabriel J.-C. P.; Star A., Grüner G., *Appl. Phys. Lett.* **2003**, *83*, 3821-3823.
[56] Kalb W. L.; Mattenberger K., Batlogg B., *Phys. Rev. B* **2008**, *78*, 035334.
[57] Bao Z., *Adv. Mater.* **2000**, *12*, 227-230.
[58] Huang W.; Sinha J.; Yeh M.-L.; Hardigree J. F. M.; LeCover R.; Besar K.; Rule A. M.; Breysse P. N., Katz H. E., *Adv. Funct. Mater.* **2013**, *23*, 4094-4104.
[59] Hammock M. L.; Sokolov A. N.; Stoltenberg R. M.; Naab B. D., Bao Z., *ACS Nano* **2012**, *6*, 3100-3108.
[60] Liao F.; Chen C., Subramanian V., *Sens. Actuators B* **2005**, *107*, 849-855.

Reprinted in part with permission from M. Jang, *et al*., *Adv. Funct. Mater.* **2015, *25*, 4882–4888. Copyright © 2015 WILEY-VCH Verlag GmbH & Co. KGaA, Weinheim.

ULSAN NATIONAL INSTITUTE OF SCIENCE AND TECHNOLOGY

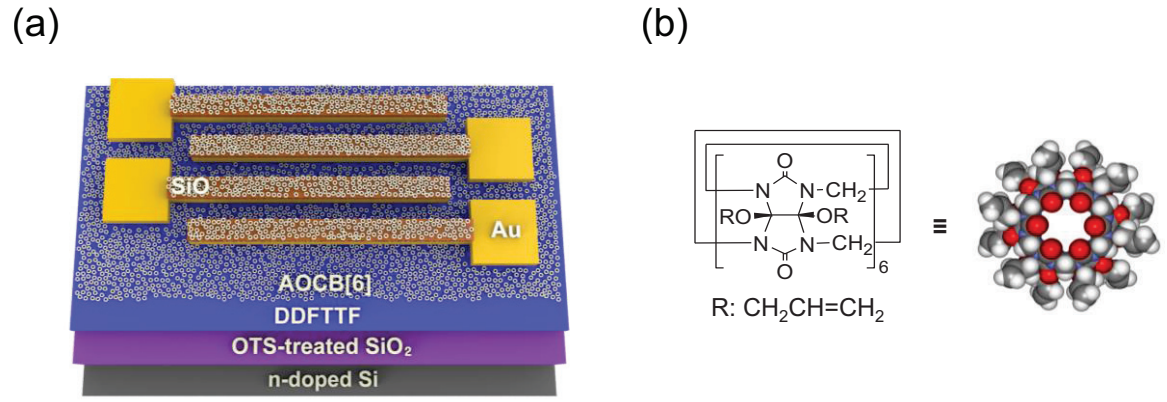

Figure 4.1. a) Schematic illustration of the top-contact OFET-based sensors with a synthetic receptor, AOCB[6], and b) the molecular structure of AOCB[6]. In the device structure, only monolayer of AOCB[6] is shown for clarity.

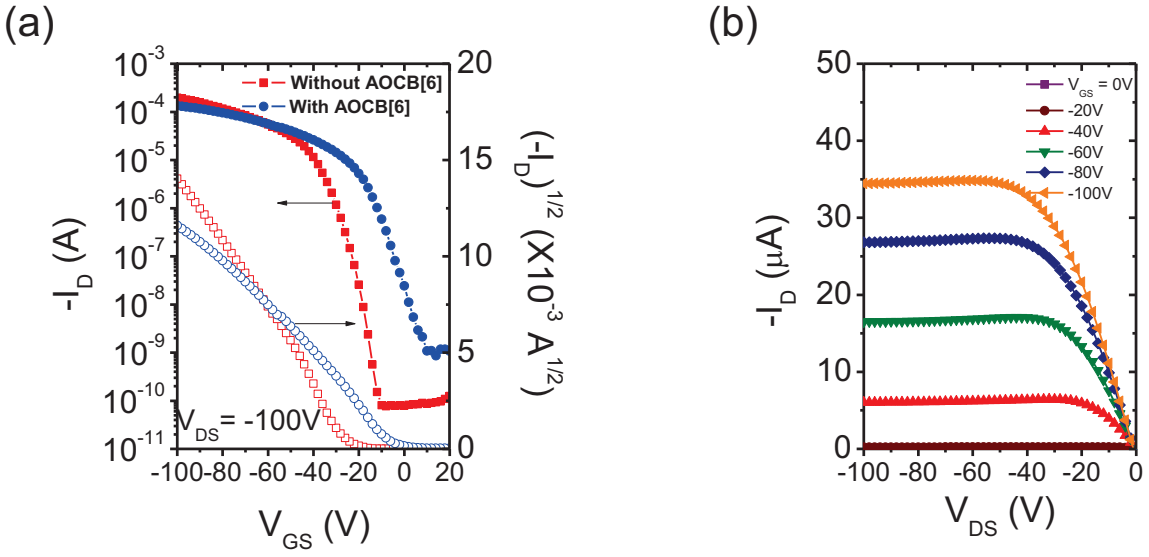

Figure 4.2. Current-voltage (*I*–*V*) characteristics of DDFTTF OFETs with and without AOCB[6]. a) Transfer characteristics for DDFTTF OFETs in *p*-channel operation mode and a source-drain electrode geometry of *W*/*L* = 180. b) Output characteristics for DDFTTF OFETs with AOCB[6].

ULSAN NATIONAL INSTITUTE OF
SCIENCE AND TECHNOLOGY

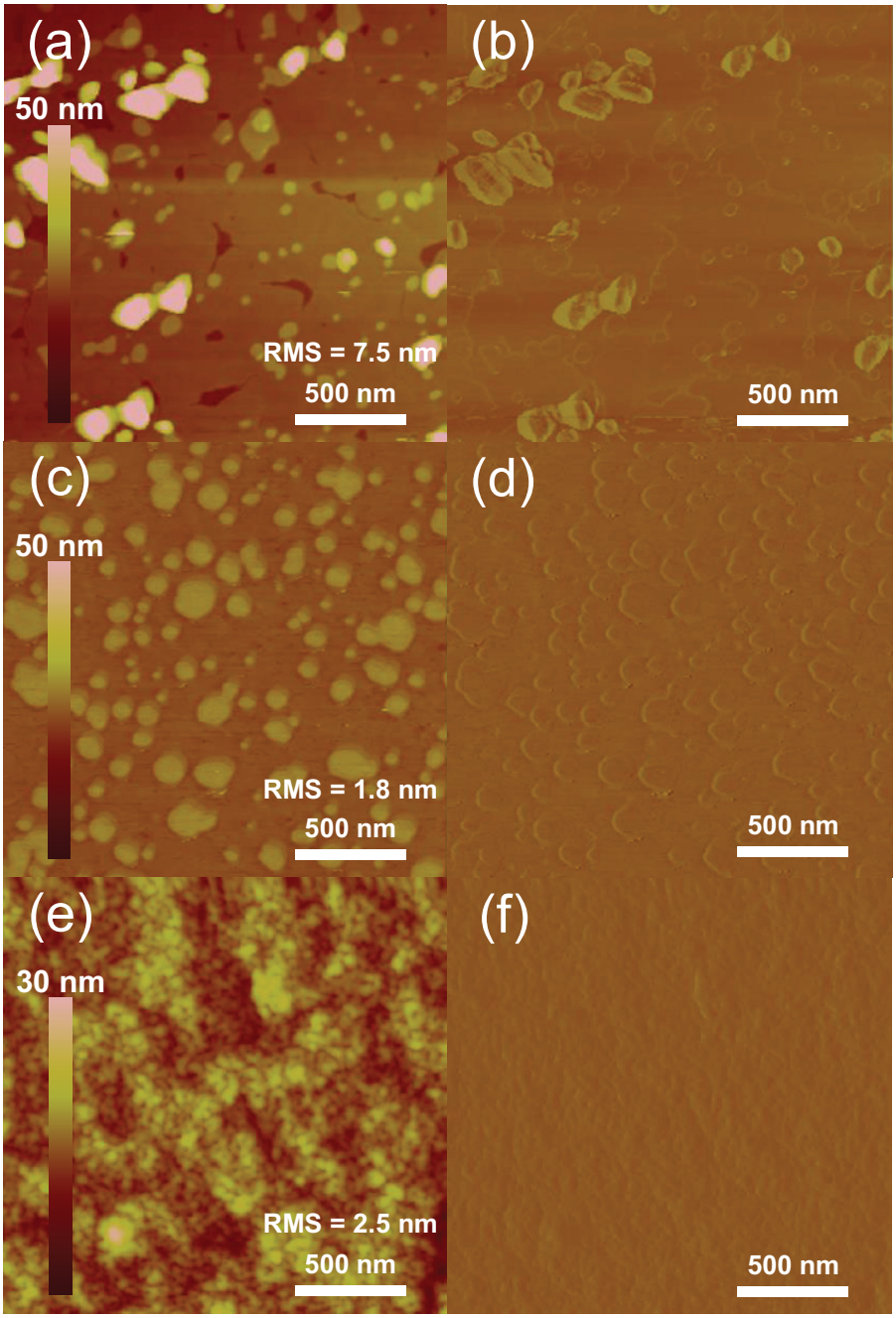

Figure 4.3. AFM images of OTS-modified SiO_2/Si substrates with a scan size of 2 μm × 2 μm; a), c) Height and b), d) phase images of DDFTTF film before and after thermal annealing at 150 °C for 30 min in nitrogen conditions. e) Height, f) phase images of AOCB[6]/DDFTTF film after annealing at 150 °C for 30 min under nitrogen conditions.

ULSAN NATIONAL INSTITUTE OF SCIENCE AND TECHNOLOGY

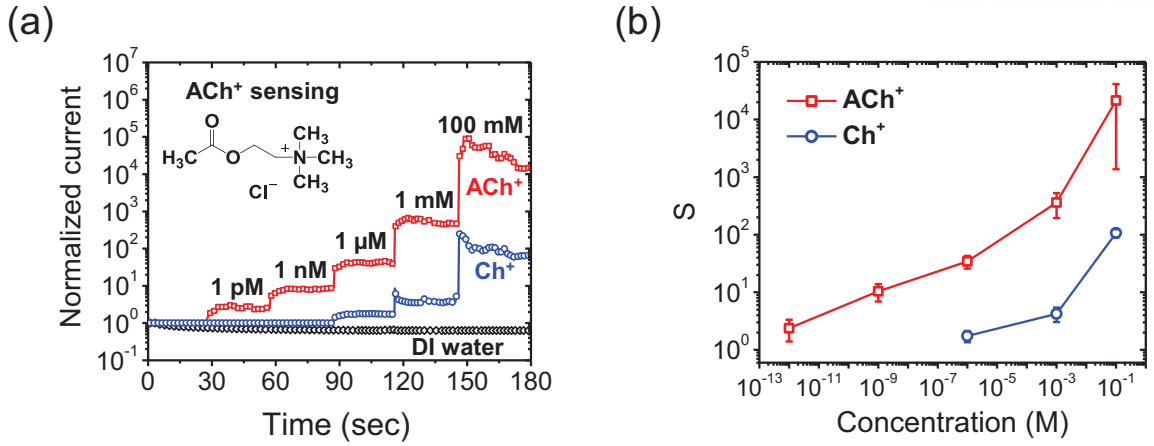

Figure 4.4. a) Real-time responses of DDFTTF OFET-based sensors with AOCB[6] toward various concentrations (1 pM – 100 mM) of ACh^+ and Ch^+, and pure DI water under typical operation conditions (V_{DS} = –2 V and V_{GS} = –60 V). b) Statistical comparisons of the sensing results for ACh^+ and Ch^+ (*S* indicates $I_D/I_{D\text{-}BASE}$).

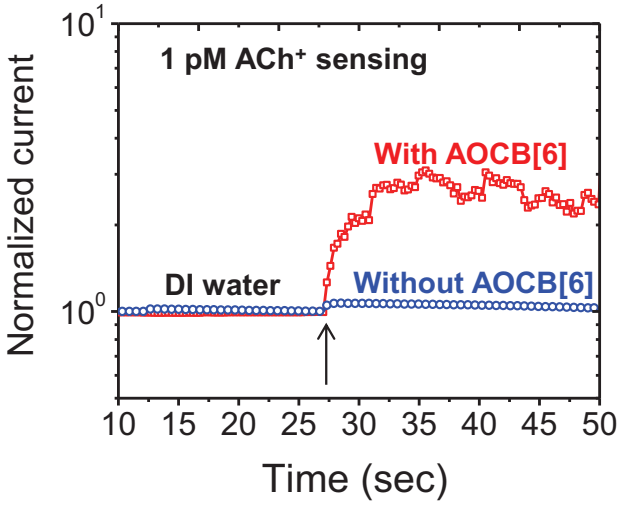

Figure 4.5. Comparison of responses of the DDFTTF OFET-based sensors with and without AOCB[6] toward 1 pM of ACh^+ at V_{DS} = –2 V and V_{GS} = –60 V.

ULSAN NATIONAL INSTITUTE OF SCIENCE AND TECHNOLOGY

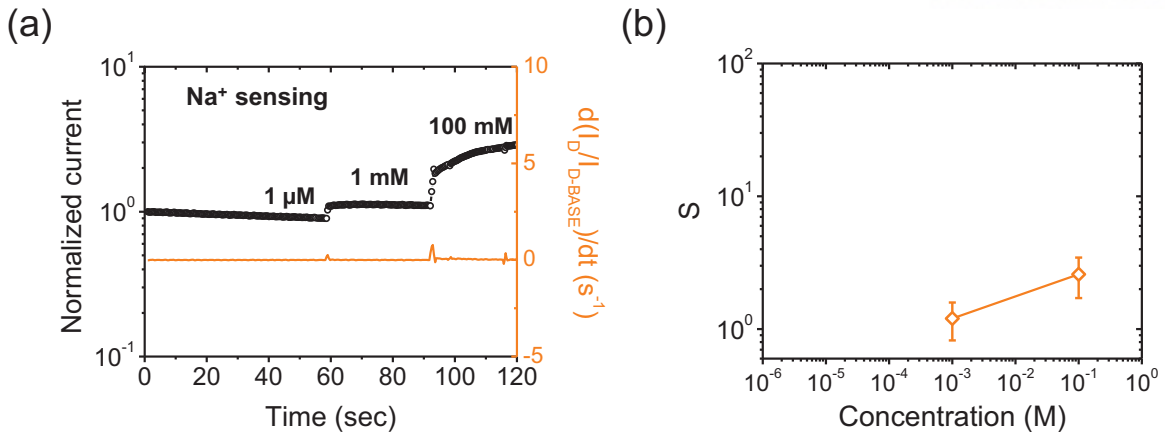

Figure 4.6. a) Real-time responses of DDFTTF OFET-based sensors with AOCB[6] toward various Na^+ concentrations (1 μM – 100 mM) at V_{DS} = –2 V and V_{GS} = –60 V. b) Statistical results for sensing Na^+ (S indicates $I_D/I_{D\text{-}BASE}$).

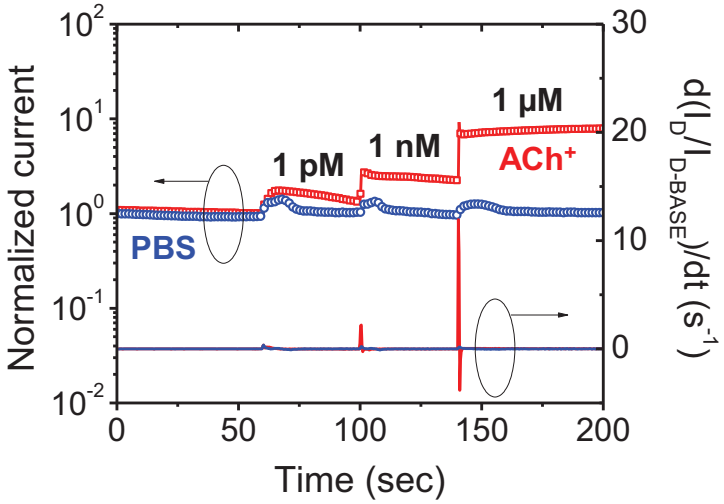

Figure 4.7. Real-time responses of the sensors with AOCB[6] toward pristine PBS and various concentrations (1 pM – 1 μM) of ACh^+ in a PBS solution at V_{DS} = –2 V and V_{GS} = –60 V. Acetylcholine chloride solutions were prepared in a PBS solution (pH 7.4, 0.01 M) containing sodium chloride (137 mM) and potassium chloride (2.7 mM).

ULSAN NATIONAL INSTITUTE OF SCIENCE AND TECHNOLOGY

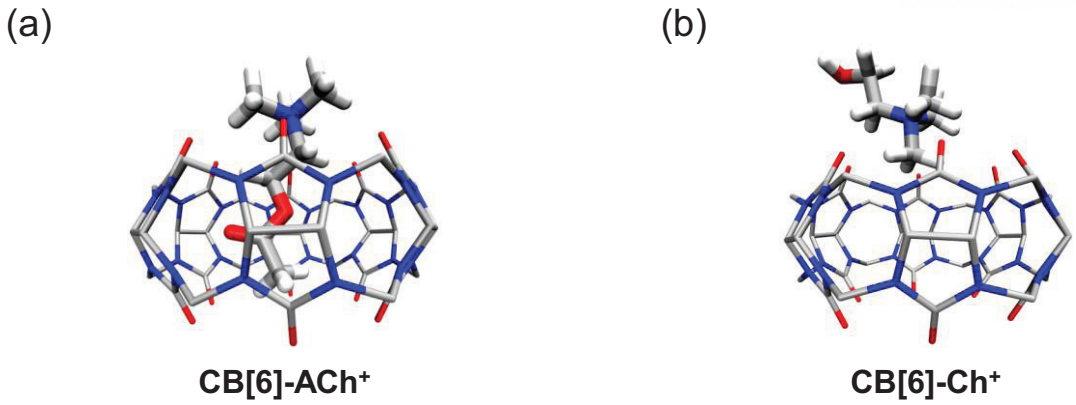

Figure 4.8. DFT optimized structures of the complexations of CB[6] and analytes: a) CB[6]-ACh^+ and b) CB[6]-Ch^+. Hydrogens of CB[6] are omitted for clarity. Color code: C, gray; O, red; N, blue; H, white.

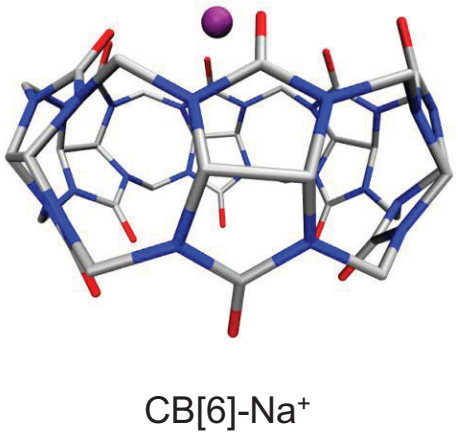

Figure 4.9. DFT optimized structures of the complexation of CB[6]-Na^+. Hydrogens of CB[6] are omitted for clarity. Color code: C, gray; O, red; N, blue; H, white; Na, purple.

ULSAN NATIONAL INSTITUTE OF SCIENCE AND TECHNOLOGY

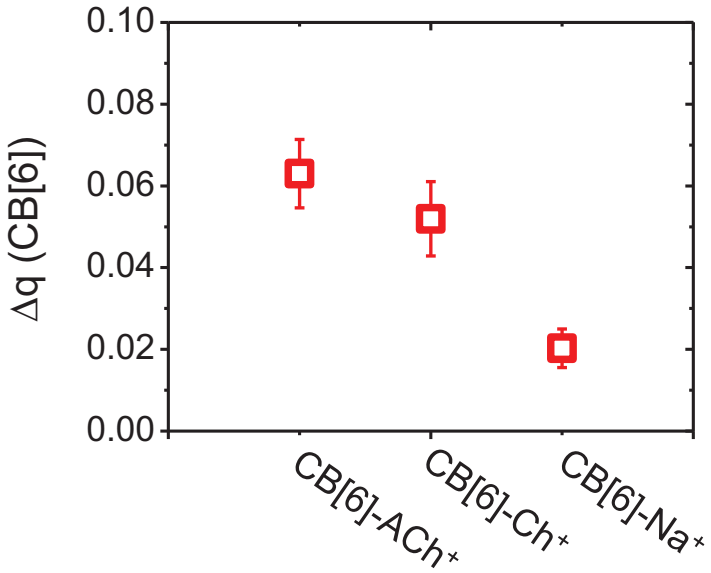

Figure 4.10. Charge changes on CB[6] after complexation with three guest molecules (ACh^+, Ch^+, and Na^+). For structures obtained from molecular dynamics simulations, charges of CB[6] are obtained from the natural population analysis at the M06-2X/6-31G(d) level.

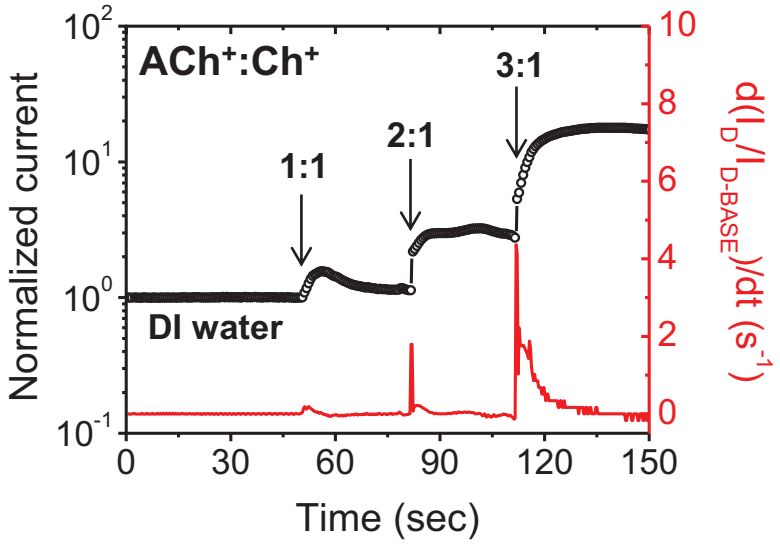

Figure 4.11. Signal changes of the sensors with AOCB[6] for the mixing systems of analytes containing both ACh^+ and Ch^+ at $V_{DS} = -2$ V and $V_{GS} = -60$ V. The red line indicates the rate of the signal change.

ULSAN NATIONAL INSTITUTE OF SCIENCE AND TECHNOLOGY

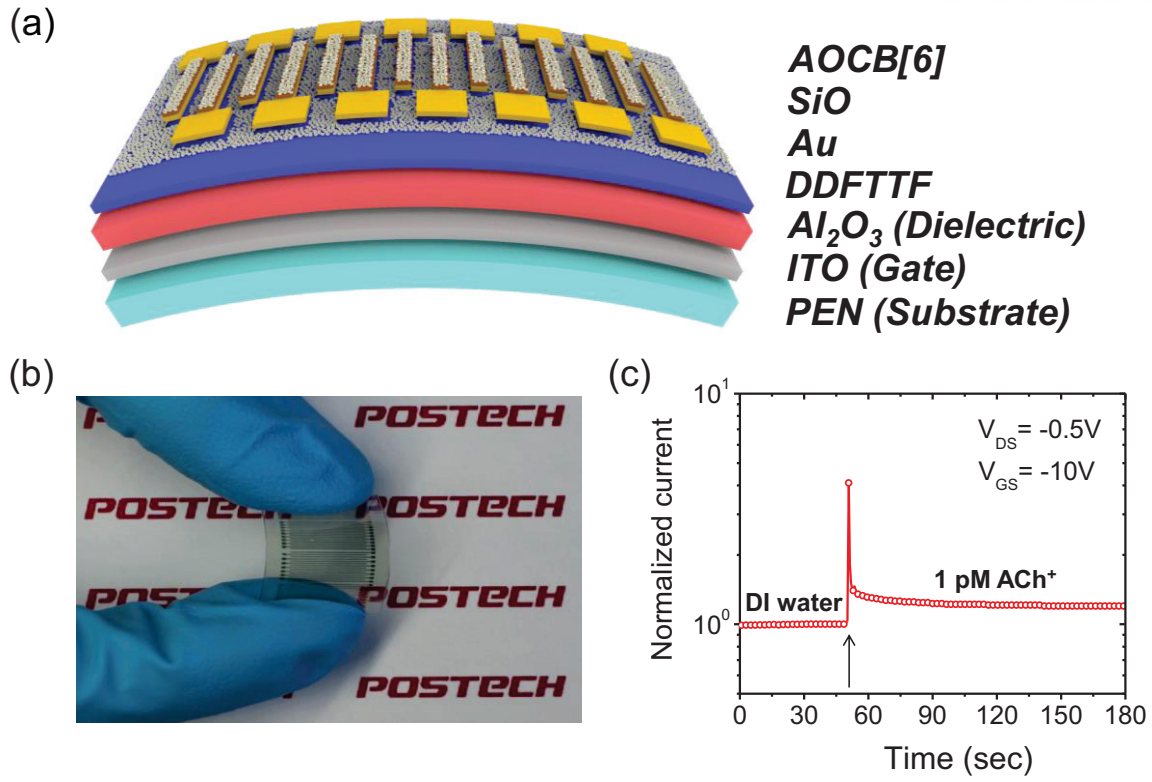

Figure 4.12. a) Schematic illustration of flexible DDFTTF OFET-based sensors with AOCB[6]. b) Photograph of a flexible sensor prepared with an Al_2O_3 gate dielectric on an ITO-coated PEN substrate. c) Real-time responses of the sensors with AOCB[6] toward 1 pM ACh^+ under a low-voltage operation condition.

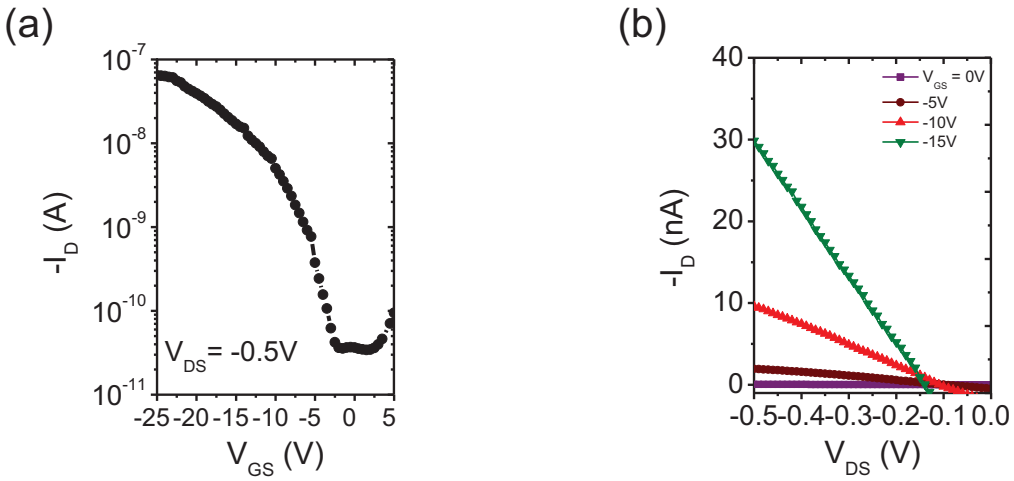

Figure 4.13. a) Transfer and b) output characteristics for flexible DDFTTF OFET-based sensors with AOCB[6] in *p*-channel operation mode.

ULSAN NATIONAL INSTITUTE OF SCIENCE AND TECHNOLOGY

Table 4.1. Summary of OFET performance obtained from DDFTTF thin films with and without AOCB[6] layers.

Functionalization	μ_{max} [b)] $[cm^2 V^{-1} s^{-1}]$	μ_{avg} [c)] $[cm^2 V^{-1} s^{-1}]$	I_{on}/I_{off}	V_{TH} [V]
N/F[a)]	0.076	0.053 (±0.038)[d)]	$>10^6$	–26.3
AOCB[6]	0.042	0.028 (±0.029)	$>10^5$	–5.6

[a)]The surface of DDFTTF thin films was not functionalized with AOCB[6]; [b)]The maximum and [c)]the average mobility measured from more than 10 OFET devices (L = 50 μm and W = 9000 μm); [d)]The standard deviation.

ULSAN NATIONAL INSTITUTE OF SCIENCE AND TECHNOLOGY

Chapter 5

Highly Sensitive Amphetamine-Type Stimulants Sensors Based on Surface-Engineered Organic Semiconductors

Abstract

One of the important social issues is the screening of amine-based illicit and designer drugs. To date, a large number of detectors for amphetamine-type stimulants (ATS) have used high-cost, custom-built test equipment. Here, highly sensitive organic field-effect transistor (OFET)-based sensors functionalized with synthetic supramolecular receptors are reported that can selectively detect amphetamine, a well-known illicit drug. A cucurbit[7]uril (CB[7]) derivative, which has good solubility in methanol but insoluble in water, has been solution-deposited as a selective sensing layer onto a water-stable *p*-channel semiconductor, 5,5′-bis-(7-dodecyl-9H-fl uoren-2-yl)-2,2′-bithiophene layer. The OFET-based sensors exhibit a detection limit down to 1 pM of amphetamine, which is six orders of magnitude lower than that of commercial ATS detectors. These experimental results show that specific synthetic receptor-engineered OFETs are promising platforms for high-performance ATS sensors on both conventional silicon and flexible substrates. Moreover, these OFET-based sensors show highly sensitive determinations of amphetamine in urine samples. Such superior sensing ability of the ATS sensor originates from the synergistic combination of a highly selective synthetic host molecule and a highly sensitive OFET device with high fidelity and with low cost as well as rapid on-site detection capability.

ULSAN NATIONAL INSTITUTE OF SCIENCE AND TECHNOLOGY

5.1. Introduction

Amphetamine-type stimulants (ATS), a group of drugs whose principal members include amphetamine and methamphetamine, have been widely used for medical use during several decades.[1] For example, it is known that amphetamine works on the brain's dopamine and norepinephrine neurotransmitter systems and therefore it is used for the treatment of attention deficit hyperactivity disorder (ADHD), narcolepsy, asthma, antidepressant, and so on.[1-4] However, frequent and long-term use of ATS may cause drug addiction and other serious side effects such as insomnia, hallucination, delusions, etc.[5, 6] Therefore, the use of ATS is restricted in many countries and strictly allowed only for medical purposes. Despite such regulations and controls, however, there has been a pronounced increase in the abuse of ATS worldwide. Especially, ATS rapidly replacing heroin and cocaine among drug addicts because it is cheap and easily accessible than other illicit drugs. Taken as pills, smoked, inhaled or injected, it is particularly attractive to young people because ATS produce a sense of high energy, a release of social inhibitions and feelings of cleverness, competence and power. Accordingly, abuse of ATS is of increasing concern to many countries and quickly growing problems, and more importantly, this is not an individual's problem but society's burning issue. Therefore, along with the strict regulation of the use of ATS by the government, there have been developed several methods to detect ATS including gas chromatography/mass spectrometry (GC/MS), liquid chromatography/mass spectrometry (LC/MS), immunoassay, and so on.[7-9] However, these analysis methods usually require long operation time, sophisticated experimental procedures and expensive equipment with well-trained professional operators. Thus, there is large demand for the development of easy, sensitive, selective, and rapid ATS detection method.

Compare with traditional analysis methods as mentioned above, supramolecular chemistry has not been applied for the detection of such drugs due to the lack of synthetic receptors which are suitable for specific recognition of ATS and related synthetic drugs.[10-15] Recently, tetraphosphonate cavitand receptor immobilized silicon microcantilevers were utilized for the detection of ATS and related synthetic drugs. Although this method provides some possibilities of supramolecular approaches can be used for the drug detection, there still are several things to be improved including detection limit of the drugs.

Sensors based on an organic field-effect transistor (OFET) show great promise for use in chemical and biological sensors, as they have many advantages including high sensitivity, low cost, simple processing, continuous monitoring, etc.[16-21] As pristine OFET-based sensors often exhibit low selectivity due to the lack of recognition unit, therefore, highly selective detection with OFET-based sensors often requires chemical modification of specific receptors on a device surface to capture target analyte. Recently, we have reported a highly selective and sensitive acetylcholine sensor based on an OFET device.[22] In this sensor, the surface of an OFET was functionalized with an acetylcholine

ULSAN NATIONAL INSTITUTE OF SCIENCE AND TECHNOLOGY

specific synthetic host molecule, a cucurbit[6]uril (CB[6]) derivative, and the sensor showed a detection limit for acetylcholine down to 1 pM, which was two orders of magnitude lower than that of acetylcholinesterase-based biosensors. Such superior sensing ability of the sensor is originated from the synergistic combination of a highly selective synthetic host molecule and a highly sensitive OFET device. This success prompts us to develop portable ATS sensors using other CB homologues with high fidelity and sensitivity with low cost as well as on-site detection capability (**Figure 5.1**).[23-27] Herein, we report a cucurbit[7]uril (CB[7]) derivative functionalized OFET device sensor for ATS which shows highly sensitive and selective sensing for ATS in water and even both in physiological buffer and urine. In addition, here we also report a flexible OFET sensor with a polymer substrate.

5.2. Experimental Section

Materials: MultihydroxyCB[7] (250 mg, 0.025 mmol) was dissolved in anhydrous DMSO (100 mL) and sonicated for 0.5 h, and sodium hydride (0.68 g, 18 eq.) was added to the solution. The mixture was stirred for 12 hours under argon atmosphere. Then, 1-Bromo-4-phenylbutane (2.0 g, 18 eq.) was slowly added to the mixture and the mixture was stirred for 12 hours. After completion of the reaction, large amount of ether was added to the solution then the solution was stirred and precipitate was washed with ether two more times. After decanting ether layer, methanol was added to the beaker and add excess amount of ether to get precipitates. The solution was centrifuged and the precipitate was washed with ether twice. After decanting ether, yellowish precipitate was collected and dried in vacuum. MS (MALDI-TOF): m/z 1803.76 $[M4+MeOH+H]^+$ (exact mass: 1803.73), 1952.27 $[M5+MeOH+H]^+$ (exact mass: 1951.82), 2101.01 $[M6+MeOH+H]^+$ (exact mass: 2099.90). Synthesis of CB[7] derivatives was performed by Dr. Ilha Hwang and Prof. Kimoon Kim, POSTECH.

DDFTTF-Based OFET Sensor Fabrication: OFET-based sensors were fabricated with a heavily n-doped silicon wafer (<0.004 Ω cm) covered with a thermally grown 300 nm-thick oxide layer (SiO_2, C_g = 10 nF cm^{-2}). The SiO_2/Si wafers were cleaned with Piranha (a mixture of H_2SO_4 and H_2O_2 by volume ratio of 7:3) solution, followed by UV-ozone treatment. The SiO_2 surface was treated with OTS in solution phase as self-assembled monolayer according to previously reported method.[22] The OTS solution (3 mM in trichloroethylene) was spin-coated onto the wafer. The wafer was exposed to NH_4OH vapor in a vacuum desiccator at room temperature overnight, followed by sequential washing, and drying with nitrogen blowing. The contact angle (droplet of DI water) on the hydrophobic OTS-treated wafer was ~110°. The DDFTTF thin films (~15 nm nominal thickness) were thermally deposited onto the OTS-treated SiO_2/Si wafer at 0.1–0.2 Å s^{-1} under a base pressure below 5.0×10^{-6} torr. During the evaporation, the optimal substrate temperature for DDFTTF deposition was 105 °C. The films were annealed at 150 °C for 30 min in a nitrogen atmosphere. Gold contacts (~40 nm thickness) were

ULSAN NATIONAL INSTITUTE OF SCIENCE AND TECHNOLOGY

thermally evaporated onto the DDFTTF films to form source and drain with a channel width (W) and a channel length (L) of 9000 μm and 50 μm, respectively. A silicon monoxide (SiO, ~20 nm thickness) layer was thermally deposited onto the electrodes except for the gold contacts. The SiO layer was used as a passivation layer for the sensor operation in liquid solutions. Then, the solution-processable AOCB[7] were dissolved in methanol (~5 mg mL^{-1}) and the film was spin-coated onto the underlying film at 7000 rpm for 30 s. The films were dried in a vacuum oven at 60 °C overnight and annealed at 150 °C for 30 min to remove the residual solvent.

Electrical Measurement: The electrical performance and sensing tests of OFETs were measured using a Keithley 4200 semiconductor parametric analyzer. The field-effect mobility (μ_{FET}) was calculated in the saturated regime using the following equation:

$$I_D = \frac{W}{2L}\mu_{FET}C_g\left(V_{GS} - V_{TH}\right)^2 \quad (1)$$

where I_D is the drain current, C_g is the capacitance per unit area of the gate dielectric layer, and V_{GS} and V_{TH} are the gate voltage and threshold voltage, respectively.

5.3. Results and Discussion

5.3.1. Synthesis and Characterization of CB[7]

The stable 1:1 inclusion complex formation and strong interactions between ATS and CB[7] were confirmed by NMR and mass spectrometries. Firstly, ^{1}H NMR spectra of amphetamine hydrochloride (**1**) bound to CB[7] are shown in **Figure 5.2**. As shown in **Figure 5.2a**, ^{1}H NMR spectroscopy showed drastic changes in proton signals of ATS upon complexation with CB[7]. For example, when a freshly dissolved **1** in D_2O was treated with 1 equiv. of CB[7], most of the proton signals of **1** were upfield shifted and only the methyl protons in *N*-methyl secondary amines were downfield shifted. The cavity and carbonyl-laced portals of CB[7] mediate encapsulation of **1** through hydrophobic and ion-dipole interactions in water. For the cases of methamphetamine (**2**) also showed similar results as in case of **1** (See **Figure 5.3a**). In addition to NMR analyses, quantitative measurements of the binding affinities between CB[7] and ATS were performed by isothermal titration calorimetry (ITC). ITC analysis revealed that CB[7] has excellent affinities for all the three ATS in Figure 1 with a 1:1 stoichiometry ($K_a = 10^5 - 10^6$ M^{-1}). For example, The binding constant of **1** toward CB[7] was $(1.2 \pm 0.1) \times 10^6$ M^{-1}. The formation of the inclusion complex is enthalpy-driven ($\Delta H° = -41.5 \pm 0.2$ kJ/mol), where the unfavorable entropic contribution ($T\Delta S° = -6.8 \pm 0.3$ kJ/mol) is apparently compensated by the large favourable enthalpic gain, as a result of the hydrophobic interactions between the phenyl ring of the guest and the inner wall of the host cavity as well as strong ion-dipole interactions between ammonium groups of the guest and carbonyl-laced portals of the host. Finally, the stable inclusion complex

ULSAN NATIONAL INSTITUTE OF SCIENCE AND TECHNOLOGY

formation is also confirmed by single crystal X-ray analysis. Single crystals of **1** and **2** complexed with CB[7] suitable for X-ray work were obtained from water by vapor diffusion, and the crystal structures of the complexes are shown in **Figure 5.2b** and **Figure 5.3b**. In both complexes, the benzyl residues of guests encapsulated deep inside of the CB[7] cavity exhibit complete inclusion of the guests while the ammonium group positioned near the carbonyl rims of CB[7]. The main planes passing through benzene ring of **1** and **2** are tilted by 55.2°and 45.0°, respectively, with reference to the main sevenfold symmetry axis of CB[7]. Such orientations of **1** and **2** lead to ion-dipole interactions between CB[7] and ammonium groups (shortest N•••O distances: 2.958 (11) Å, 2.772 (5) Å for **1**@CB[7] and **2**@CB[7], respectively). CB[7] derivatives (allyloxyCB[7] (**5**)) which have good solubility in methanol and not soluble in water. Therefore, the CB[7] film can easily be deposited using the spin coating method with a methanol solution of **5** on top of the DDFTTF semiconducting layer. The recognition property of the functionalized CB[7] is basically the same as of the CB[7] itself and functionalization of outer wall of the receptor molecule only affect on the solubility of the molecule and processability for the sensor device fabrication. Therefore the deposited film acts as a stable and selective sensing layer for ATS in the aqueous phase.

5.3.2. Fabrication of OFETs and *I-V* Characterizations

The bottom-gate/top-contact transistor-based sensors were fabricated to demonstrate highly sensitive chemical detection, using allyloxyCB[7] (AOCB[7])-functionalized semiconductor layer. A *p*-channel, 5,5′-bis-(7-dodecyl-9H-fl uoren-2-yl)-2,2′-bithiophene DDFTTF thin film (~15 nm thickness) was deposited with thermal evaporation onto *n*-octadecyltrimethoxysilane (OTS)-treated SiO_2/Si substrates as the active layer for the OFET type-sensor device due to its relatively high mobility and stability in water.[28] The gold source and drain electrodes (~40 nm thickness) in the channel area were covered with a SiO passivation layer (~20 nm thickness) as previously reported[22] (see also "Experimental Section" above). A selective receptor, AOCB[7] solution (~5 mg mL^{-1}), which was dissolved in methanol, was spin-coated on top of the semiconductor. The corresponding device structure is shown in **Figure 5.4a**. The electrical characteristics of OFETs with and without AOCB[7] were measured in the saturation regime (**Figure 5.4b**). The linear regime operation also showed obvious field-effect behaviors (**Figure 5.4c**). The DDFTTF OFETs with AOCB[7] had a relatively high field-effect mobility (μ_{FET}) of 0.02 $cm^2\ V^{-1}\ s^{-1}$, with an on/off current ratio (I_{on}/I_{off}) of more than 10^5 in ambient conditions. Although high mobility is not an essential requirement for sensing applications, it can facilitate a superior signal amplification and high response speed.[29]

5.3.3. Microstructural Analysis of Thin-Film

We conducted a tapping-mode atomic force microscopy (AFM) investigation, to investigate the surface morphological characteristics of DDFTTF films and AOCB[7]-functionalized DDFTTF films before and after amphetamine sensing. The thermal evaporation of 30 nm of DDFTTF resulted in highly

ULSAN NATIONAL INSTITUTE OF SCIENCE AND TECHNOLOGY

planar surfaces over large areas as shown in **Figure 5.5a**,**b**. The annealed DDFTTF thin films showed the polycrystalline grains and distinct grain boundaries with a root-mean-square (RMS) roughness of 1.7 nm. The spin-coated AOCB[7] layer covered the DDFTTF layer fully and uniformly (**Figure 5.5c** and **5.5d**), which were crucial for highly sensitive sensor fabrication. The cross-sectional AFM analysis revealed that the thickness of the AOCB[7] layer was 3.7 nm. As can be seen in **Figure 5.5e**,**f**, the surface of AOCB[7]-functionalized films clearly showed crumpling morphology after sensing tests. Moreover, the AOCB[7] aggregation morphology in DDFTTF thin films existed mainly due to the binding interaction between AOCB[7] host and amphetamine. However, this results of the AFM analysis showed that the surface of the organic active layer of the sensor was maintained after direct exposure to the liquid-phase analytes.

5.3.4. OFET-Based Sensors

A sensing system for the detection of liquid analytes was prepared by placing a polydimethylsiloxane (PDMS) mold container onto the sensor device. Sensing experiments were performed under ambient conditions by monitoring the output current as a function of time. The V_{DS} and V_{GS} were fixed at -2 V and -60 V, respectively. Prior to detecting the analytes, a baseline current was estimated with deionized (DI) water. After stabilizing the output current, solutions (~15 μL) containing analytes were injected into the mounted PDMS container. The sensing signals were normalized by dividing the drain current by the baseline current ($I_D/I_{D\text{-}BASE}$). In a control experiment, biogenic amines, phenylethylamine (PEA) exposure can be measured via binding interaction at the target site. The sensors with AOCB[7] showed the much higher drain current change for liquid-phase PEA compared to the sensors with AOCB[6] (**Figure 5.6a**). CB homologues and derivatives, their varying cavity and portal sizes can expand the scope and lead to tunable molecular recognition properties from those of CB[6]. CB[7] has the mean diameter of the internal cavity ~7.3 Å, which forms complexes easily with larger guest molecules that are not included in CB[6].[23, 26] This finding indicates that the introduction of the AOCB[7] layer significantly enhances the sensitivity of the sensors through selective binding of bulky amines, such as PEA. We also monitored the change of drain current toward PEA at different concentrations (**Figure 5.6b**). The signal changes of the sensors increased with an increasing concentration of PEA. However, the sensors toward 1 nM PEA showed negative sensing behaviors, in which the drain current decreased after injection of the analytes. The complexation between CB[7] and PEA has a lower binding constant of $(8.6 \pm 0.7) \times 10^4$ M^{-1} from ITC analysis, which supports that AOCB[7] forms a weak host-guest complex with PEA. Thus, the sensors for PEA exhibited the detectable signals at concentrations higher than 1 nM.

The real-time liquid-phase sensing responses of sensors functionalized with AOCB[7] toward amphetamine, which is a known illicit drug, are shown in **Figure 5.7a**. The DDFTTF OFET-based sensor showed enhanced drain current after injection of liquid-phase analytes. In *p*-channel OFET-

ULSAN NATIONAL INSTITUTE OF SCIENCE AND TECHNOLOGY

based sensors, hole charge-transport may increase after the absorption of amine receptors, amphetamine because the electron-withdrawing effects into the channel region. This can be induced by charge-dipole interactions between the carbonyl group of AOCB[7] and the positively charged ammonium group of amine analytes. Surprisingly, the detection limit (1 pM) of the DDFTTF sensors with AOCB[7] toward amphetamine was six orders of magnitude lower than that (~μM) of the commercial detectors. **Figure 5.7b** shows the statistical data for the sensing results of amphetamine. The sensing signals of the sensors increased with an increasing concentration of amphetamine. However, its an excellent linearity of its response was maintained only at very low analyte concentrations, and the sensors possess a nonlinear sensitivity at high concentrations of analyte. Detection lineariry is directly affected by specific absorption rates of the analyte. As the solute concentration increases, the analyte molecules may begin to interact with each other, through intermolecular attractive forces. Such interactions may result in the nonlinear response at high analyte concentrations. We also monitored changes in the drain current of the sensors with and without the AOCB[7] layer, while the devices were exposed to 1 pM of amphetamine (**Figure 5.8**). The sensors with AOCB[7] showed much higher sensitivity for amphetamine compared to the sensors without AOCB[7]. These results indicate that introduction of the AOCB[7] layer significantly improves the sensitivity of the sensors through selective binding of amphetamine on the device surface.

Furthermore, **Figure 5.9a** shows that the direct-sensing behaviors of methamphetamine, which is also known as amphetamine-like popular drugs. The positive sensing behaviors, in which the drain current is enhanced after binding events with the analytes, were also observed for methamphetamine. The AOCB[7]-functionalized sensors could also detect methamphetamine, although they exhibited relatively lower sensitivity compared to sensors for amphetamine due to the effects of bulky analytes. For complexation between CB[7] and methamphetamine, the enhanced electron donating ability of the methyl group of methamphetamine may interrupt the strong charge-dipole interactions between CB[7] and the positively charged ammonium group of methamphetamine. **Figure 5.9b** shows the statistical data for the sensitivity of the methamphetamine sensors.

The proposed sensor in this study was tested reusability of the sensor for practical applications. The transfer curves of DDFTTF OFETs with AOCB[7] were measured in ambient air before and after sensing for amphetamine, and after re-thermal annealing (**Figure 5.10a**). After a sensing test, the off-current increased due to the doping effect of the analytes and oxygen.[22, 30] In most of the OFET-based sensors, the active semiconductor layers are exposed to the target analytes, in which the channel currents can be changed by charge doping or de-doping from the analytes. After sensing of amphetamine, we thermally re-annealed the devices at 150 °C for one time only in nitrogen conditions. The annealing process for the reusable, robust sensors shows that the increased in off-current completely recovery to the original current value. The morphological analysis has also been performed with AFM analysis

ULSAN NATIONAL INSTITUTE OF SCIENCE AND TECHNOLOGY

(**Figure 5.10b**). The AFM image of AOCB[7]-functionalized DDFTTF film after re-annealing showed relatively uniform surface with reducing AOCB[7] aggregation. The results clearly support good reusability of AOCB[7]-functionalized DDFTTF films in liquid-phase analytes, through strong binding of the sensing layer to the surface of the organic active layer.

For our real biological sensing platform, we included the sensors toward phosphate-buffered saline (PBS) systems (pH 7.4, 0.01 M), containing sodium chloride (137×10^{-3} M) and potassium chloride (2.7×10^{-3} M) (**Figure 5.11**). The sensing tests were prepared in the PBS baseline estimation and in PBS solvent. The sensor with AOCB[7] exhibited the minimal changes in the output current when the device was exposed to pristine PBS. In the presence of the PBS solution (under a physiological condition), the OFET sensors showed remarkably enhanced signal intensities toward various amphetamine concentrations (1 pM – 1 μM). However, these sensors exhibited the lower sensitivity compared with our previous results in DI water due to the relatively high binding affinity between AOCB[7] and the interfering cations (Na^+ and K^+).

When people take specific drugs, drugs or their metabolites can typically eliminate or excrete drug matter from the body. Urine drug testing used by police has been the most common method for drug-detection analysis because of ease of sampling. For drug sensors with low-cost and high practicality, we have performed additional experiments for OFET-based amphetamine sensors by using a artificial urine, instead of DI water. The AOCB[7]-functionalized OFET sensors exhibited minimal sensing signals after continuous injections of the only artificial urine solution (**Figure 5.12a**). Amphetamine solutions were prepared in the urine solution, and then its dilution on concentrations was conducted with DI water. Prior to injection of the analytes, baseline tests were performed using artificial urine. The sensors could also detect amphetamine with the detection limit down to 0.2 pM in the artificial urine samples even after the post dilution process, as shown in **Figure 5.12b**. The ATS sensor herein can be applied to sub-picoM concentration of amphetamine determinations in urine samples.

The OFET-based sensors are also of vital importance for many artificial intelligent and health-care applications. In particular, the development of wearable sensor platform based on flexible devices is underway for use in health-care applications. In **Figure 5.13a**, we also fabricated flexible drug sensors using an indium tin oxide (ITO)-coated polyethylene naphthalate (PEN) substrate and an aluminum oxide (Al_2O_3) transparent gate dielectric. A 100 nm-thick Al_2O_3 dielectric layer was deposited on the PET substrate via a radio frequency (RF) magnetron sputtering technique, and a photograph of the fabricated flexible sensor is shown in **Figure 5.13b**. The transfer and output characteristics of the DDFTTF OFET-based sensor with AOCB[7] are investigated, which exhibited ample electrical performance (**Figure 5.14a** and **5.14b**). The results of the sensing experiments for amphetamine exhibited performances similar to SiO_2 dielectric-based sensors. Using these AOCB[7] decorated flexible sensor platform, the selective detection of amphetamine with a concentration of 1 pM has been

ULSAN NATIONAL INSTITUTE OF SCIENCE AND TECHNOLOGY

also realized under low-voltage operation conditions (V_{DS} = −1.5 V and V_{GS} = −10 V). These results describe the first demonstration of rapid ATS sensing with supramolecular chemistry using synthetic receptor-functionalized flexible OFET-type sensors.

5.4. Conclusion

In summary, the results reported herein demonstrate that highly sensitive and portable OFET-based ATS sensors without high-cost equipment. The molecular recognition at the interface for amphetamine is achieved with high fidelity and with low cost by supramolecularly functionalized with organic semiconductors. AOCB[7], a synthetic receptor molecule which has good solubility in methanol and not soluble in water, could effectively be deposited on top of the water-stable DDFTTF semiconducting layer. The first ATS sensors with specific synthetic receptor-engineered OFET-platform are demonstrated on both rigid substrate (SiO_2/Si) and flexible plastics (polyethylene terephthalate PET) substrates. These sensors in DI water and even in physiological buffer system showed a detection limit for amphetamine down to 1 pM. Furthermore, the sensors could detect amphetamine with high sensitivity and selectivity even in the presence of artificial urine, due to the higher binding affinity of AOCB[7] toward amphetamine compared to urine. Such superior sensing ability of the ATS sensor is originated from the synergistic combination of a highly selective synthetic host molecule and a highly sensitive OFET device with high fidelity and with low cost as well as on-site detection capability. This work also provides a viable methodology for the fabrication of OFET-based sensors that can detect the drugs directly in real street samples.

ULSAN NATIONAL INSTITUTE OF SCIENCE AND TECHNOLOGY

5.5. References

[1] Elia J.; Ambrosini P. J., Rapoport J. L., *N. Engl. J. Med.* **1999**, *340*, 780-788.
[2] Rothman R. B.; Baumann M. H.; Dersch C. M.; Romero D. V.; Rice K. C.; Carroll F. I., Partilla J. S., *Synapse* **2001**, *39*, 32-41.
[3] Winstanley C. A.; Eagle D. M., Robbins T. W., *Clin. Psych. Review* **2006**, *26*, 379-395.
[4] Heal D. J.; Smith S. L.; Gosden J., Nutt D. J., *J. Psychopharmacol.* **2013**, *27*, 479-496.
[5] Berman S. M.; Kuczenski R.; McCracken J. T., London E. D., *Mol. Psychiatry.* **2008**, *14*, 123-142.
[6] Chen H.; Wu J.; Zhang J., Hashimoto K., *Curr. Drug Abuse. Rev.* **2010**, *3*, 222-238.
[7] Marais A. A. S., Laurens J. B., *Forensic Sci. Int.* **2009**, *183*, 78-86.
[8] Deventer K.; Van Eenoo P., Delbeke F. T., *Rapid Commun. Mass Spectrom.* **2006**, *20*, 877-882.
[9] Negrusz A.; Moore C.; Deitermann D.; Lewis D.; Kaleciak K.; Kronstrand R.; Feeley B., Niedbala R. S., *J. Anal. Toxicol.* **1999**, *23*, 429-435.
[10] Lavigne J. J., Anslyn E. V., *Angew. Chem. Int. Ed.* **2001**, *40*, 3118-3130.
[11] Anslyn E. V., *J. Org. Chem.* **2007**, *72*, 687-699.
[12] Pinalli R., Dalcanale E., *Acc. Chem. Res.* **2013**, *46*, 399-411.
[13] Anderson M.; Wilcox K.; Guericke M.; Chu H.; Wilson M. V.; Wilson E.; Lucas K., Holmes A. E., *Chirality* **2010**, *22*, 398-402.
[14] Minami T.; Esipenko N. A.; Akdeniz A.; Zhang B.; Isaacs L., Anzenbacher P., *J. Am. Chem. Soc.* **2013**, *135*, 15238-15243.
[15] Biavardi E.; Federici S.; Tudisco C.; Menozzi D.; Massera C.; Sottini A.; Condorelli G. G.; Bergese P., Dalcanale E., *Angew. Chem. Int. Ed.* **2014**, *53*, 9183-9188.
[16] Janata J., Josowicz M., *Nat. Mater.* **2003**, *2*, 19-24.
[17] Hammock M. L.; Knopfmacher O.; Naab B. D.; Tok J. B. H., Bao Z., *ACS Nano* **2013**, *7*, 3970-3980.
[18] Roberts M. E.; Sokolov A. N., Bao Z., *J. Mater. Chem.* **2009**, *19*, 3351-3363.
[19] Lin P., Yan F., *Adv. Mater.* **2012**, *24*, 34-51.
[20] Yu H.; Bao Z., Oh J. H., *Adv. Funct. Mater.* **2013**, *23*, 629-639.
[21] Yun M.; Sharma A.; Fuentes-Hernandez C.; Hwang D. K.; Dindar A.; Singh S.; Choi S., Kippelen B., *ACS Appl. Mater. Interfaces* **2014**, *6*, 1616-1622.
[22] Jang M.; Kim H.; Lee S.; Kim H. W.; Khedkar J. K.; Rhee Y. M.; Hwang I.; Kim K., Oh J. H., *Adv. Funct. Mater.* **2015**, *25*, 4882-4888.
[23] Lee J. W.; Samal S.; Selvapalam N.; Kim H.-J., Kim K., *Acc. Chem. Res.* **2003**, *36*, 621-630.
[24] Lagona J.; Mukhopadhyay P.; Chakrabarti S., Isaacs L., *Angew. Chem. Int. Ed.* **2005**, *44*, 4844-4870.
[25] Masson E.; Ling X.; Joseph R.; Kyeremeh-Mensah L., Lu X., *RSC Adv.* **2012**, *2*, 1213-1247.
[26] Assaf K. I., Nau W. M., *Chem. Soc. Rev.* **2015**, *44*, 394-418.
[27] Barrow S. J.; Kasera S.; Rowland M. J.; del Barrio J., Scherman O. A., *Chem. Rev.* **2015**, *115*, 12320-12406.
[28] Roberts M. E.; Mannsfeld S. C. B.; Queraltó N.; Reese C.; Locklin J.; Knoll W., Bao Z., *Proc. Natl. Acad. Sci. U.S.A.* **2008**, *105*, 12134-12139.
[29] Zang Y.; Huang D.; Di C.-a., Zhu D., *Adv. Mater.* **2016**, *28*, 4549-4555.
[30] Bao Z., *Adv. Mater.* **2000**, *12*, 227-230.

ULSAN NATIONAL INSTITUTE OF SCIENCE AND TECHNOLOGY

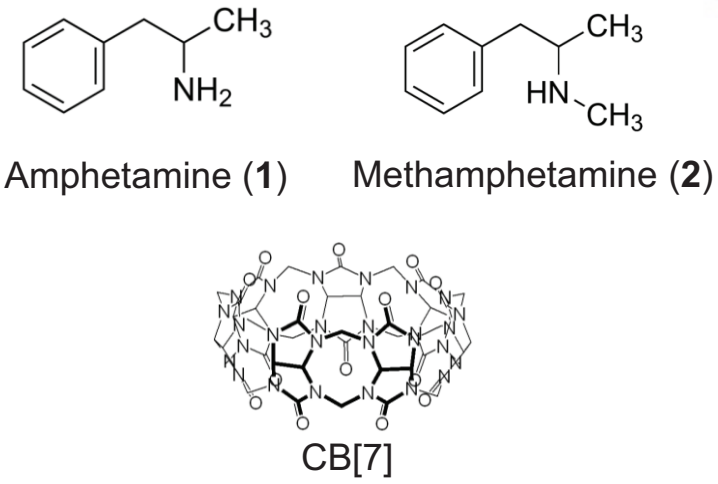

Figure 5.1. Chemical structures of the ATS tested and receptor CB[7].

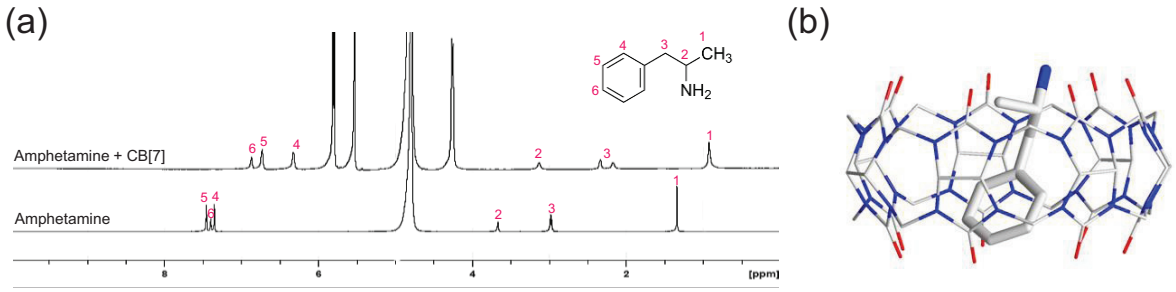

Figure 5.2. a) ^{1}H-NMR spectra of complexation of **1** and CB[7] in D_2O. (b) X-ray structure of **1**@CB[7].

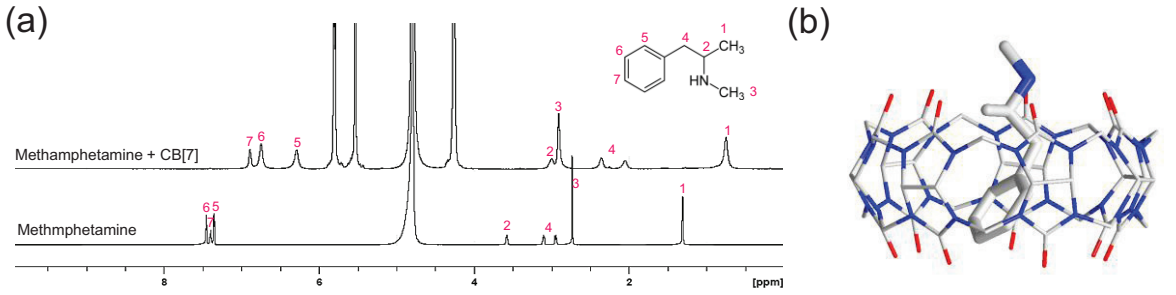

Figure 5.3. a) ^{1}H-NMR spectra of complexation of **2** and CB[7] in D_2O. (b) X-ray structure of **2**@CB[7].

ULSAN NATIONAL INSTITUTE OF SCIENCE AND TECHNOLOGY

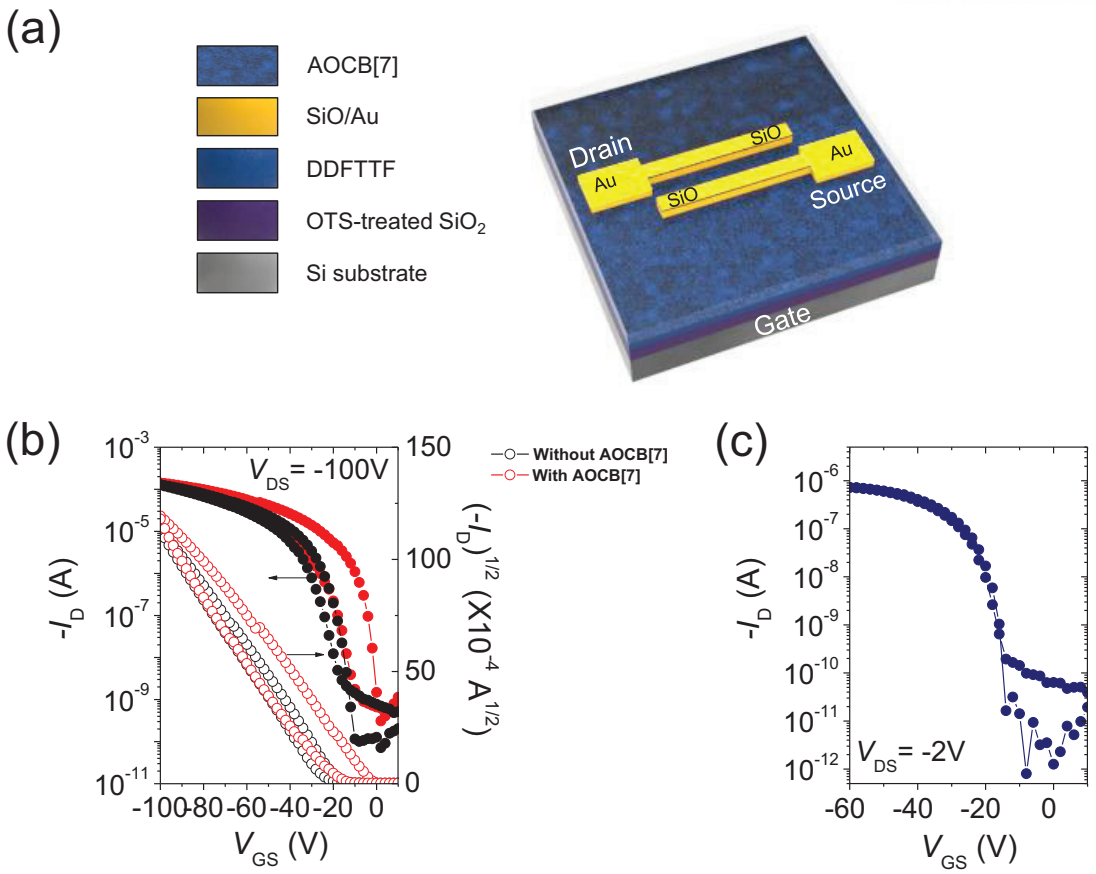

Figure 5.4. a) Schematic illustration of the top-contact OFET-based sensors with AOCB[7]. b) Transfer characteristics of DDFTTF OFETs with and without AOCB[7] in *p*-channel operation mode. c) Transfer characteristics for DDFTTF OFETs with AOCB[7] under low-voltage operation.

ULSAN NATIONAL INSTITUTE OF SCIENCE AND TECHNOLOGY

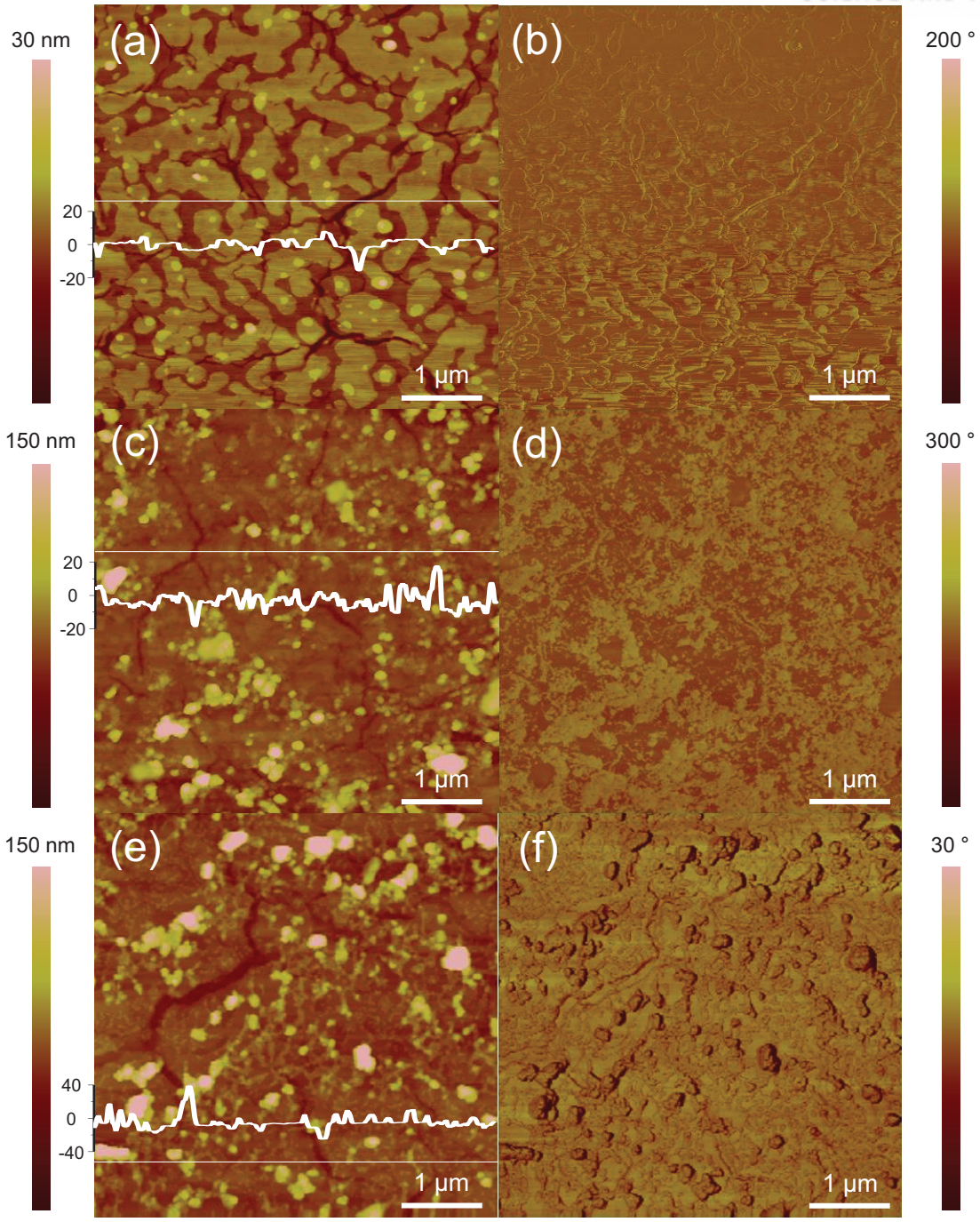

Figure 5.5. AFM images of the active layers of DDFTTF OFET-based sensors; a) Height and b) phase images of DDFTTF film after thermal annealing at 150 °C for 30 min in nitrogen conditions. c,e) Height and d,f) phase images of the surface of the sensors with AOCB[7] film before and after sensing tests for amphetamine, respectively.

ULSAN NATIONAL INSTITUTE OF SCIENCE AND TECHNOLOGY

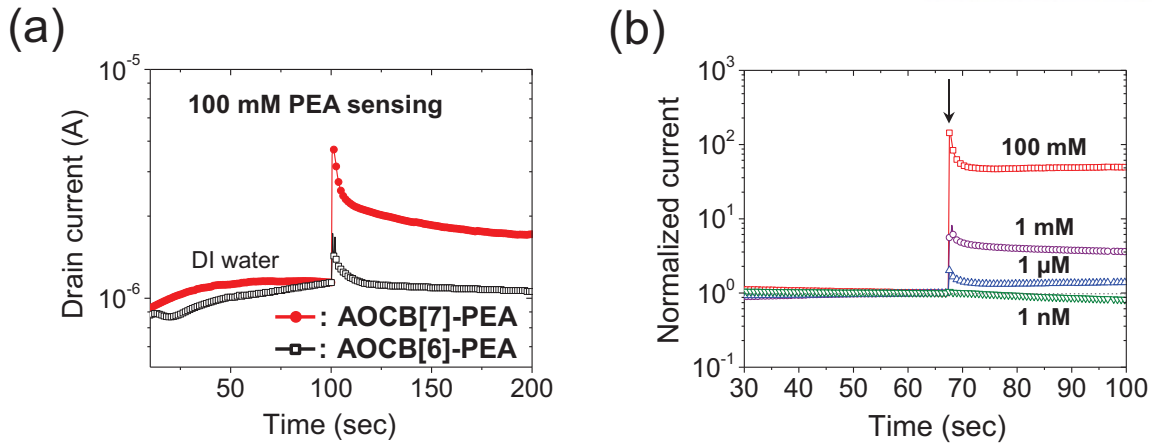

Figure 5.6. a) Comparison of sensing responses of the DDFTTF OFET-based sensors with AOCB[7] and with AOCB[6] toward 100 mM of PEA at V_{DS} = -2 V and V_{GS} = -60 V. b) Sensing results of the sensors with AOCB[7] toward various PEA concentrations (from 1 nM to 100 mM) at V_{DS} = -2 V and V_{GS} = -60 V.

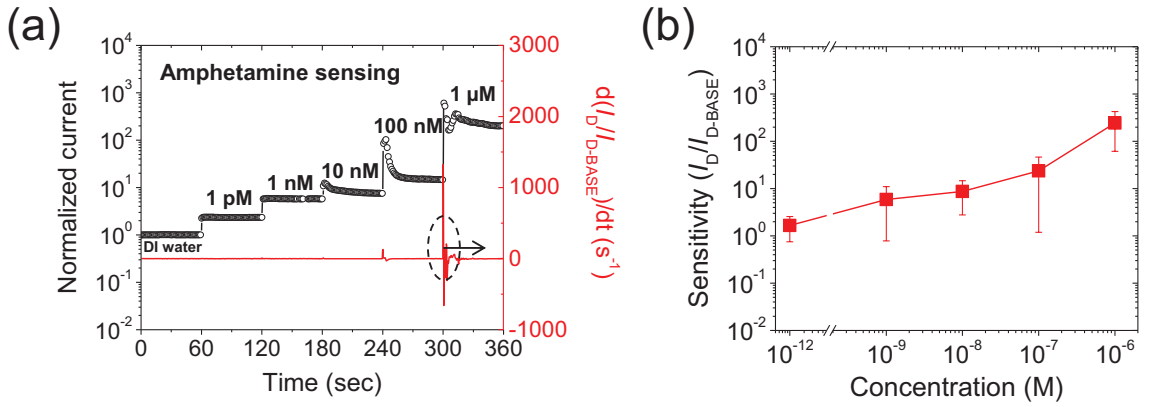

Figure 5.7. a) Real-time responses of DDFTTF OFET-based sensors with AOCB[7] toward various concentrations (from 1 pM to 1 μM) of amphetamine under typical operation conditions (V_{DS} = -2 V and V_{GS} = -60 V). b) Plots showing the sensitivity for amphetamine. The error bar represents the standard deviation.

ULSAN NATIONAL INSTITUTE OF SCIENCE AND TECHNOLOGY

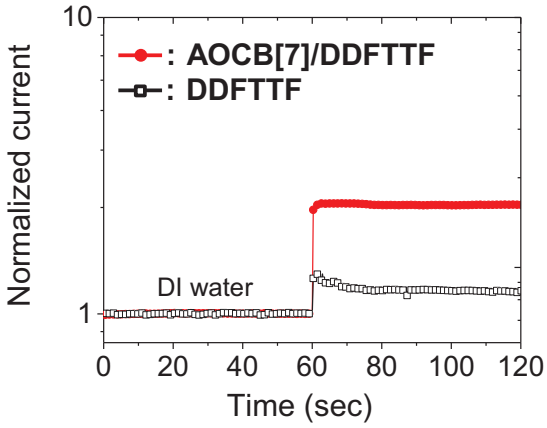

Figure 5.8. a) Comparison of sensing responses of the DDFTTF OFET-based sensors with and without AOCB[7] toward 1 pM of amphetamine at V_{DS} = -2 V and V_{GS} = -60 V.

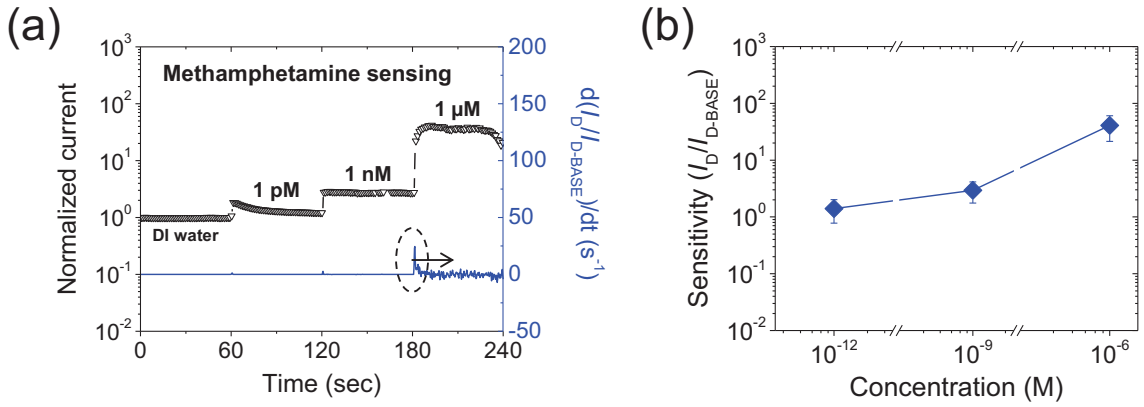

Figure 5.9. a) Real-time responses of DDFTTF OFET-based sensors with AOCB[7] toward various concentrations (from 1 pM to 1 µM) of methamphetamine under typical operation conditions (V_{DS} = -2 V and V_{GS} = -60 V). b) Plots showing the sensitivity for methamphetamine. The error bar represents the standard deviation.

ULSAN NATIONAL INSTITUTE OF SCIENCE AND TECHNOLOGY

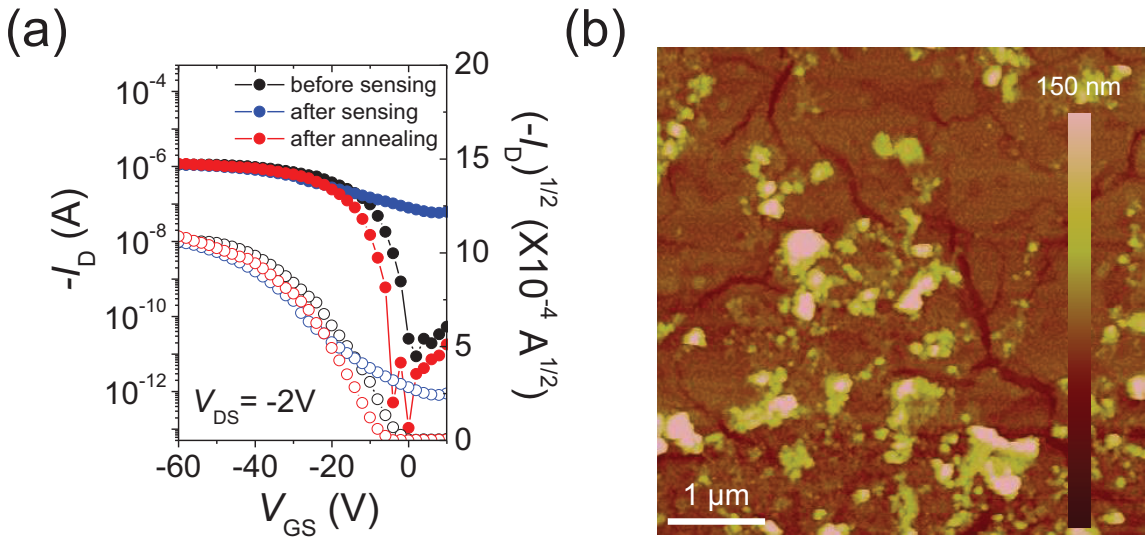

Figure 5.10. a) Comparison of the electrical characteristics of the DDFTTF OFETs with AOCB[7] before and after sensing tests for amphetamine, and re-thermal annealing. b) AFM height image of AOCB[7]/DDFTTF film on OTS-treated SiO2 after re-annealing at 150 °C for 30 min in nitrogen conditions.

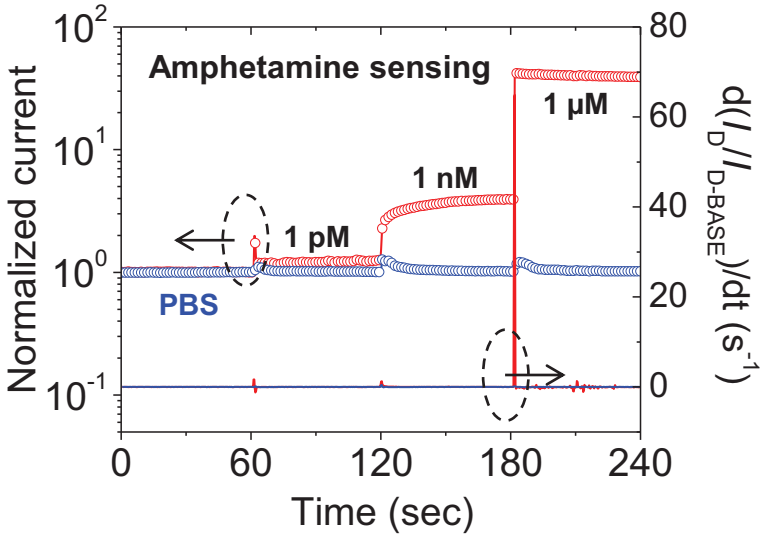

Figure 5.11. a) Real-time responses of the sensors with AOCB[7] toward pristine PBS and various concentrations (from 1 pM to 1 μM) of amphetamine in a PBS solution at V_{DS} = -2 V and V_{GS} = -60 V. Amphetamine solutions were prepared in a PBS solution (pH 7.4, 0.01 M) containing sodium chloride (137 mM) and potassium chloride (2.7 mM).

ULSAN NATIONAL INSTITUTE OF SCIENCE AND TECHNOLOGY

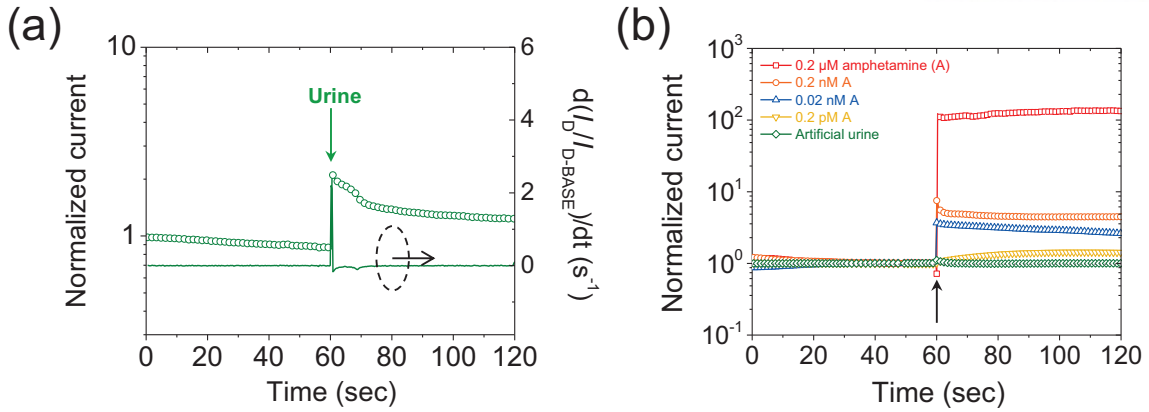

Figure 5.12. a) Sensing responses of the DDFTTF OFET-based sensors with AOCB[7] toward pristine artificial urine at V_{DS} = -2 V and V_{GS} = -60 V. b) Sensing results of the sensors with AOCB[7] toward various amphetamine concentrations (from 0.2 pM to 0.2 μM) in a urine solution at V_{DS} = -2 V and V_{GS} = -60 V.

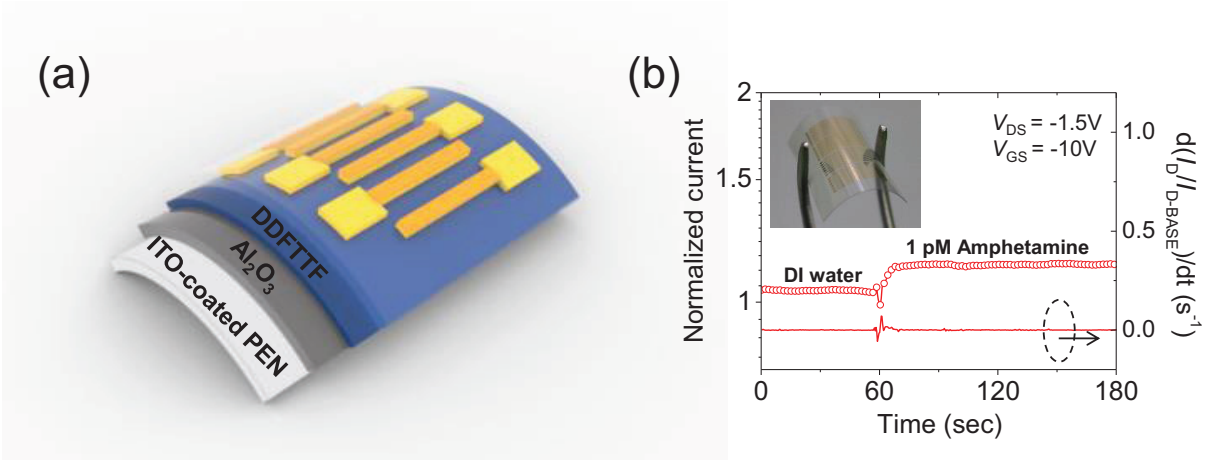

Figure 5.13. a) Schematic illustration of a flexible DDFTTF OFET-based sensor with AOCB[7] sensor prepared with an Al_2O_3 gate dielectric on an ITO-coated PEN substrate. b) Real-time responses of the sensors with AOCB[7] toward 1 pM amphetamine under a low-voltage operation condition. The inset shows a photograph of the flexible sensor with AOCB[7].

ULSAN NATIONAL INSTITUTE OF SCIENCE AND TECHNOLOGY

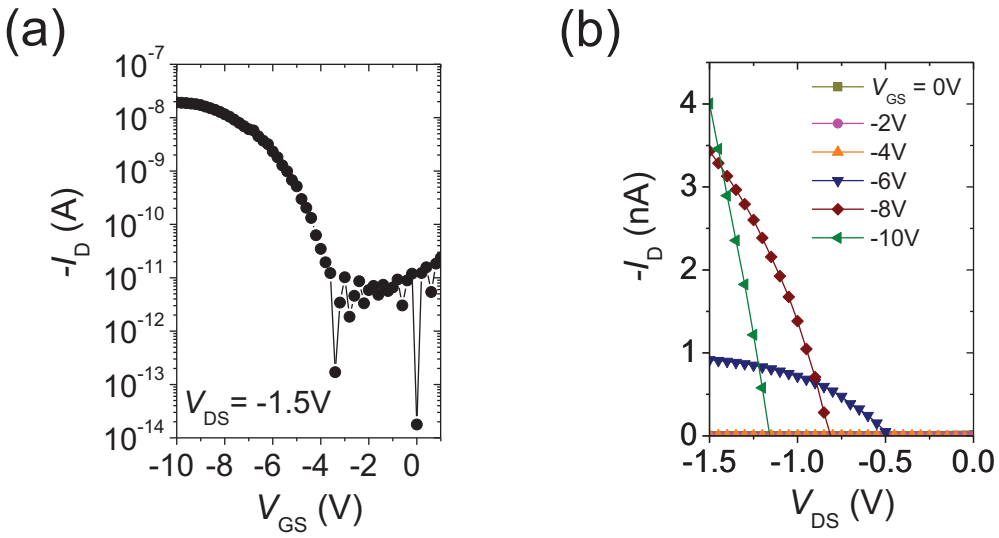

Figure 5.14. a) Transfer and b) output characteristics for flexible DDFTTF OFET-based sensors with AOCB[7] in *p*-channel operation mode.

ULSAN NATIONAL INSTITUTE OF SCIENCE AND TECHNOLOGY

Chapter 6

Summary and Perspectives

In chapter 1, typical properties of organic semiconductors, a discussion of OFET operation, and device architectures are briefly introduced with their sensor applications. The working principles of this OFET-type sensors are discussed in detail, the significance of nanoscopically engineered organic semiconductors for high-performance sensors are also introduced.

In chapter 2, two new polymers (PDPP-FBT and PDPP-2FBT) incorporating diketopyrrolopyrrole (DPP) and either single- or double-fluorinated 2,1,3-benzothiadiazole (BT) were synthesized and investigated. The introduction of doubly-fluorinated BT into the polymer backbone induces a noticeable change in its optical profiles and energy levels, which results in a slightly wider bandgap and deeper HOMO, relative to the others. GIXD analysis reveals that both polymer films have semi-crystalline lamellar structures with edge-on orientations in the solid state. Thanks to the strong intermolecular interactions and highly electron-deficient π-systems driven by the inclusion of F atoms, the polymers exhibit excellent electron-transporting properties (μ_e = 0.42 and 0.30 $cm^2\ V^{-1}s^{-1}$ for PDPP-FBT and PDPP-2FBT, respectively). This study highlights that the use of fluorinated BT blocks in the polymers is a powerful strategy for the molecular design of high-performance *n*-channel-dominant ambipolar OFETs without sacrificing their original hole mobilities.

In chapter 3, an organic heterointerface was successfully fabricated to improve the crystallinity and control the morphology of an organic semiconductor thin film. This work newly report that soft and rubbery characteristics of small molecules interfacing the organic semiconductor can enhance the diffusion of deposited admolecules and improve their crystallinity when the substrate surface is heated at a temperature higher than its glass transition temperature (T_g). Pentacene is used as an active layer above, and *m*-bis(triphenylsilyl)benzene is used as the bottom layer. Sequential evaporations of these materials result in extraordinary morphology with far fewer grain boundaries and myriad nanometre-sized pores. These peculiar structures are formed by difference in molecular interactions between the organic layers and the substrate surface. The pentacene film exhibits high mobility up to 6.3 $cm^2\ V^{-1}\ s^{-1}$, and the pore-rich structure improves the sensitivity of organic-transistor-based chemical sensors. This approach demonstrates a conceptually novel methodology for the fabrication of "structurally engineered" organic semiconducting thin films towards high-performance organic electronics.

In chapter 4, highly sensitive organic-transistor-based sensors that can selectively detect a neurotransmitter acetylcholine (ACh^+) without enzyme immobilization have been prepared by functionalization with a synthetic receptor, a cucurbit[6]uril (CB[6]) derivative. PerallyloxyCB[6]

ULSAN NATIONAL INSTITUTE OF SCIENCE AND TECHNOLOGY

((allyloxy)$_{12}$CB[6], AOCB[6]), which is soluble in methanol but insoluble in water, has been effectively solution-deposited onto a water-stable *p*-channel semiconductor, 5,5′-bis-(7-dodecyl-9H-fluoren-2-yl)-2,2′-bithiophene (DDFTTF) layer, owing to the solvent orthogonality. The OFET-based sensors prepared on a rigid Si wafer and a flexible plastic substrate exhibit a detection limit down to 1 pM of ACh^+, which is six orders of magnitude lower than that of ion-selective electrode-based sensors. Moreover, these OFET-based sensors show highly selective discrimination of ACh^+ over choline (Ch^+), due to the higher binding affinity of AOCB[6] toward ACh^+ compared to Ch^+. This work describes a low-cost and viable way for the fabrication of high-performance sensors for the detection of biogenic molecules. From this work, highly sensitive and selective water-stable OFET-based sensors are a highly promising alternative to conventional enzyme-based biosensors.

In chapter 5, the results obtained herein demonstrate high-performance amphetamine-type stimulants (ATS) sensor from the synergistic combination of a highly selective synthetic host molecule and a highly sensitive OFET device with high fidelity and with low cost as well as on-site detection capability. Other CB homologues, a cucurbit[7]uril (CB[7]) derivative was utilized as the receptor molecule to functionalize the semiconductor film. The first ATS sensors with specific synthetic receptor-engineered OFET-platform are demonstrated on rigid substrate (SiO_2/Si) and even on flexible plastics (polyethylene terephthalate PET) substrates. These sensors in DI water and even in physiological buffer system showed highly sensitive (detection limit of 1 pM of amphetamine) sensing behaviors. Furthermore, these OFET-based sensors show highly sensitive determinations of amphetamine in artificial urine samples. This work provides a viable methodology for the fabrication of OFET-based sensors that can detect the drugs directly in real street samples.

OFETs, three-terminal electronics using organic semiconductors as an active layer, are recognized to be one of the key building blocks for materials/electronics communities. Owing to the growing interest in the field of organic electronics, numerous materials, methods, architectures, and characterization techniques are in development for sensor applications. In particular, OFETs can serve as promising sensor platforms due to their potential applications in cost-effective, light-weight, flexible, high-performance electronics. The intrinsic capability of OFETs to directly transform chemical or physical sensing events to the electrical signals provides them with great potential as reliable sensors offering high sensitivity, selectivity, and rapid responses. Although rapid advances in developing such OFET-based sensors in the last several years have demonstrated the peaking significance and potential utility of this unique class of sensing platforms, most of the current works still remain a number of challenges to be addressed on the sensors' quality for diverse practical uses.

Continuous efforts to further improve the qualities of sensors, including sensitivity, selectivity, response time, stability, reproducibility, limit of detection, can be effectively performed by using on-demand, structure-engineered, surface-engineered, and tailored organic materials for the active layers

ULSAN NATIONAL INSTITUTE OF
SCIENCE AND TECHNOLOGY

of the devices. For potential commercial uses include wearable consumer electronics, smart robotics, medical prosthetics, electronic skin, and health monitoring, therefore, detection systems on nanoscopically engineered organic-transistor-based sensors must be addressed and developed. Furthermore, this needs in-depth understanding of the working mechanism of the sensors. More importantly, portable and miniaturized sensors with wireless and smartphone applications for the real-time detection capabilities should be created by nanoscopically engineered organic-transistor-based sensors, which afford excellent components for the state-of-the-art protocol-type sensors.

ULSAN NATIONAL INSTITUTE OF SCIENCE AND TECHNOLOGY

Acknowledgements

I am so honored to receive Ph.D. degree from Ulsan National Institute of Science and Technology (UNIST), and to enjoy this wonderful honor of knowing or working in Soft Nanomaterials and Devices Laboratory (SNDL). First of all, I would like to express my deep appreciation to my supervisor Professor Joon Hak Oh throughout my Ph.D. period. Under professor's supervision, I learnt how to grow as an independent research scientist. His advice and training on both research as well as on my career have been invaluable. I am very grateful for his contributions of time, directions, and support to make my Ph.D. research studies productive and stimulating.

I would like to thank to my co-supervisor Professor Changduk Yang. He encouraged me to pursue this doctoral degree during my graduate course. I would also like to thank to my thesis committee professors, Prof. Hyunhyub Ko, Prof. Sang Kyu Kwak, Prof. Byeong-Su Kim for professors' invaluable suggestions and feedback on my thesis. In addition, I thank to professors and co-workers of collaborative group, Prof. Kimoon Kim, Prof. Kilwon Cho, Prof. Yoonyoung Chung, Dr. Ilha Hwang, and Dr. Boseok Kang in POSTECH, and Dr. Junghoon Lee in UNIST.

Moreover, I would especially like to thank to all of SNDL members for allowing me to research in a pleasant and enjoyable working environment for my Ph.D. thesis. I have experienced their kind help and support day by day. I am very grateful to all of you. To my graduate student friends of UNIST and POSTECH, and my friends, I thank them for their support and generosity. Lastly, I would like to sincerely thank to my family, my parents and my brother, for all their support, encouragement, and love throughout my life. My parents always believe me and cheer me up to realize my own potential. Without them, I may never have gotten to where I am today. I would like to thank everyone once more.

Jan. 11. 2017

Moonjeong Jang

ULSAN NATIONAL INSTITUTE OF SCIENCE AND TECHNOLOGY

감사의 글

박사학위를 받기까지, 저의 지도 교수님이신 오준학 교수님의 아낌없는 지도와 훌륭한 가르침을 받으면서 학업과 연구에 더 집중할 수 있었고 박사학위 과정을 끝까지 마칠 수 있었습니다. 교수님께 진심으로 감사 드립니다. 대학원에 입학하고 무엇부터 시작해야 하는지 모르는 저에게 배움의 길을 열어주시고, 학생으로서 제가 한계에 부딪히거나 힘이 들 때는 함께 고민해주시고 조언해주셨으며 항상 응원해주셨습니다. 연구가 무엇인지, 제가 무엇을 잘 하는지 스스로 깨달을 수 있도록 부족한 저를 잘 이끌어주셨던 교수님. 앞으로도 베풀어주신 교수님의 가르침을 가슴에 새기며 이루고자 하는 모든 일에 열정을 가지고 자랑스러운 제자로서, independent한 연구자로서 성장해 나가겠습니다. 다시 한번 깊은 감사와 존경의 마음을 전하고 싶습니다.

또한 UNIST 지도 교수님이신 양창덕 교수님께 깊은 감사의 말씀을 올리고 싶습니다. 학위기간 동안 관심 많이 가져주시고 격려해주시고 힘을 주셔서 정말 감사 드립니다. 바쁘신 가운데에도 박사학위 심사위원을 흔쾌히 수락해주시고 함께 해주신 고현협 교수님, 곽상규 교수님, 그리고 김병수 교수님, 찾아갈 때마다 반겨주시고, 항상 아낌없는 조언과 따뜻한 격려 정말 감사합니다. 하시고자 하는 연구도 모두 잘 되기를 진심으로 바라겠습니다. 그리고 공동 연구로 많은 기회와 도움을 주신 포항공대 김기문 교수님, 조길원 교수님, 정윤영 교수님, 황일하 박사님, 강보석 박사님, UNIST 이정훈 박사님께도 감사의 말씀을 올리고 싶습니다.

그리고 옆에서 대학원 생활을 잘할 수 있도록 격려해 주고 이끌어준 하나뿐인 제 동기 은광 오빠, 티격태격할 때도 있지만 5년 동안 힘들 때마다 서로 의지하면서 도움을 많이 받았던 것 같아요. 아무 탈 없이 함께 졸업하게 되서 기쁘고 창업 그 꿈, 꼭 이루길 바랄게요. 5년이나 함께한 우리 연구실의 터줏대감으로 섬세하고 정 많은 보고서 작성 메이트 무열이, 다양한 색깔의 트레이닝 복으로 열심히 실험하는 우리 연구실의 스마트 학생 윤호, 연구실 원년 멤버라 해도 전혀 이상하지 않은 맥박 센서 만들어줄 오영 오빠, 방장으로 누구보다 연구실을 잘 이끌어 나갈 성실하고 책임감 넘치는 쭈봉 여자친구 해랑이, 형들 잘 따르고 센스 있는 입담과 실험 스킬을 가진 철희, 이제 장난도 잘 치고 새로운 분야에서 잘 해내고 있는 걱정인형 인호, 똑 부러지게 일 잘하는 부사수 효은이. 2년 동안 날 믿고 따라와줘서 고맙고, 더 많은 시간을 함께 하지 못해서 아쉽지만 어디에 있든지 주어진 일을 잘 해낼 수 있을거야. 걱정하지 말고 항상 응원할게! 한국인 입맛을 가진 타고난 기럭지 미녀 하눔, 밥 잘 먹고 몸 관리 잘하는 많이 친해진 징징이 홍기, 해맑고 연구에 관심 많은 로맨틱 가이로 변신한 상진이, 착하고 인사성 밝은 웃는 얼굴 용희, 벌써 연구실 생활에 완벽 적응한 신입생 같지 않은 신입생들 종현이와 재환이, 소녀 감성이지만 우리 연구실이 세계로 한 단계 더 뻗어 나갈 수 있도록 합성의 문을 열어준 Xiaobo 박사님, 파마머리를 고수하는 다방면에서 노력하고 잘하는 토마토 지

ULSAN NATIONAL INSTITUTE OF SCIENCE AND TECHNOLOGY

형 오빠, 크고 작은 일들을 겪으면서 저의 20대의 많은 추억을 함께한 그리운 까마귀 1호정 언니와 까마귀 2 아름 언니, 언니들 덕분에 씩씩하게 연구실 생활 잘 해낼 수 있었고, 선배의 중요성도 알게 되고, 빈자리가 크게 느껴지지만 우리 더 자주 오래 보도록 해요. 항상 제 주변 어딘가에 있을 어엿한 직장인으로 변해가는 우리 연구실의 애교쟁이 오홍자 자연이, 철저한 감시로 증착기를 열심히 맡아주었던 동영이, OEL 원년 멤버들인 은엽이, 다정이, 유진이와 Xien 교수님까지 5년 동안 가족들보다 더 오래 보고 함께하면서 참 많은 것을 배우고 좋은 추억들을 쌓았습니다. 그리고 우리 SNDL 멤버들, 모두들 힘내서 좋은 일만 가득하기를 바라겠습니다. 진심으로 고맙습니다. UNIST 대학원 생활을 함께하면서 정들었던 결혼한 일영 오빠, 긍정적인 현지 언니, 털털한 쿨녀 소연 언니, 서울대로 이사간 은선이 정말 고맙습니다.

제 꿈을 함께 응원해줬던 친구들, 개구리들 지혜, 윤진이, 지회, 같은 길을 걷고 있는 지혜, 슬기, 윤정이 그리고 근아, 그리고 티파니 수하와 태연 채빈이, 힘들 때마다 의지했고 덕분에 연구할 때도 더 힘이 나서 잘해낼 수 있었습니다. 정말 고맙다는 말을 전하고 싶습니다.

마지막으로 제 버팀목이자 든든한 지원군인 사랑하는 우리 가족, 아버지, 어머니, 그리고 남동생에게 정말 감사하다는 말을 전하고 싶습니다. 길다면 길 수도 있는 대학원 생활 동안 타지에 있는 딸 걱정해주시고 응원해주신 부모님의 사랑 속에서 현재의 저로 성장할 수 있었습니다. 항상 건강하시고, 믿고 기대하는 만큼 더욱 자랑스러운 딸, 더욱 훌륭한 사람이 되겠습니다.

지난 5년간의 대학원 생활을 값진 성장통으로 삼아 현재의 저에 안주하지 않고 더욱 더 발전하고 성장해 나가겠습니다. 마지막으로 사회에 이바지하고자 끊임없이 고민하고 열정을 갖고 가치 있는 사람이 될 것을 다짐하며 감사의 글을 마치겠습니다.

2017년 1월 11일

장 문 정

ULSAN NATIONAL INSTITUTE OF SCIENCE AND TECHNOLOGY

Curriculum Vitae

Moonjeong Jang

Personal Details

Name	Moonjeong Jang
Gender	Female
Date of Birth	June 30, 1989
Nationality	Republic of Korea
Address	School of Energy and Chemical Engineering, Ulsan National Institute of Science and Technology (UNIST), UNIST-gil 50, Ulsan 689-798, South Korea
E-mail Address	jmoonjeong@unist.ac.kr

Education

M.S. & Ph.D.	Mar. 2012 – Feb. 2017 Energy Engineering, School of Energy and Chemical Engineering, Ulsan National Institute of Science and Technology (UNIST), Research Advisor: Prof. Joon Hak Oh (POSTECH), Prof. Changduk Yang (UNIST)
B.S.	Mar. 2008 – Feb. 2012 Fine Chemical Engineering and Applied Chemistry, Chungnam National University

Publication

1. G. Kim,† H. Kim,† M. Jang, Y. K. Jung, J. H. Oh,* C. Yang,* "Ultra-Narrow-Bandgap Thienoisoindigo Polymers: Structure-Property Correlations in Field-Effect Transistors", *J. Mater. Chem. C* **2016**, *4*, 9554-9560 [† contributed equally]
2. M. Jang, M. Y. Lee, J. H. Jung, J. H. Oh,* "웨어러블 소자 응용을 위한 분자기반 고성능 센서 (Molecule-Based High-Performance Sensors for Wearable Device Applications)", *Polymer Sci. Technol.* **2015**, *26*, 290-298
3. M. Jang, H. Kim, S. Lee, H. W. Kim, J. K. Khedkar, Y. M. Rhee, I. Hwang,* K. Kim,* J. H. Oh,* "Highly Sensitive and Selective Biosensors Based on Organic Transistors Functionalized with Cucurbit[6]uril Derivatives", *Adv. Funct. Mater.* **2015**, *25*, 4882-4888
4. J. Lee,† M. Jang,† S. M. Lee, T. J. Shin, J. H. Oh,* C. Yang,* "Fluorinated Benzothiadiazole (BT) Groups as a Powerful Unit for High-Performance Electron-Transporting Polymers", *ACS Appl. Mater. Interfaces* **2014**, *6*, 20390 [† contributed equally]
5. B. Kang,† M. Jang,† Y. Chung,† H. Kim, S. K. Kwak, J. H. Oh,* K. Cho,* "Enhancing 2

ULSAN NATIONAL INSTITUTE OF SCIENCE AND TECHNOLOGY

D growth of organic semiconductor thin films with macroporous structures via a small-molecule heterointerface", *Nat. Commun*. **2014**, 5:4752 [†contributed equally]

6. J. H. Oh,* A.-R. Han, H. Yu, E. K. Lee, M. Jang, "Tuning Polarity and Improving Ch arge Transport in Organic Semiconductors", *Proceedings of SPIE* **2013**, *8331*, 883112

Patents

1. K. Cho, J. H. Oh, B. Kang, M. Jang, Y, Chung, "다공성 유기 반도체 층을 갖는 적층체 및 그를 포함하는 화학센서 (Laminate Having Porous Organic Semiconductor Thin Film and Chemical Sensor Comprising the Same)" KR 10-1645176-0000 (07-28-2016)
2. K. Cho, J. H. Oh, B. Kang, M. Jang, Y, Chung, "유리전이온도를 갖는 저분자 물질을 포함하는 적층체 및 그의 제조방법 (Laminated Structure Comprising Small-Molecular Material and Method for Preparing the Same)" KR 10-1577989 (12-10-2015)

Presentation (Domestic)

1. M. Jang, H. Kim, G. Kim, C. Yang, J. H. Oh, "N-Channel Organic Field-Effect Transistors Based on Substituted Indigo Derivatives with Strong Electron-Withdrawing Groups", The Polymer Society of Korea Spring Meeting, Daejeon, Korea, Apr. 06-08, **2016**.
2. M. Jang, I. Hwang, S. Lee, H. Kim, K. Kim, J. H. Oh, "High-Performance Sensors Based on Organic Semiconductor Thin Film Functionalized with Synthetic Receptor Molecules", The Korean Society of Industrial and Engineering Chemistry Spring Meeting, Busan, Korea, Apr. 30-May. 1, **2015**.
3. M. Jang, J. Lee, S. M. Lee, D. Yoo, T. J. Shin, C. Yang, J. H. Oh, "Fluorinated Benzothiadiazole-Based Polymers for High-Performance n-Channel Organic Field-Effect Transistors", The Korean Society of Industrial and Engineering Chemistry Spring Meeting, Busan, Korea, Apr. 30-May. 1, **2015**.
4. M. Jang, B. Kang, Y. Chung, H. Kim, S. K. Kwak, K. Cho, J. H. Oh, "High-Performance FET-Type Chemical Sensors Based on Organic Semiconductor Thin Films with Macroporous Structures", The Korean Society of Industrial and Engineering Chemistry Spring Meeting, Busan, Korea, Apr. 30-May. 1, **2015**.
5. M. Jang, I. Hwang, S. Lee, H. Kim, K. Kim, J. H. Oh, "Highly Sensitive and Selective OFET-Type Sensors Using Synthetic Ionophores: Cucurbit[6]uril Derivatives", The Korean Institute of Chemical Engineers (KIChE) Spring Meeting, Jeju, Korea, Apr. 22-24, **2015**. (In Honor of the Best Thesis Award)
6. M. Jang, J. Lee, C. Yang, J. H. Oh, "High Electron Mobilities for Field-Effect Transistors Based on Ambipolar Diketopyrrolopyrrole-Benzothiadiazole Polymer with Fluorine Substituents", The Polymer Society of Korea Spring Meeting, Daejeon, Korea, Apr. 11-12, **2013**.

Presentation (International)

1. M. Jang, I. Hwang, H. Kim, E. Jin, K. Kim, J. H. Oh, "High-Performance Field-Effect Transistor-Type Sensors Functionalized with Cucurbit[7]uril (CB[7]) Derivatives", IUPAC-PSK40, Jeju, Korea, Oct. 04-07, **2016**.

ULSAN NATIONAL INSTITUTE OF SCIENCE AND TECHNOLOGY

2. M. Jang, H. Kim, S. Lee, H. W. Kim, J. K. Khedkar, Y. M. Rhee, I. Hwang, K. Kim, J. H. Oh, "Highly Sensitive and Selective Biosensors Based on Organic Semiconductor Thin Film Functionalized with Cucurbit[6]uril Derivatives", The Korea-Japan Joint Forum (KJF) Fall Meeting, Jeju, Korea, Sep. 6-9, **2015**.
3. M. Jang, I. Hwang, S. Lee, I. H. Song, K. Kim, J. H. Oh, "Highly Sensitive Water-Stable OFET-Based Biosensors Functionalized with Molecular Sieves: Cucurbit[6]uril Derivatives", Materials Research Society (MRS) Fall Meeting, Boston, MA, USA, Nov. 30-Dec. 5, **2014**. [A6.11]
4. M. Jang, J. Lee, C. Yang, J. H. Oh, "High Electron Mobilities for Field-Effect Transistors Based on Ambipolar Diketopyrrolopyrrole-Based Copolymers with Fluorine Substituents", 5th Asian Conference on Organic Electronics, POSTECH, Pohang, Korea, Nov. 13-15, **2013**. [Received "the Best Poster Award"]